Advanced Carbon Fiber Composite Materials for Shielding and Antenna Applications

AIDIN MEHDIPOUR

A THESIS
IN
THE DEPARTMENT
OF
ELECTRICAL AND COMPUTER ENGINEERING

PRESENTED IN PARTIAL FULFILLMENT OF THE REQUIREMENTS
FOR THE DEGREE OF DOCTOR OF PHILOSOPHY AT
CONCORDIA UNIVERSITY
MONTREAL, QUEBEC, CANADA

MAY 2011

CONCORDIA UNIVERSITY

SCHOOL OF GRADUATE STUDIES

This is to certify that the thesis prepared

By: **Aidin Mehdipour**

Entitled: **Advanced Carbon Fiber Composite Materials for Shielding and Antenna Applications**

and submitted in partial fulfillment of the requirements for the degree of

DOCTOR OF PHILOSOPHY (Electrical & Computer Engineering)

complies with the regulations of the University and meets the accepted standards with respect to originality and quality.

Signed by the final examining committee:

_____ Chair
Dr. R. Glitho

_____ External Examiner
Dr. C. Caloz

_____ External to Program
Dr. V.S. Hoa

_____ Examiner
Dr. T. Denidni

_____ Examiner
Dr. R. Paknys

_____ Thesis Co-Supervisor
Dr. A.R. Sebak

_____ Thesis Co-Supervisor
Dr. C.W. Trueman

Approved by _____
Dr. M. Kahrizi, Graduate Program Director

May 16, 2011 _____
Dr. Robin A.L. Drew, Dean
Faculty of Engineering & Computer Science

Abstract

Advanced Carbon Fiber Composite Materials for Shielding and Antenna Applications

Aidin Mehdipour, Ph.D.

Concordia University, May 2011

Due to the low weight, ease of fabrication, low cost, high stiffness, high thermal and electrical conductivity, advanced carbon fiber composite (CFC) material is one of the most desirable materials which have been considered recently in the aerospace, electronic, and infrastructure industry.

This thesis examines the use of CFC materials for electromagnetic field shielding and antenna applications. Using a suitable electromagnetic model of composite materials, we evaluate the shielding effectiveness (SE) and other EM properties of composites paying attention to antenna design. Analytical and simulation results are compared with experimental data. Two kinds of composite materials are investigated, namely reinforced continuous carbon-fiber (RCCF) composites and carbon nanotube (CNT) composites.

For analytical SE analysis of multilayer RCCF composites, the material shows anisotropic behavior along the direction of the fibers, and we employ the transmission matrix method in conjunction with the anisotropic properties of each layer. The shielding performance of composites is also experimentally investigated. In order to enhance the conductivity of an RCCF composite, a small volume fraction of multi-walled carbon nanotubes (MWCNTs) is added to the RCCF material. We investigate the SE of the proposed MWCNT “nanocomposite” over a wide frequency band up to 26.5 GHz. The

effect of aspect ratio on shielding performance is addressed as well. The effective conductivity of the nanocomposites was determined over the frequency range of interest.

The use of RCCF and single-walled carbon nanotube (SWCNT) composite is investigated for building antennas, by replacing the metal with CFC. We use an RCCF composite to build resonant and wideband antennas. The effect of the conductivity tensor of RCCF composite on the antenna performance is addressed. We also study the performance of a microstrip patch antenna with the ground plane made of RCCF composite.

As one of the most highly-conductive composite materials, single wall carbon nanotube (SWCNT) buckypapers are used to build composite antennas. A new fabrication method is proposed to print arbitrarily-shaped full-composite SWCNT antenna on any type of substrate. Various types of SWCNT antennas are fabricated for different antenna applications, namely UHF-RFID, WLAN, UWB, and mm-wave applications. Good agreement is observed between simulation and experimental results for all the aforementioned composite antennas.

Using the spectral domain method, the Green's function is obtained for an infinitesimal HED on a dielectric slab over a CFC ground plane. Due to the high conductivity, CFCs are modeled using a surface impedance. The expressions for the electric field components are derived. The numerical integration details particularly dealing with low-converged tail of the integrand for fields at the air-dielectric interface are addressed. Numerical results based on this method compare well with results based on a time-domain finite integration technique. The effect of conductivity and anisotropy of the composite ground plane on electric field is investigated.

Acknowledgments

Foremost, I owe my deepest gratitude to my advisors, Prof. Abdel R. Sebak and Prof. Christopher W. Trueman, for their invaluable supervision, encouragement and support in every stage of my research. This thesis would not have been possible without their guidance, patience and enthusiasm.

My sincere thanks also go to Prof. Suong V. Hoa, as a member of my thesis committee, and Dr. Iosif D. Rosca at Concordia Center for Composites for their cooperation in providing composite materials and printing composites on substrate, and for the valuable technical discussions on composite materials. I would also like to thank Prof. Robert Paknys, Prof. Tayeb A. Denidni and Prof. Christophe Caloz for their participation in my thesis committee and for their valuable comments and suggestions.

Last but not the least, I would like to thank my family for all their support and encouragement. I am much indebted to my parents, whose dedication and affection are always with me throughout my life.

Table of Contents

List of Figures

List of Tables

List of Symbols

ε	Electric Permittivity
ε_0	Permittivity of Vacuum, $\varepsilon_0 = 8.854 \times 10^{-12}$ F/m
σ	Electric Conductivity
δ	Skin depth
η	Wave Impedance
β	Propagation Constant
μ	Magnetic Permeability
μ_0	Permeability of Vacuum, $\mu_0 = 4\pi \times 10^{-7}$ N/A^2
μ_r	Relative Permeability
ω	Angular Velocity
θ_i	Incident Angle of Plane wave
φ	Angle between Principal and Global Coordination
γ	Polarization Angle of Plane wave
∇	Del Operator
π	Angular Distance in Radian, $\pi = 180$ degrees
Σ	Summation
$\vec{E}$	Electric Field
$E\perp$	Perpendicular Mode
$E_{\parallel}$	Parallel Model
$\vec{H}$	Magnetic field
$\vec{J}$	Electric surface Current Density
f	Frequency
d_{max}	Maximum Read Range
Q	Quality Factor

List of Abbreviations

mm	millimeter
EMC	Electromagnetic Compatibility
EMI	Electromagnetic Interference
SE	Shielding Effectiveness
2D	Two Dimensions
3D	Three Dimensions
PEC	Perfect Electric Conductor
FCC	Federal Communication Commission
DMF	Dimethylformamide
WiMAX	Worldwide-Interoperability-for-Microwave-Access
WPAN	Wireless Personal Area Network
CST MWS	Computer Simulation Technology Microwave Studio
CVD	Chemical Vapor Deposition
CFC	Carbon Fiber Composite
CB	Carbon Black
RCCF	Reinforced Continuous Carbon Fiber
CNT	Carbon NanoTube
MLA	Meander Line Antenna
MoM	Method of Moment
MWCNT	Multiwall Carbon Nanotube
SWCNT	Single-Wall Carbon NanoTube
SCF	Short Carbon Fiber
TMM	Transmission Matrix Method
FDTD	Finite Difference Time Domain
FEM	Finite Element Method
FIT	Finite Integration Technique
TE	Transverse Electric
TM	Transverse Magnetic

TEM	Transverse Electromagnetic
AR	Aspect Ratio
RFID	Radio-Frequency Identification
CONCOM	Concordia Center for Composites
UWB	Ultra-Wideband
UHF	Ultra High Frequency
HED	Horizontal Electric Dipole
IPL	Interference Path Loss
GPS	Global Positioning System

Chapter 1 : Introduction

Different kinds of metals such as copper and aluminum are extensively used in aerospace and many other industrial applications. In fact, the high value of the conductivity of metal makes it a very good candidate for shielding applications. However, some disadvantages of metals are their high weight, manufacturing cost and poor corrosion resistance, which make designers want to produce a good alternative material to metals. For this purpose, many kinds of "composite" materials have been proposed [1]-[7].

Due to the low weight, ease of fabrication, low cost, high stiffness, high thermal and electrical conductivity, a carbon fiber composite (CFC) is one of the most desirable materials which have been considered recently in the aerospace, electronic, and infrastructure industry [8]-[13]. In electrical applications, CFCs are used for electromagnetic interference (EMI) shielding, thermoelectric energy conversion, radar absorbing material, sensors, switches, electronic devices like diodes and transistors, and thermal pastes [14]. However, one of the main disadvantages of CFC is their relatively low conductivity compared to metals. The low conductivity leads to low shielding effectiveness (SE), which is a very critical factor for electromagnetic compatibility (EMC) purposes. The characterization and analysis of the SE of composites is a very challenging issue for EMC engineers [11], [15]-[25].

Metals are regularly used in antenna and microwave structures as the material for the radiating element, transmission lines and feed networks. In new antenna and microwave

technologies, low-cost, low-weight, low-corrosion and high thermal conductivity characteristics are factors with high degree of importance. For this purpose, one should think about the materials other than metals. Recently, a few conductive materials have been introduced as a replacement of metals for some limited antenna applications [26]-[31]. Due to the low conductivity of conductive composites, replacing metals with such a material is challenging and needs much more investigation.

1.1 Motivations

Recently, CFCs have been used extensively in the aerospace and aircraft industry. There are many sensitive electronic equipments inside the fuselage of spacecraft, aircraft, and helicopters, susceptible to interference from external electromagnetic waves [32]-[35]. Interference can degrade the performance of electronic devices considerably and so the fuselage is required to be a good electromagnetic shield against external fields. But by using a composite as the material for the fuselage instead of a metal, the shielding properties degrade drastically. As a result, in addition to the mechanical properties, the EM shielding characterization of composites is very important factor which should be investigated carefully. There are many parameters which affect the SE of CFC, such as the fabrication process, the fiber percentage, and the thickness of sample [22]. It should be noted that because of the complicated structure of composites, they may show frequency-dependent shielding properties over wide frequency ranges [22][25],[37]. Moreover, the direction of fibers in some kinds of CFCs such as reinforced continuous carbon fiber (RCCF) composite is a very critical factor which makes the material show an anisotropic property along the fiber direction [25],[38]-[40]. Therefore, one should use

appropriate analytical and modeling approaches to analyze the shielding properties of composites. However, since in practical cases the composite material is not exactly like an assumed model for analytical methods, the experimental verification of shielding performance of composites is another important factor which should be evaluated over the frequency range of interest. The analysis of SE is associated with the conductivity characterization of composites, which is also necessary for composite antenna design.

Aside from shielding analysis, in order to use CFC in antenna structures as radiating elements, two challenging issues arise. The first challenge is the radiation properties of composite antennas which could be significantly different than copper antennas due to the lower conductivity of composite. Another challenge is the fabrication of composite antennas, including printing composite material on the substrate and making any arbitrary shape of an antenna on the substrate. Providing a strong adhesion between the composite and substrate is another significant challenge.

1.2 Objectives

One objective of this work is to investigate the shielding properties of different kinds of CFC materials. For this purpose, first we use appropriate models of these composites for analytical or numerical analysis. Then, by applying suitable methods the shielding behavior of the composite material is determined and the effect of the different physical parameters of composite on the SE is obtained. Choosing the appropriate model for a composite material highly depends on the carbon fibers distribution inside the material. After proposing the model, the useful method, whether analytical or numerical, should be employed to solve the problem. Depending on the type of composite, different kinds of

methods could be used, such as the transmission matrix method (TMM) [36], Floquet-mode theory [38], the method of moments (MoM)[41], homogenization methods [42], finite element method (FEM), or the finite difference time domain (FDTD) method [43]. By doing the analytical or numerical study, we can find out the effect of different physical parameters of composites on SE. SE of composites is also experimentally examined over a very wide frequency range up to 50 GHz. It is done by using different standard measurement setups such as a coaxial fixture at low frequencies, and various waveguide setups at higher frequencies. We consider two famous types of CFCs, namely reinforced continuous carbon fiber (RCCF) and carbon nanotube (CNT) composites. The composite samples were produced at the Concordia Center for Composites (CONCOM) Laboratory [44].

Another main objective of this dissertation is to explore using CFCs in antenna structures and associated applications. The performance of various types of antennas is investigated when the metal parts are replaced with composites. By doing so, a new generation of antennas is proposed, having no metal in their structure. We will consider different types of resonant, multiband, and wideband antennas designed for various applications.

1.3 Thesis Organization

This thesis is organized as follows.

In Chapters 2 and 3, we introduce two commonly-used CFC materials, namely RCCF and CNT composites, respectively. We investigate the electrical and shielding characteristics of these composites using appropriate analytical and numerical models.

The TMM method along with accurate equivalent EM model is used to calculate the SE of multilayered RCCF's. The shielding property of both RCCF and CNT composites is addressed experimentally over a wide frequency range, from DC to 26.5 GHz. The effect of CNT loading and aspect ratio (AR) on SE and conductivity of CNT composites is studied in detail.

In Chapter 4, using the spectral domain method, we calculate the exact solution for the Green's function of a dielectric slab backed by a CFC ground plane and excited by a horizontal electric dipole (HED). The expression for the electric field is obtained and the numerical integration is addressed in detail. Finally, some numerical results are presented and compared to that of the slab with a perfect electric conductor (PEC) ground plane. Moreover, numerical results based on this method compare well with results based on a time-domain finite integration technique (FIT).

In Chapters 5 and 6, we explore the use of CFCs for antenna structures. RCCF, RCCF/CNT, and CNT composites are used as the replacement of metal in the antenna structures. The effect of adding fractional CNT loading to RCCF samples is investigated, which leads to an improvement in the conductivity of the RCCF/CNT composite compared to the RCCF material itself. Different types of antennas are considered for study operating over UHF radio frequency identification (UHF-RFID), Bluetooth, wireless local area network (WLAN), UWB, X-band, and mm-wave frequency ranges. The effect of conductivity tensor of CFCs on the antenna performance such as bandwidth and gain is addressed. For wideband applications, the dispersion characteristic of the antenna is investigated. Experimental verification is provided for the performance of these CFC antennas. The fabrication process and the associated challenges are discussed.

A new fabrication technique is proposed to print CNT buckypaper on both sides of substrate to make full-composite antennas with desired shape and structure. Different kinds of substrate are considered to show the versatility of the proposed fabrication process.

Chapter 7 contains conclusions of the thesis and addresses future research into the use of CFCs for shielding, antenna, and microwave applications.

Chapter 2 : Shielding Characteristics of Reinforced Continuous Carbon Fiber Composites

The reinforcing fibers of the carbon-fiber composites could be in various forms such as RCCF, short carbon fiber (SCF), carbon nanotube (CNT), and carbon black (CB). In this dissertation, we consider two frequently-used CFCs, namely RCCF and CNT composites. These materials have good mechanical and chemical properties. Moreover, the electrical conductivity of these CFCs is typically higher than other types of composites, making them more suitable for EM and shielding applications.

A typical RCCF composite is composed of a resin reinforced by fibers that are oriented in a specific direction, as shown in Figure 2.1. Such materials are often made in several or many layers, with the carbon fibers oriented in a different direction in each layer, to approximate isotropic behavior. The cross-sectional view of a single-layer RCCF is shown in Figure 2.1 (b). The average diameter of fibers is 4.98±0.36 μm and separation distance between fibers is typically 1 μm. The density of RCCF composites is around 1.5 g/cm^3, half that of aluminum and more than five times lower than copper.

From an EMC point of view, since for most applications the shielded device is under far-field electromagnetic field exposure, plane wave shielding effectiveness is adequate

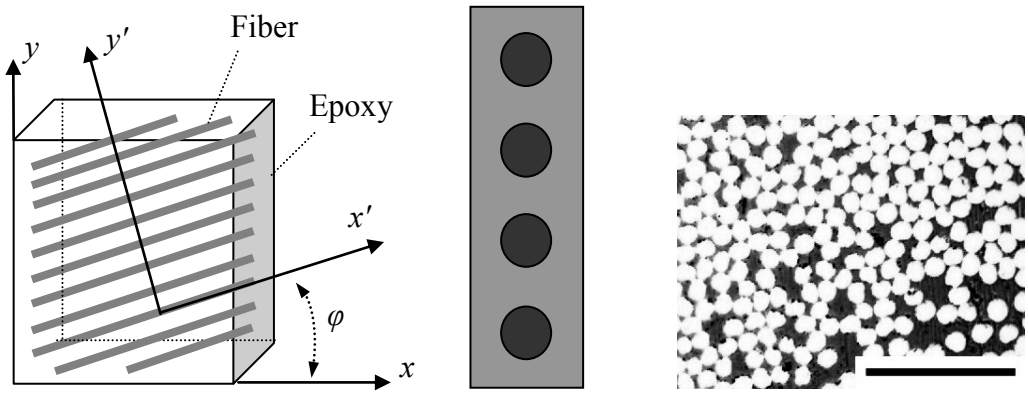

(a) (b) (c)

Figure 2.1 (a) RCCF composite, (b) Cross-view, (c) Optical micrograph of RCCF Composite (scale bar 50 μm).

for analysis. A full-wave numerical solution simulation must use a very fine discretization step to represent the individual composite fibers, which leads to a very time-consuming process. Therefore, due to the complex structure of composites, some analytical techniques with specific assumptions have been introduced to simplify the problem [36], [38], [41]. In [38], a model based on filament currents and the "thin current assumption" was proposed to provide a highly accurate result at high frequencies. However, the accuracy of this model depends on both frequency and incidence angle so that it is not valid for some particular oblique incidence directions. In [41], a periodic surface integral equation was employed to analyze one-layer fiber-reinforced composite materials. Even though this method predicts the composite shielding behavior well at very high frequencies for all incidence angles, it requires a lot of CPU time particularly when applied to multilayer composite material structures.

When the period of periodic structure is much less than wavelength, the structure can be approximated as a uniform medium with an effective value for the conductivity. In order to simplify the solution, a lossy isotropic model for multilayer conductive

composites has been introduced in [24]. By assuming an isotropic model for each layer and applying the TMM, the shielding analysis of such a multilayer medium can be easily performed. However, the isotropic model may not be very accurate when the anisotropic behavior in each individual layer is important. The conductivity in each layer of RCCF is high along the direction of fibers (σ_x'), but low in the perpendicular direction (σ_y') so that $\sigma_x'/\sigma_y' >> 1$ [39]. In [36][45],[46], the plane-wave shielding properties of multilayer RCCF composites are studied by using the homogeneous anisotropic bulk model of the structure. Each layer is characterized by an anisotropic permittivity tensor. Since the carbon fiber composite is a non-magnetic medium, the permeability of composites is considered as free space permeability (μ_0). The proposed anisotropic bulk model shows much better accuracy than isotropic model particularly at high frequencies and also when the fibers in different layers are in different directions. By using the anisotropic model of each layer, the main structure is converted to a multilayer anisotropic medium, making the TMM suitable to characterize the shielding properties of the structure.

2.1 Effective Anisotropic Models of RCCF Composite

Although the one-layer anisotropic homogeneous model can be efficiently used, it cannot predict the shielding behavior of composite at high frequencies. Two other types of anisotropic equivalent-models have been introduced for one-layer composite, namely three-layer homogeneous and inhomogeneous models [25], [47]. The models are shown in Figure 2.2. These models include more of the internal detail of the structure so that high frequency behavior such as resonances can be captured. In the three-layer model,

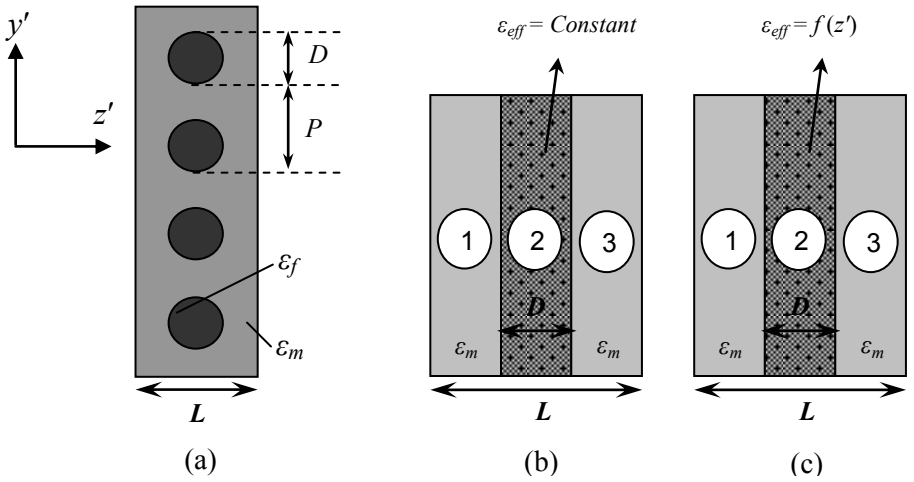

Figure 2.2. (a) RCCF composite, (b) three-layer homogeneous model, (c) three-layer inhomogeneous model [25].

each layer of composite is divided to three sub-layers. The middle sub-layer includes the conducting fibers and is represented with an effective anisotropic homogeneous or inhomogeneous medium. Although the homogeneous model shown in Figure 2.2(b) increases the validity of composite model for higher frequencies, it cannot capture the resonant behavior at high frequencies for some cases. The resonances at high frequencies occur due to a phenomenon called as "grating effect" of periodic structures. When the separation distance between fibers are in the order of wavelength, the periodic structure lets the electric field parallel to fibers go through and as a result, SE drops. The three-layer inhomogeneous model is proposed to increase the validity of model. Similar to three-layer homogeneous model, in this case each layer is divided to three parts. The middle part is an inhomogeneous medium with effective permittivity tensor given by [25]

$$\varepsilon_{y'}^{-1} = (1-g)\varepsilon_m^{-1} + g\varepsilon_f^{-1} \tag{2.1}$$

$$\varepsilon_{x'} = \varepsilon_{z'} = (1-g)\varepsilon_m + g\varepsilon_f \tag{2.2}$$

where $g = 2\sqrt{Dz' - z'^2} / P$. For the homogeneous model, g is equal to $\pi D/4P$ which is the ratio of fiber cross section area to the total cross section area at the middle layer. The inhomogeneous property of middle layer is due to the variation of structure geometry along the z direction. When a wave reaches to the middle layer and propagates through, the wave sees an increasing cross-section of the fiber until the center of the fiber and then the wave sees a decreasing fiber cross-section. The three-layer inhomogeneous layer represents much more of the detail of structure so that the accuracy of this model is high for a very wide range of frequency. Using the effective anisotropic models, we study the SE characteristics of RCCF composite by applying the TMM technique. Since the electromagnetic properties of an anisotropic medium are completely different from an isotropic one, the plane wave propagation inside these kinds of material is first briefly explained.

2.2 Plane Wave Propagation in Anisotropic Materials

An anisotropic medium is described with a dielectric tensor, given by

$$\bar{\varepsilon} = \begin{bmatrix} \varepsilon_{x_1} & 0 & 0 \\ 0 & \varepsilon_{y_1} & 0 \\ 0 & 0 & \varepsilon_{z_1} \end{bmatrix} \tag{2.3}$$

where ε_{x_1}, ε_{y_1} and ε_{z_1} are the permittivities along the principal axes (x_1 , y_1, z_1). Generally, the principal axes do not correspond to the global coordinate directions (x, y, z). Therefore, the dielectric tensor in xyz coordinates can be written as

$$\bar{\varepsilon} = T \begin{bmatrix} \varepsilon_{x_1} & 0 & 0 \\ 0 & \varepsilon_{y_1} & 0 \\ 0 & 0 & \varepsilon_{z_1} \end{bmatrix} T^{-1} \tag{2.4}$$

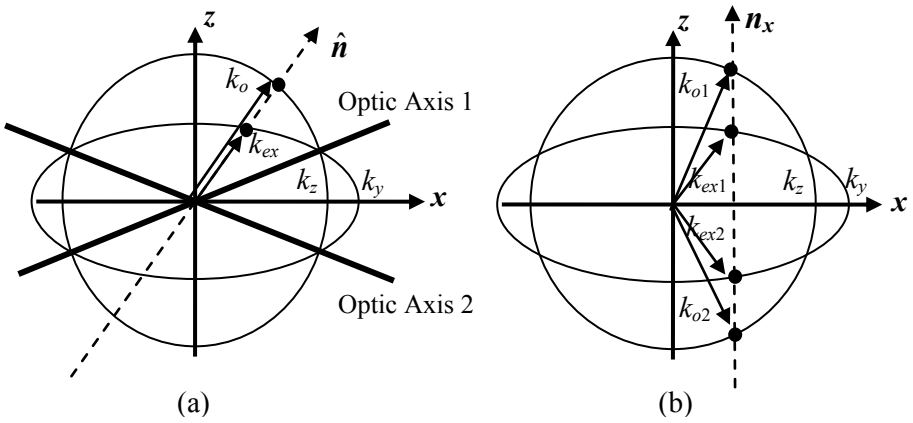

Figure 2.3. (a) A plane wave in anisotropic media with specific $\hat{\boldsymbol{n}}$ [48]. (b) A plane wave in anisotropic media with specific n_x.

where T is the coordinate rotation matrix. Hence, in global xyz coordinates, we have a non-diagonal dielectric tensor given by

$$\bar{\varepsilon} = \begin{bmatrix} \varepsilon_{xx} & \varepsilon_{xy} & \varepsilon_{xz} \\ \varepsilon_{yx} & \varepsilon_{yy} & \varepsilon_{yz} \\ \varepsilon_{zx} & \varepsilon_{zy} & \varepsilon_{zz} \end{bmatrix}. \tag{2.5}$$

For the following analysis, we assume that the principal axes coincide with xyz axes. The plane wave may be represented as

$$\boldsymbol{E} = \boldsymbol{E_0}\, e^{-jk\hat{\boldsymbol{n}}.\boldsymbol{r}} \tag{2.6}$$

where

$$\hat{\boldsymbol{n}} = \boldsymbol{x}n_x + \boldsymbol{y}n_y + \boldsymbol{z}n_z \tag{2.7}$$

and $k_0^2 = \omega^2\mu\varepsilon_0$, $k_x^2 = \varepsilon_x k_0$, $k_y^2 = \varepsilon_y k_0$, $k_z^2 = \varepsilon_z k_0$. Using Maxwell equations we have [48]

$$\boldsymbol{n}\times(\boldsymbol{n}\times\boldsymbol{E}) + \omega^2\mu\bar{\varepsilon}\cdot\boldsymbol{E} = 0. \tag{2.8}$$

When the principal axes coincide with the xyz axes, if we set the determinant of coefficients in (2.8) to zero, we obtain

$$\frac{n_x^2 k_x^2}{k^2 - k_x^2} + \frac{n_y^2 k_y^2}{k^2 - k_y^2} + \frac{n_z^2 k_z^2}{k^2 - k_z^2} = 0. \tag{2.9}$$

The solution to this "dispersion equation" is always a spherical surface and an ellipsoid. For example, if we assume the *xz* plane ($n_y = 0$), (2.9) becomes

$$(k^2 - k_y^2)\left[n_x^2 k_x^2 (k^2 - k_z^2) + n_z^2 k_z^2 (k^2 - k_x^2)\right] = 0. \tag{2.10}$$

As shown in Figure 2.3 , for a specific vector $\hat{\boldsymbol{n}}$, by regarding the forward and backward propagation, we have generally four propagation constants. Figure 2.3(a) shows the propagation constants of a plane wave in the specific direction of $\hat{\boldsymbol{n}}$. In Figure 2.3(b), the propagation constants for waves with a specific n_x value are illustrated. The constants k_o and k_{ex} are associated with "ordinary" and "extraordinary" modes, respectively. Where the circle and the oval intersect each other, we have a single value of the propagation constant for that one specific direction, and that direction is called an "optical axis". It should be noted that in some planes the circle and ellipse do not intersect. Since both ordinary and extraordinary modes are excited inside an anisotropic medium, the TMM formulation of multilayer anisotropic media is expressed as a 4×4 matrix rather than two 2×2 matrices as for isotropic media. It should be noted that when the principal axis is not parallel to the *xyz* coordinates, coupling between ordinary and extraordinary modes exists.

2.2.1 Shielding Analysis of Multilayered RCCF Using Transmission Matrix Method

It was noted above that the equivalent models can predict the electromagnetic properties of composites. The three-layer anisotropic inhomogeneous model is the most accurate equivalent one among proposed equivalent models. The effective parameters of

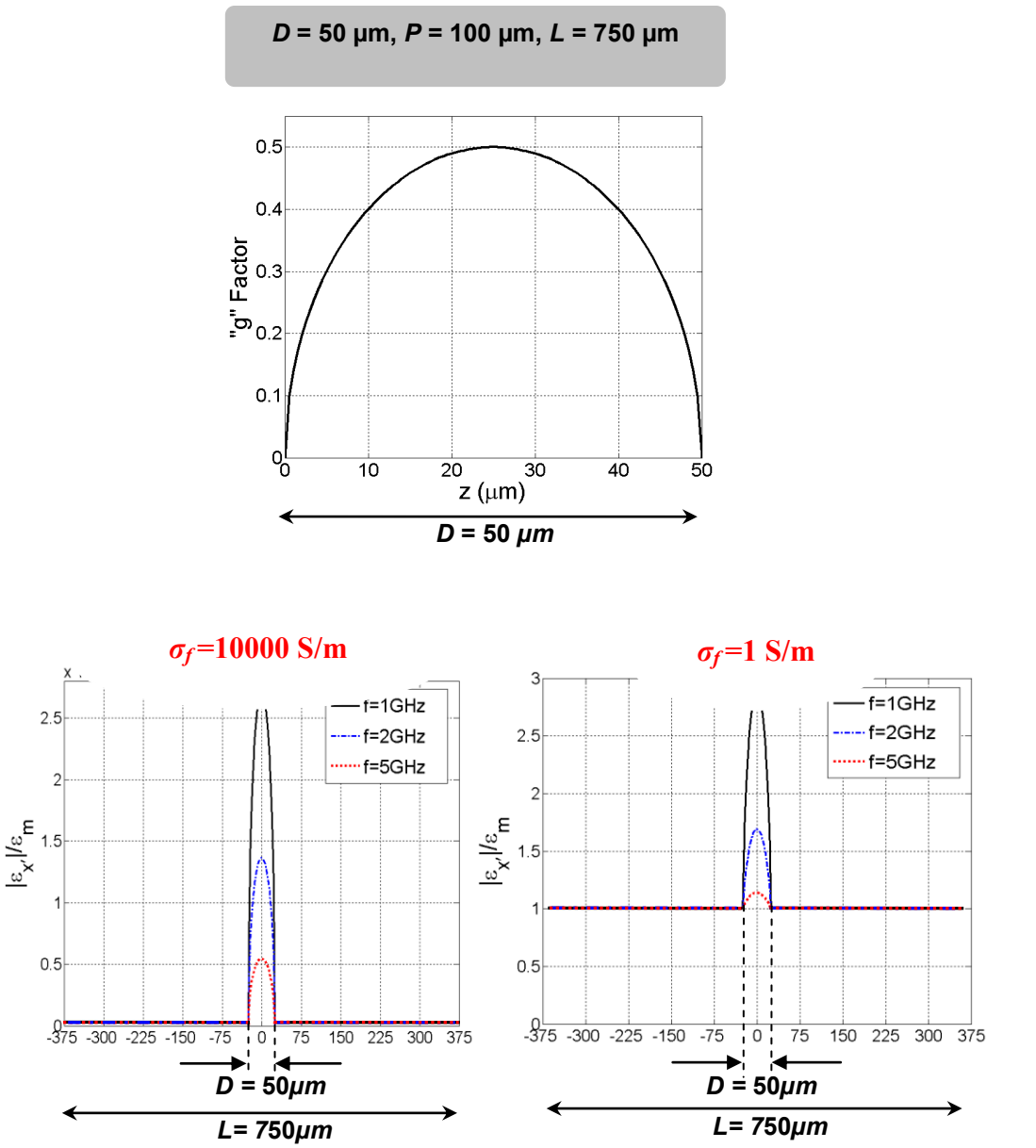

Figure 2.4. The *g*-factor and magnitude of permittivity inside composite layer characterized by equivalent inhomogeneous model.

composites displayed in Figure 2.2 can be obtained from (2.1). Figure 2.4 shows the calculated magnitude of permittivity along the fiber direction in the layer at three different frequencies. It is observed that at the permittivity of middle region has a considerable inhomogeneous behavior.

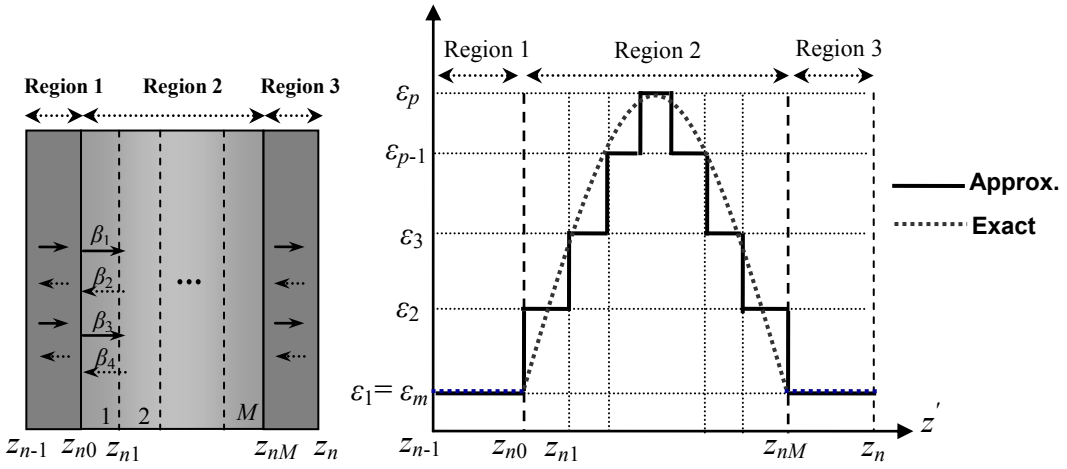

(a) (b)

Figure 2.5. Dividing inhomogeneous layer to several homogeneous sub-layers.

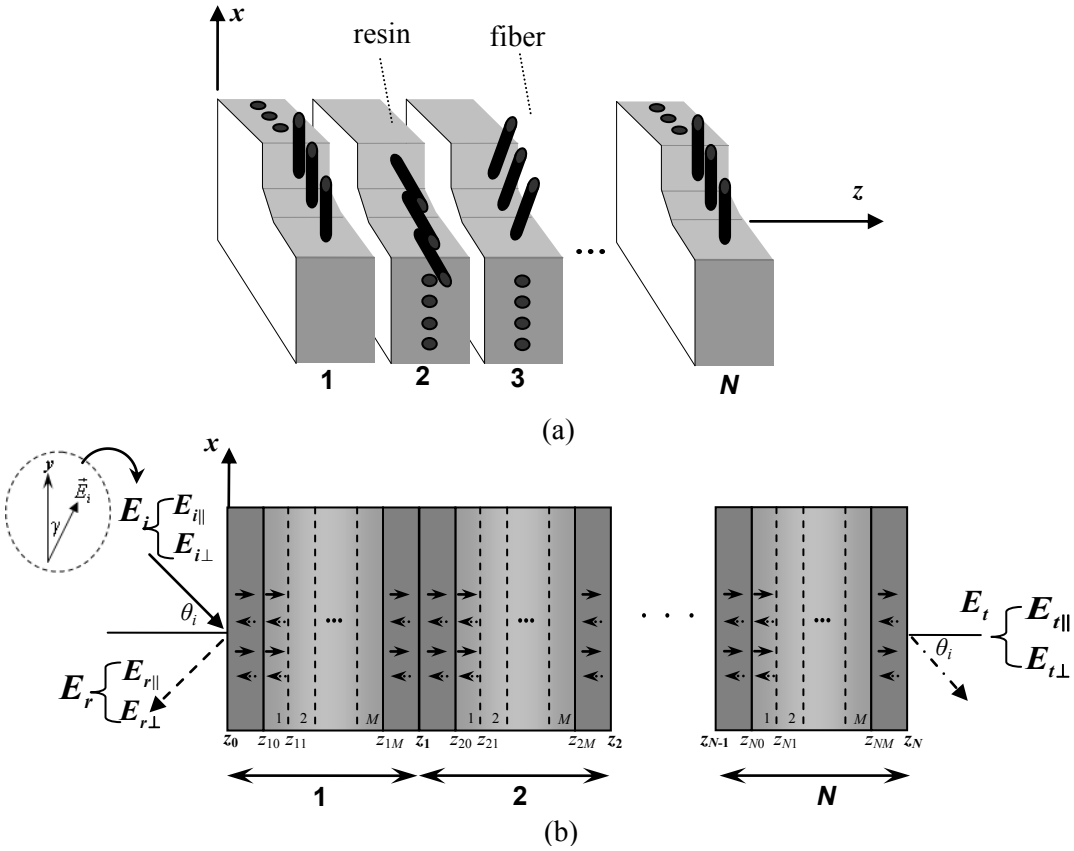

Figure 2.6. Multilayer RCCF composite inhomogeneous model characterized by a number of homogeneous sub-layers.

In order to convert an inhomogeneous problem to a homogeneous one, we may split each inhomogeneous layer to *M* homogeneous sub-layers as displayed in Figure 2.5. By doing so, it is observed that each layer of a multilayer reinforced composite comprises *M*+2 layers. The number of sub-layers *M* depends on how rapidly the permittivity changes with distance and by choosing higher values, the results would converge better. After converting the inhomogeneous medium to a multilayer homogeneous one, we obtain the multilayer anisotropic model shown in Figure 2.6. The TMM technique along with anisotropic medium characteristics is used to solve the problem.

2.3 Incident Plane Wave on Multilayer Anisotropic Medium

As shown in Figure 2.7, the reinforced composite can be modeled as one anisotropic medium with principal axis (x', y', z') so that x' and z' are parallel to fiber direction and z-axis, respectively. The angle of reinforced-fiber direction to the global coordination axis is assumed as φ. By solving Maxwell's equations in each layer, the TMM is applied to find the SE of multilayer composites. The dielectric constant and conductivity tensor are

$$\bar{\varepsilon} = \begin{bmatrix} \varepsilon_{x'} & 0 & 0 \\ 0 & \varepsilon_{y'} & 0 \\ 0 & 0 & \varepsilon_{z'} \end{bmatrix} \tag{2.11}$$

and

$$\bar{\sigma} = \begin{bmatrix} \sigma_{x'} & 0 & 0 \\ 0 & \sigma_{y'} & 0 \\ 0 & 0 & \sigma_{z'} \end{bmatrix} \tag{2.12}$$

in $x'y'z'$ coordinates, and are not diagonal in xyz coordinates. In case the layers are lossy, we combine the real permittivity and conductivity into a complex permittivity,

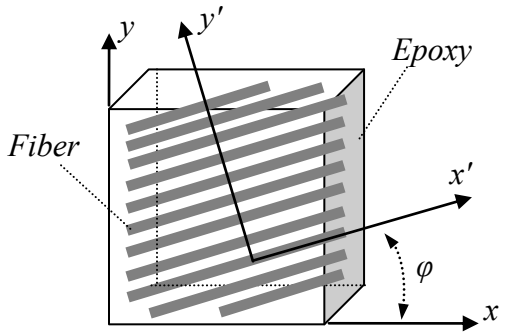

Figure 2.7. Composite material with reinforced carbon fibers.

$\bar{\varepsilon} = \varepsilon_0(\bar{\varepsilon}_r + \frac{\bar{\sigma}}{j\omega})$. By using the coordinate rotation matrix *T*, the dielectric tensor becomes

$$\bar{\varepsilon} = \begin{bmatrix} \varepsilon_{xx} & \varepsilon_{xy} & 0 \\ \varepsilon_{yx} & \varepsilon_{yy} & 0 \\ 0 & 0 & \varepsilon_{zz} \end{bmatrix} \tag{2.13}$$

where

$$\varepsilon_{xx} = \varepsilon_{y'} \sin^2 \varphi + \varepsilon_{z'} \cos^2 \varphi \tag{2.14}$$

$$\varepsilon_{yy} = \varepsilon_{y'} \cos^2 \varphi + \varepsilon_{x'} \sin^2 \varphi \tag{2.15}$$

$$\varepsilon_{zz} = \varepsilon_{z'} \tag{2.16}$$

$$\varepsilon_{xy} = \varepsilon_{yx} = (\varepsilon_{y'} - \varepsilon_{x'}) \sin\varphi \cos\varphi. \tag{2.17}$$

A plane wave can be decomposed into parallel and perpendicular components, corresponding to the parallel and perpendicular polarization. As explained earlier, when an anisotropic medium is excited by a plane wave, we have two ordinary and extraordinary modes with different propagation constants. When principal coordinate directions coincide with the global coordinates, each parallel mode and perpendicular mode excitation separately leads to ordinary and extraordinary modes and there is no coupling between these modes. However, when principal axes are not parallel to the

global axes, coupling between two modes exists which leads to coupled equations. The solution of such a problem is explained as follows. The incident plane wave is given by

$$\boldsymbol{E} = \boldsymbol{E_0} e^{-jk\hat{\boldsymbol{n}}.\boldsymbol{r}} = \boldsymbol{E_0} e^{-j(k_x x + k_y y + k_z z)} \tag{2.18}$$

By substituting (2.14)-(2.18) in Maxwell's equations, we obtain:

$$\begin{bmatrix} \omega^2\mu\varepsilon_{xx} - k_y{}^2 - k_z{}^2 & \omega^2\mu\varepsilon_{xy} + k_x k_y & \omega^2\mu\varepsilon_{xz} + k_x k_z \\ \omega^2\mu\varepsilon_{yx} + k_x k_y & \omega^2\mu\varepsilon_{yy} - k_x{}^2 - k_z{}^2 & \omega^2\mu\varepsilon_{yz} + k_y k_z \\ \omega^2\mu\varepsilon_{zx} + k_x k_z & \omega^2\mu\varepsilon_{zy} + k_y k_z & \omega^2\mu\varepsilon_{zz} - k_x{}^2 - k_z{}^2 \end{bmatrix} [E] = 0. \tag{2.19}$$

In a multilayer anisotropic media, as shown in Figure 2.8, the parameters k_x and k_y should be constant in all layers to satisfy the boundary condition at interfaces. Moreover, for convenience suppose that the plane wave is incident in the x-z plane, and hence $k_y = 0$. Therefore given (k_x, k_y) and the dielectric tensors(2.14)-(2.17), the roots of the coefficient matrix determinant give us the propagation constants k_{zi} as

$$\begin{vmatrix} \omega^2\mu\varepsilon_{xx} - k_z{}^2 & \omega^2\mu\varepsilon_{xy} & k_x k_z \\ \omega^2\mu\varepsilon_{yx} & \omega^2\mu\varepsilon_{yy} - k_x{}^2 - k_z{}^2 & 0 \\ k_x k_z & 0 & \omega^2\mu\varepsilon_{zz} - k_x{}^2 - k_z{}^2 \end{vmatrix} = 0 \tag{2.20}$$

which leads to

$$A_1 k_z{}^4 + A_2 k_z{}^2 + A_3 = 0 \tag{2.21}$$

where

$$\begin{aligned} A_1 &= \omega^2\mu\varepsilon_{zz} \\ A_2 &= k_x{}^2\omega^2\mu(\varepsilon_{xx} + \varepsilon_{zz}) - \omega^4\mu^2\varepsilon_{zz}(\varepsilon_{xx} + \varepsilon_{yy}) \\ A_3 &= \omega^2\mu(\omega^2\mu\varepsilon_{zz} - k_x{}^2)\left[\varepsilon_{xx}(\omega^2\mu\varepsilon_{yy} - k_x{}^2) - \omega^2\mu\varepsilon_{xy}\varepsilon_{yx}\right]. \end{aligned} \tag{2.22}$$

By solving (2.21), four wave vectors ($\boldsymbol{K_i}$ vectors) are obtained which are related to ordinary and extraordinary modes which are forward and backward in the z-direction

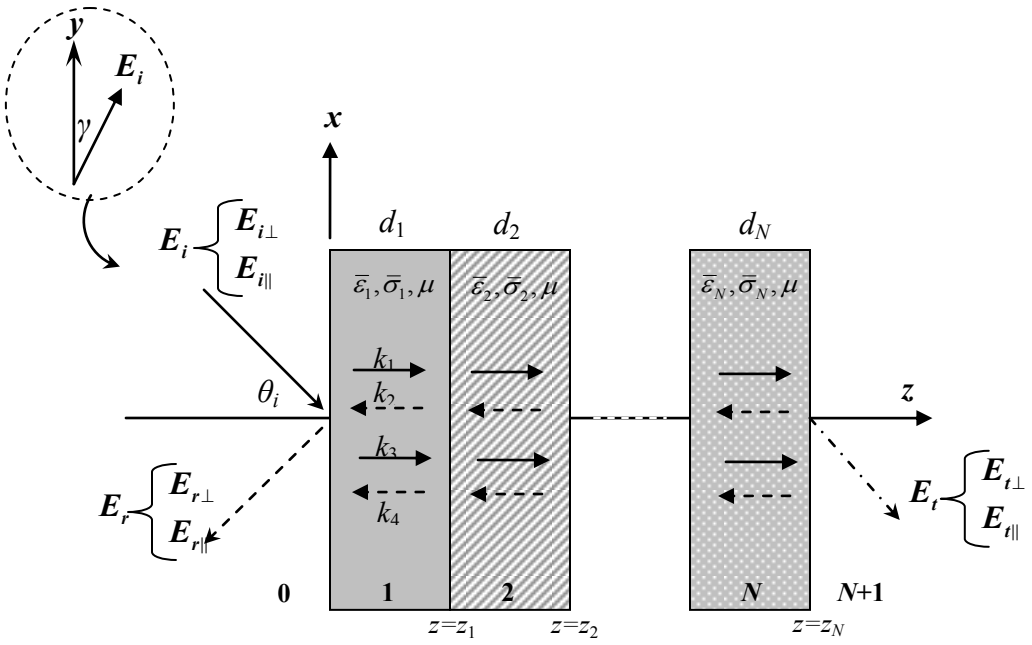

Figure 2.8. Multilayer anisotropic media excited by an incident plane wave.

$$\boldsymbol{K_i} = k_x \boldsymbol{x} + k_{zi} \boldsymbol{z} \qquad (i = 1,2,3,4) \tag{2.23}$$

with the corresponding polarization vectors

$$\boldsymbol{p_i} = p_{ix} \boldsymbol{x} + p_{iy} \boldsymbol{y} + p_{iz} \boldsymbol{z} \tag{2.24}$$

in which

$$\begin{aligned} p_{ix} &= (\omega^2 \mu \varepsilon_{yy} - k_x{}^2 - k_{zi}{}^2)(\omega^2 \mu \varepsilon_{zz} - k_x{}^2 - k_{zi}{}^2) \\ p_{iy} &= \omega^2 \mu \varepsilon_{yx} (-\omega^2 \mu \varepsilon_{zz} + k_x{}^2 + k_{zi}{}^2) \\ p_{iz} &= k_x \beta (-\omega^2 \mu \varepsilon_{yy} + k_x{}^2 + k_{zi}{}^2) \end{aligned} \tag{2.25}$$

Also the vector $\boldsymbol{p_i}$ can be normalized by using normalization constant ($\boldsymbol{p_i} / |\boldsymbol{p_i}|$). Hence, as shown in Figure 2.8, in each layer two transmitted and two reflected waves exist. We can write the electric field as

$$\boldsymbol{E} = \sum_{i=1}^{4} C_i \, \boldsymbol{p_i} \, e^{-j(k_x x + k_{zi}(z - z_m))}. \tag{2.26}$$

By applying the Maxwell equations, the *H*-field is

$$\boldsymbol{H} = \sum_{i=1}^{4} C_i \, \boldsymbol{s}_i \, e^{-j(k_x x + k_{zi}(z - z_m) - \omega t)} \quad , \quad \boldsymbol{s}_i = \frac{1}{\omega\mu}(\boldsymbol{K}_i \times \boldsymbol{p}_i). \tag{2.27}$$

Imposing the boundary conditions for tangential electric and magnetic fields, we are able to ensure continuity between layers m and m-1 with

$$\begin{bmatrix} C_1(m-1) \\ C_2(m-1) \\ C_3(m-1) \\ C_4(m-1) \end{bmatrix} = D^{-1}(m-1)D(m)P(m) \begin{bmatrix} C_1(m) \\ C_2(m) \\ C_3(m) \\ C_4(m) \end{bmatrix} \tag{2.28}$$

where

$$D(m) = \begin{bmatrix} r_{1x}(m) & r_{2x}(m) & r_{3x}(m) & r_{4x}(m) \\ s_{1y}(m) & s_{2y}(m) & s_{3y}(m) & s_{4y}(m) \\ r_{1y}(m) & r_{2y}(m) & r_{3y}(m) & r_{4y}(m) \\ s_{1x}(m) & s_{2x}(m) & s_{3x}(m) & s_{4x}(m) \end{bmatrix} \tag{2.29}$$

and

$$P(m) = \begin{bmatrix} e^{jk_{z1}(m)d_m} & 0 & 0 & 0 \\ 0 & e^{jk_{z2}(m)d_m} & 0 & 0 \\ 0 & 0 & e^{jk_{z3}(m)d_m} & 0 \\ 0 & 0 & 0 & e^{jk_{z4}(m)d_m} \end{bmatrix}. \tag{2.30}$$

D and P are called dynamical and propagation matrices. The dynamical matrix will be diagonal if the coupling between modes does not exist. The matrix R is the coordinate rotation matrix which is applied to avoid singularity of some inverse matrixes. Finally the relation between fields in regions 0 and N+1 is

$$\begin{bmatrix} C_1(0) \\ C_2(0) \\ C_3(0) \\ C_4(0) \end{bmatrix} = D_0^{-1}R^{-1} \left[\prod_{m=1}^{N} D(m)P(m)D^{-1}(m) \right] D_0 R \begin{bmatrix} C_1(N+1) \\ C_2(N+1) \\ C_3(N+1) \\ C_4(N+1) \end{bmatrix} \tag{2.31}$$

and

$$D_0 = \begin{bmatrix} 0 & 0 & \cos\theta_i & \cos\theta_i \\ 0 & 0 & \frac{1}{\omega\mu}(k_x \sin\theta_i + k_{z0}\cos\theta_i) & \frac{1}{\omega\mu}(-k_x \sin\theta_i - k_{z0}\cos\theta_i) \\ 1 & 1 & 0 & 0 \\ -\frac{k_{z0}\cos\theta_i}{\omega\mu} & \frac{k_{z0}\cos\theta_i}{\omega\mu} & 0 & 0 \end{bmatrix} \tag{2.32}$$

where $k_{z0} = \omega\sqrt{\mu\varepsilon_0}\cos\theta_i$ and θ_i is the incidence angle as shown in Figure 2.8. Finally, by given incident plane wave with arbitrary propagation direction, after some mathematical procedures, the SE of multilayer composite can be obtained as

$$SE = 20\log\left(\frac{|\boldsymbol{E}_i|}{|\boldsymbol{E}_t|}\right) \tag{2.33}$$

in which $|\boldsymbol{E}_t|$ and $|\boldsymbol{E}_i|$ can be expressed in terms of C_i coefficients using (2.26) .

2.3.1 Simulation Results Using Three-Layer Anisotropic Inhomogeneous Model

By implementing the above code, we generate the simulation results for some case studies. By setting t = 3 mm, $\varepsilon_{rm} = \varepsilon_{rf} = 2$, σ_f = 10000 S/m, D = 0.05mm, P = 0.1 mm, L = 0.75 mm, the SE of a four-layer composite using two different models, namely the anisotropic one-layer homogeneous model and the three-layer inhomogeneous model, is calculated as displayed in Figure 2.9. It is observed in Figure 2.9(a), for the $E_{\|}$-mode that at high frequencies, the three layer inhomogeneous model agrees much better with the FEM result than does the one-layer homogeneous model. FEM is a well-known full-wave numerical technique which is based on discretization of structure to a number of elements/meshes [49].

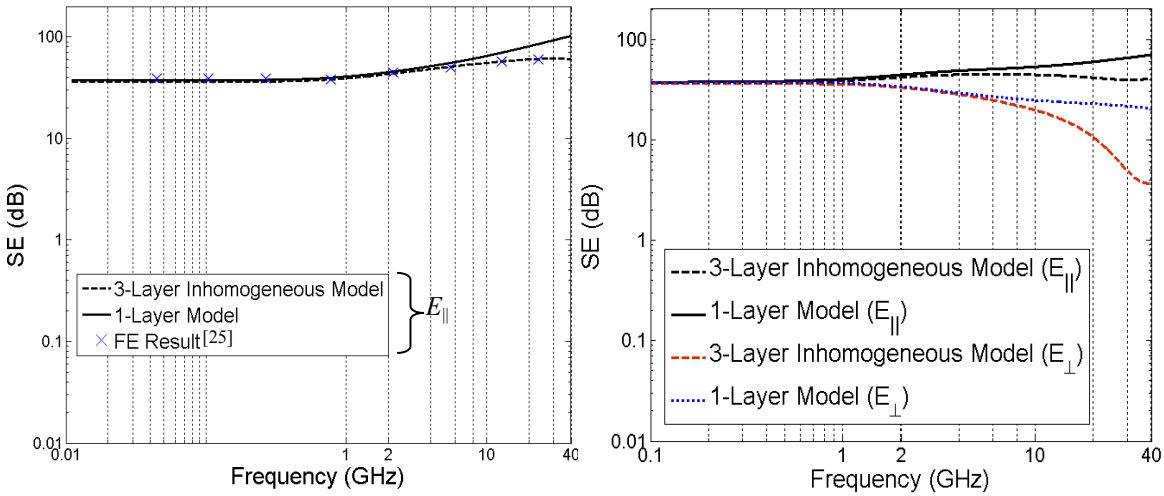

Figure 2.9. SE of four layer composite, (a) (0/90/0/90), (b) (0/30/90/-60).

The inhomogeneous model includes more details of the structure such that it can predict the high frequency behavior much better than the homogeneous model. As shown in Figure 2.9(b), the SE shows highly different behavior for two different electric field polarizations ($E_{\|}$ and $E\perp$). Since in RCCF composites there is a coupling between modes, the shielding properties could be very different for parallel and perpendicular modes as observed in Figure 2.9(b).

2.3.2 Simulation Results Using One-Layer Anisotropic Homogeneous Model

Here, the SE of multilayer composite laminates is obtained analytically by using the 1-layer anisotropic homogeneous model of each layer along with the TMM technique. The SE sensitivity analysis is performed as a function of fiber orientation and plane wave parameters, which are the angle of incidence and the polarization of the electric field. The SE of 1 mm-thick 8-layer and 12-layer composites are calculated for different fiber

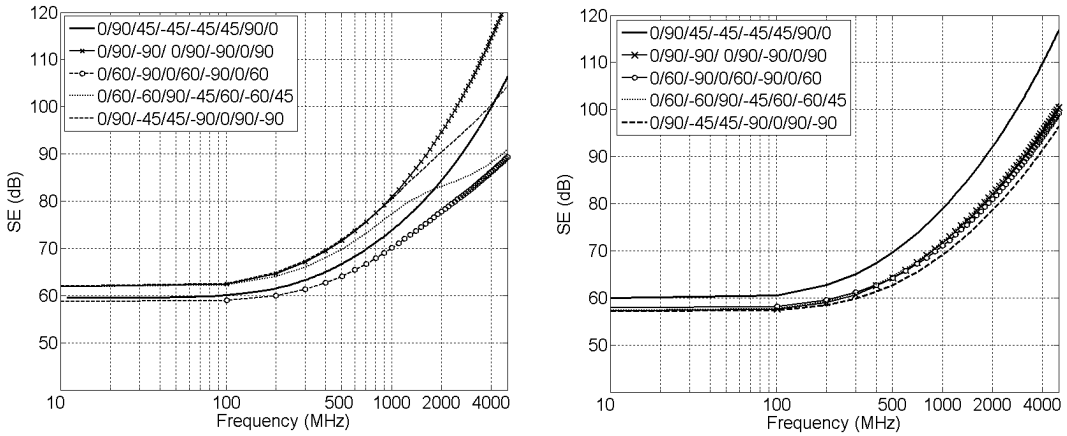

Figure 2.10. SE of 8-layer reinforced composite material, (a) perpendicular *E*-field ($E\perp$), (b) parallel *E*-field ($E_{\parallel}$).

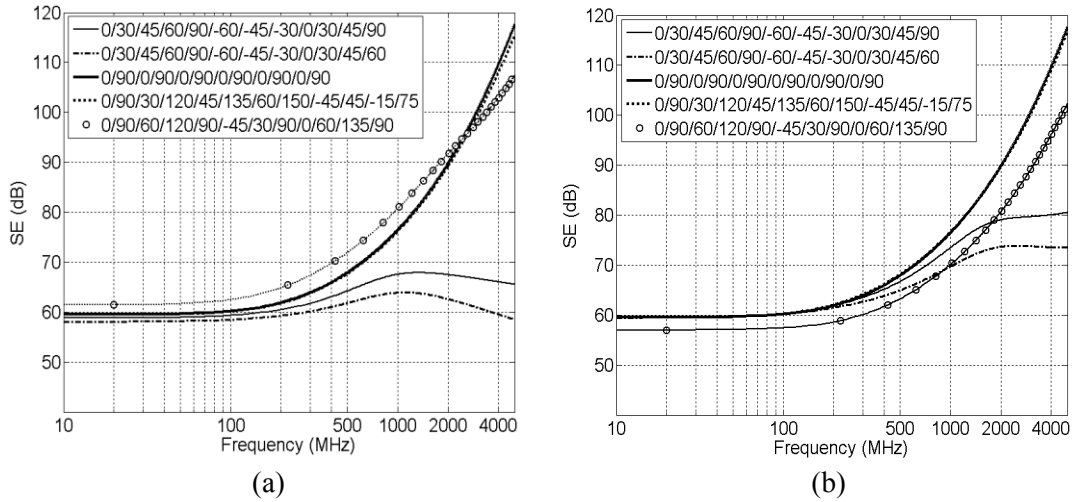

Figure 2.11. SE of 12-layer reinforced composite material, (a) perpendicular *E*-field ($E\perp$), (b) parallel *E*-field ($E_{\parallel}$).

orientation patterns in Figure 2.10 and Figure 2.11, respectively. The relative permittivity is considered as 3.3 for all layers and the conductivity tensor in principal coordinate is $\bar{\sigma} = (10000, 0.1, 0.2)\, S/m$ for all cases. It can be observed that at frequencies greater than 1 GHz, we have more than 10 dB difference between SE for various orientation patterns in both $E\perp$ and $E_{||}$ cases, which can be explained as follows. Due to the coupling between modes in anisotropic layers, both components of the electric field, E_x and E_y, always exist

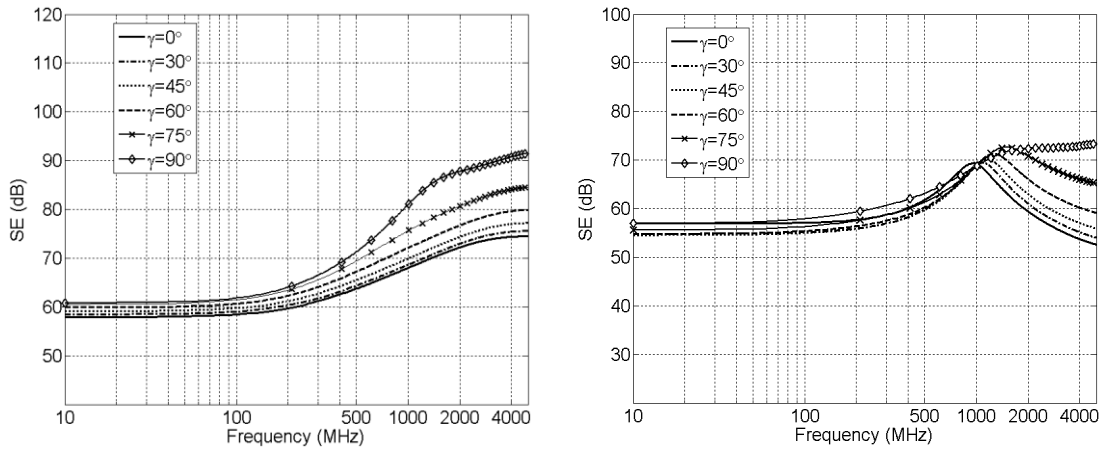

(a) (b)

Figure 2.12. The effect of polarization angle on SE, (a) 12-layer and (b) 8-layer composites.

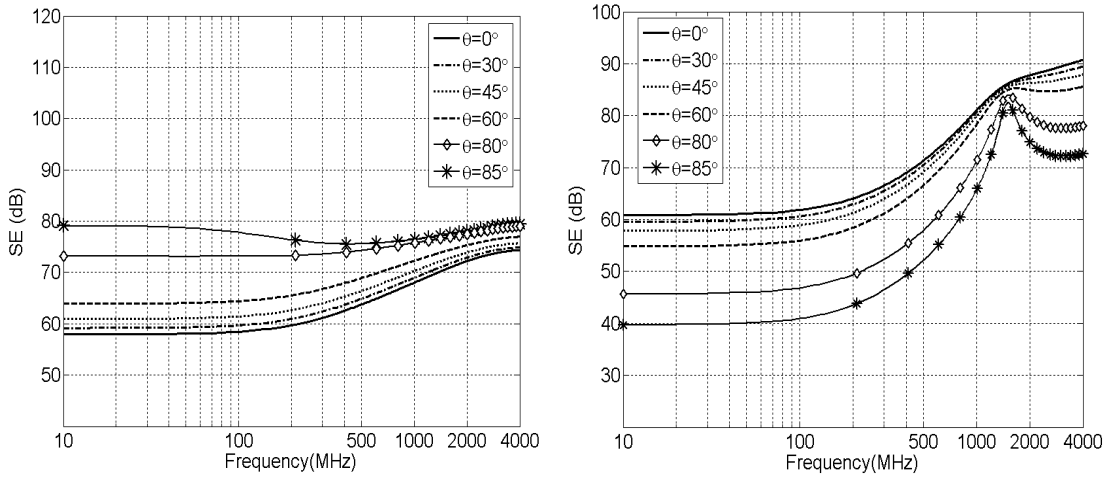

(a) (b)

Figure 2.13. The effect of incident angle on SE, (a) $E\perp$ and (b) $E_{||}$.

independent of the polarization of the incident plane wave. Hence, the different orientation patterns have different effects on the attenuation of these components. On the other hand, the orientation of fibers can be used to control the shielding effectiveness of multilayer composites at the frequency range of interest. It should be noted that the SE calculated in Figure 2.10 and Figure 2.11 is just for $E\perp$ and $E_{||}$ modes which are correspond to γ = 0º and γ = 90º, respectively. Figure 2.12 shows the effect of the

polarization angle γ on the SE of 8-layer (0/30/60/90/90/60/30/0) and 12-layer (0/30/45/90/-45/-30/0/30/45/90/-45/-30) composite materials. It can be seen that the SE changes considerably with the polarization angle γ at higher frequencies. The effect of incidence angle θ on the SE is calculated for $E\perp$ and $E_{||}$ modes in Figure 2.13(a) and Figure 2.13(b), respectively. It is observed that the SE decreases for $E_{||}$ and increases for $E\perp$ as the incidence angle increases. The reflection coefficient between air and a highly lossy material decreases in the $E_{||}$ case as the incidence angle increases from zero up to the angles close to the grazing incidence [50]. As a result, the power transmission increases for the $E_{||}$ mode versus incidence angle. Contrarily, in the $E\perp$ case, the transmission coefficient and as a result the SE decreases as the incidence angle increases.

2.4 Measurement Setups and Experimental Results

In order to use composites in industry, the measurement result of shielding properties is a key factor which should be presented to verify the performance of a composite experimentally. Actually the numerical and analytical models are often used to understand the electromagnetic properties of a material and to obtain a design outline to get better SE. In a design outline, one may provide a table showing the effect of different parameters like sample thickness, fiber orientation, carbon concentration on SE of composite. Different types of measurement setups are used to evaluate the SE of composites experimentally [51]-[55]. For example, the dual TEM-cell setup [51], lens antennas for free space measurements [52], the coaxial cable fixture [53][54] and standard waveguide setups [22][55] can be used for shielding measurements. Choosing the appropriate kind of measurement setup depends on the frequency range of interest.

The coaxial cable fixture is one of the most common setups. This setup is widely used for low-frequency SE measurements. The cut-off frequency of a coaxial cable depends on the diameter of inner and outer conductor so that a coaxial cable with 33mm and 76mm diameters has a 1.7 GHz cut-off frequency and with 6mm and 14mm has a 9.5 GHz cut-off frequency. Since the plane wave parameters (incident angle and polarization angle) affect the SE, it is important to determine the plane wave parameters in measurement setups. In the coaxial cable fixture, the incident angle is normal because the propagation mode is transverse electromagnetic (TEM). And because of electric field vector is in the radial direction, all polarizations altogether are tested in the SE measurement. However, the operating frequency range is limited by cut-off frequency of next mode (TE_{11}) in the coaxial cable fixture. Above the TE_{11} cut-off frequency other modes exist and the results of an SE measurement become difficult to interpret.

To cover a wide frequency range a set of standard waveguide setups can be used, each over a limited frequency range where only the dominant mode propagates. Thus, we can measure SE by using G-, X-, Ku- and K-band waveguides. The dimensions of standard waveguides and their operating frequency ranges are given in [56].

In a waveguide setup, the fundamental mode is TE_{10} with the electric field distribution as shown in Figure 2.14(a). The *y*-directed electric field distribution is

$$E_y = A\sin\left(\frac{\pi x}{a}\right)e^{-j\beta z} \tag{2.34}$$

where β is the propagation constant of dominant mode. Equation (2.34) can be re-written as

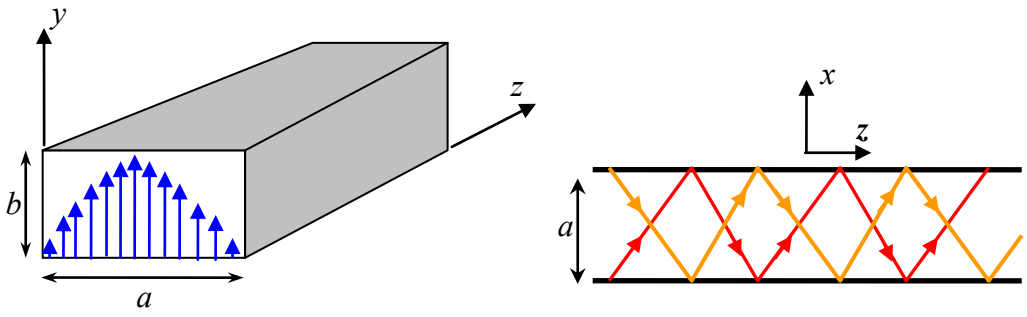

(a) (b)

Figure 2.14. Rectangular waveguide setup, (a) TE_{10} electric field distribution at cross-section, (b) Waveguide top-view along with two plane-wave rays.

$$E_y = \left(\frac{A}{2j}\right)\left(e^{j\left(\frac{\pi x}{a}-\beta z\right)} - e^{j\left(-\frac{\pi x}{a}-\beta z\right)}\right). \tag{2.35}$$

From (2.35) and observing Figure 2.14(b), we find that the incident wave in a waveguide is composed of two oblique-incident plane waves with constant amplitude.

It is important to note that the waveguide setup tests the SE with the electric field oriented in the *y* direction and so for anisotropic materials, the results will depend on the orientation of the sample in the waveguide. Although the waveguide setup tests the SE for a particular incidence direction, it is in *xz*-plane and not *yz* so that the polarization of the electric field does not depend on the incidence angle.

As experimental setup for low frequency measurements, up to 1.7 GHz, we used the coaxial cable fixture shown in Figure 2.15(a). A one-layer RCCF sample was fabricated in CONCOM laboratory using the following procedure [57]. Provided by Hexion Specialty Chemicals [58], the mixture of epoxy resin Epon 862 and the curing agent (26.4 *wt*%) Epikure W was degassed in a vacuum oven at 90 °C for 30 min. After impregnating

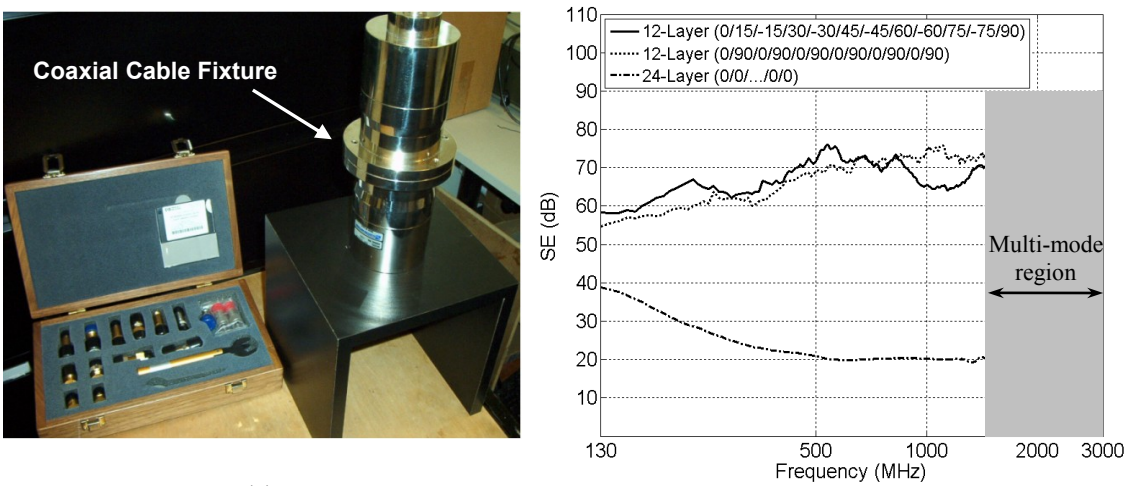

(a) (b)

Figure 2.15. (a) Coaxial cable fixture, (b) Measurement results.

one ply of unidirectional carbon cloth (T300), produced by MF Composites [59], with the mixture between two aluminum plates coated with demolding agent, the plates were tightened. Then, the composite was cured at 120°C for 6 hours. The thickness of sample is 0.399 mm.

Using an HP8720 network analyzer, the SE of three fabricated composite samples was measured as shown in Figure 2.15(b). There are two samples of RCCF composite that are 4.5 mm thick and have 12 layers. The orientation of the fibers is different in the two samples. In one it is 0/15/-15/30/-30/45/-45/60/-60/75/-75/90 and in the other it is 0/90/0/90/0/90/0/90/0/90/0/90. The third sample is 6 mm thick and has 24 layers. The measured SE in Figure 2.15(b) shows that even though the thickness of 24-layer sample is one-third larger than that of the 12-layer samples, the SE of 24-layer composite is much less than 12-layer one. It is owing to this fact that the fiber orientations of all layers in 24-layer sample are in the same direction, and so only block the component of the electric field parallel to the fibers, and not the perpendicular component.

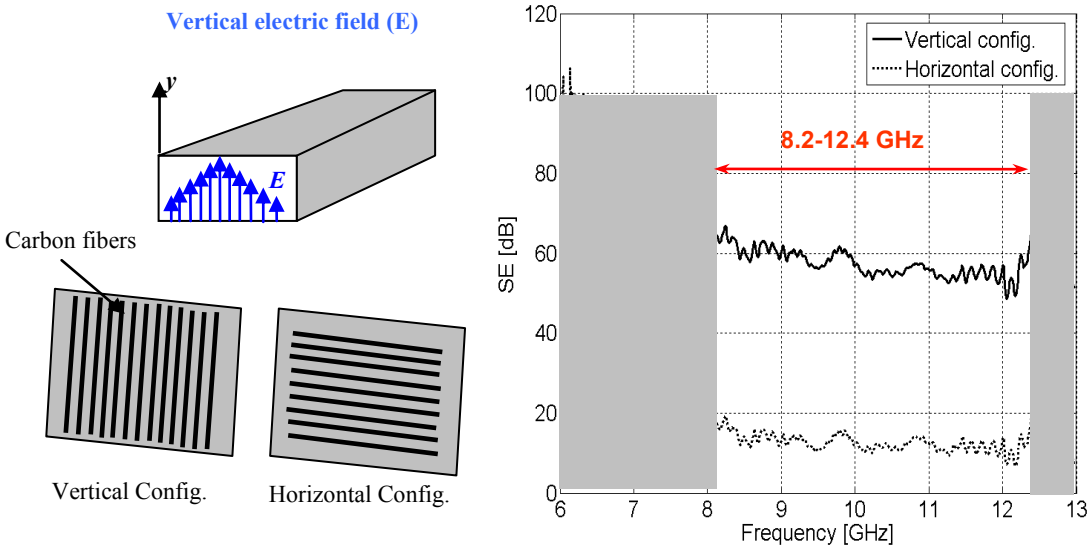

Figure 2.16. SE for two different configurations using waveguide measurement setup.

Note in Figure 2.15(b) that the SE of the two 12 layer samples is similar, but is different in detail. The 0/15/-15/30/-30/45/-45/60/-60/75/-75/90 sample has a higher SE at 400 MHz, but the SE is lower between 800 and 1500 MHz. This may be due to the some differences between fabricated sample and EM model of sample.

For high frequency measurements, we used an X-band (8.2-12.4 GHz) waveguide setup. The waveguide cross-section size is 22.86 × 10.16 mm^2. For example, the measured SE of a one-layer unidirectional carbon fiber (T300-12K) sample is reported in Figure 2.16. SE is measured for two different cases, with the fibers parallel to the electric field, and with the fibers perpendicular. It is observed that SE is about 40 dB lower for the case that electric field is perpendicular to fiber orientation.

2.5 Summary

In this chapter, the electromagnetic and shielding properties of RCCF composites were investigated. The equivalent inhomogeneous anisotropic model was efficiently used to

analyze the shielding characteristics of RCCF composites. The effect of orientation pattern and incident plane wave parameters on shielding effectiveness of multilayer RCCF composites was studied. It was shown, both numerically and experimentally, that using different orientation patterns in the multilayer composites controls the shielding properties of the structure. The effect of incident angle was different on the shielding of perpendicular ($E\perp$) and parallel ($E_{||}$) modes. Moreover, the effect of incident plane wave polarization angle was evaluated for two typical multilayer composites. It is observed that shielding effectiveness varies considerably at higher frequencies for different polarization angles.

Chapter 3 : Carbon Nanotube Composites

CNTs were discovered by Ijima in 1991 [60]. CNTs are made from rolled sheets of graphite. Generally there are three types of CNTs, namely zigzag, armchair, and chiral nanotubes [61]. CNTs are found in two categories, namely single wall carbon nanotubes (SWCNT) and multiwall carbon nanotubes (MWCNT). The diameter of CNTs is in the order of a few nanometers whereas the length could be in the order of few micrometers. Details about CNT types and models of materials are given in [62]. There are different techniques to produce CNTs such as arc discharge, laser ablation, high pressure carbon monoxide (HiPCO), and chemical vapor deposition (CVD) methods. The CVD method, known as catalyst method, is the most common technique to make cheaper CNTs in higher quantities [63]. The Young's modulus and tensile strength of a CNT are 1.2 TPa and 150 GPa, respectively, whereas the strength of steel is about 2GPa. The density of CNTs is around 1.4 g/cm^3, half that of aluminum and more than five times lower than copper. The thermal conductivity of CNT is about 3500-6000 W/m·K, more than ten times that of copper at 385 W/m·K. The electric current carrying capability is around 10^9 amp/cm^2, about one thousand times that of copper. CNTs are stable at high temperatures up to 2800 $^\circ$C in vacuum and 750 $^\circ$C in air.

Outstanding mechanical properties, high electrical conductivity and high aspect ratio (AR) make the CNTs one of the most promising filler materials for conductive polymer

composites [64]-[73][78]-[79][81][80]. AR is the ratio of length to diameter of nanotube. Compared to other kind of carbon composites such as carbon black (CB), CNT composites show higher conductivity with lower carbon percentage. For example, for composite with 0.35% CNT, one may need to use 20% CB composite to reach to the same level of conductivity [79]. The other advantages of CNT composites are the uniformity and isotropy. Due to the high AR and small size of CNTs which is about a few nanometers in diameter and few micrometers in length, the CNT composite maintain its uniformity and isotropy even for higher carbon concentration. The AR of the nanotubes is one of the main parameters that affect the percolation behavior and as a result, the conductivity of the nanocomposites [64],[69]-[71],[80][81]. Due to the low price and scalable production, MWCNTs are extensively used to produce conductive composites [64] with epoxy resins, one of the most widely used thermosets. The conductivity of the composite and its SE depend on the loading and characteristics of the MWCNTs, and also the properties of the conductive network formed by the MWCNTs all over the matrix [80][81]. In order to produce a conductive network, highly-entangled accumulations of MWCNTs should be distributed efficiently in the resin by shear mixing or by ultrasonic processing. Among the shear mixing techniques, three-roll milling [65]-[68] is one of the best methods as it is solvent free, scalable, uniformly shears the entire volume of the material, and can easily handle high nanotube loadings [80][81].

The majority of the studies on nanocomposites made of CNTs and thermoplastics [72]-[75] or thermosets [76]-[78] have reported the shielding effectiveness to be up to 60 dB over various frequency ranges, from low frequencies (130 MHz) up to the K-band where the maximum SE of 20 to 60 dB is achieved only at very high nanotube loadings

(15 to 50 *wt*%). However, high CNT loading (>10 *wt*%) is detrimental to the process and cost of the composite. Therefore, it is very demanding and desirable to make highly conductive composites with low CNT loading.

Recently in the CONCOM laboratory, highly conductive nanocomposites have been produced so that they are made of mass-produced MWCNTs at low loadings (<10 *wt*%) and epoxy resin [81]. Three-roll milling was used for MWCNTs dispersion. The high shielding performance of various samples over G-, X-, Ku- and K-band frequency range is investigated and compared with SE of other types of CNT samples reported in the literature. In addition to the conductivity, the thickness of the sample determines the SE as well. The effect of sample thickness on the SE of our nanocomposites is assessed and verified experimentally.

In what follows, we first briefly introduce the preparation process and DC conductivity properties of the proposed highly conductive composites. Then, the SE and effective conductivity results over the desired frequency range will be presented.

3.1 Sample Preparation and Percolation Curves

The samples were produced by CONCOM using the preparation method explained in [81]. MWCNTs synthesized by CVD were provided by Arkema (Graphistrength-C100), Bayer Material Science (Baytubes-C150P) and NanoLab (Industrial Grade CNTs–NLIG). Their main characteristics are presented in Table 3.1.

Table 3.1: Characteristics of the MWCNTs given by the manufacturer [81]

Acronym	Lot no.	Outer Diam. (D)., nm	Length (L), μm
C100	7127	10-15	0.1-10
C150P	103	13-16	1->10
NLIG	43008	10-30	5-20

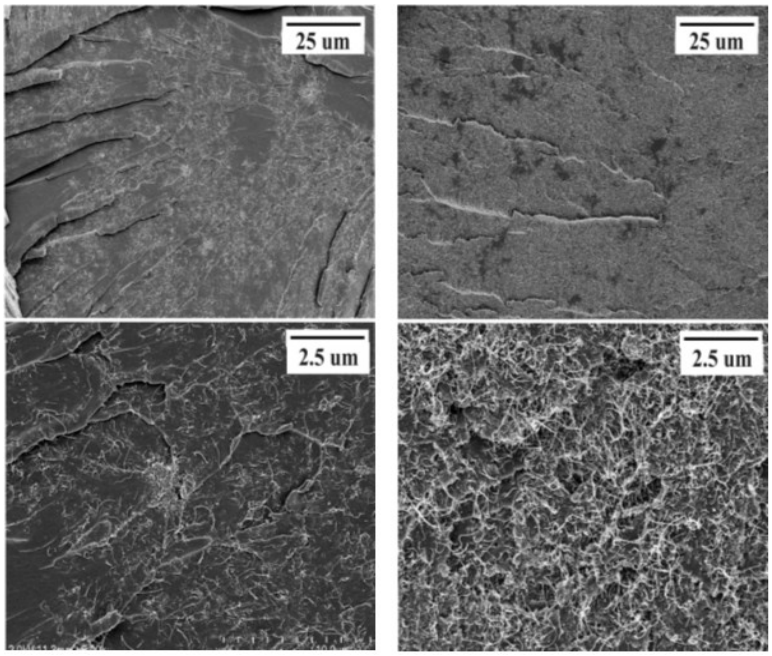

(a) (b)

Figure 3.1. SEM micrographs of NLIG composites (a) 1 *wt*% loading, (b) 8 *wt*% loading [80].

3.1.1 Composite Preparation

The composite preparation details were given by Dr. Rosca from CONCOM as follows [81]:

The resin, the curing agent (26.4 wt%) and the MWCNTs were weighed and hand mixed to form batches of 12 g. As the reactivity of the curing agent is very low at room temperature, we added the curing agent from the beginning in order to reduce the mixture viscosity, especially for high nanotube loadings. The batch was three-roll-milled for several times on a laboratory scale mill (EXAKT 80E, EXAKT Technologies, Inc.) at different shearing intensities. Next, the mixture was degassed in a vacuum oven at 90 °C for 30 min and loaded between two aluminum plates coated with demolding agent and

separated by a PTFE spacer of 1.6 mm thickness. Finally, the plates were tightened together by bolt joints, and the composite was cured at 120 °C for 6 hours. After demolding, the composite was trimmed to form 50 × 50 × 1.6 mm^2 plates. Batches with nanotube loading lower then 0.5 wt% were prepared by dilution of the 0.5 wt% mixture. The SEM micrographs of Figure 3.1 shows that three-roll milling is a very suitable method for homogeneously dispersing MWCNTs over a wide range of loadings.

3.1.2 DC Conductivity Measurements

The van-der-Pauw method is used to measure the conductivity of MWCNT composites [82] [83]. According to the percolation theory [84] the conductivity of composite can be expressed as

$$\sigma = \sigma_0 \left(p - p_c \right)^t \tag{3.1}$$

where p is nanotube weight fraction, p_c is percolation threshold, t is critical exponent and σ_0 is the conductivity of an element of the percolating network. Figure 3.2 and Table 3.2 present the percolation curves and the percolation parameters respectively for our MWCNT samples.

Figure 3.2 shows that AR has a significant effect on the conductivity of a composite. Having the aspect ratio 5.5 times greater, the NLIG composite shows a conductivity about 10 times higher than the C150P composite. The maximum conductivity of 239.1 S/m obtained for NLIG at 8 *wt*% is one of the highest values reported for epoxy-MWCNT composites at similar loading.

Table 3.2: Percolation parameters of the MWCNT samples [81]

MWCNT	p_c , *wt*%	*t*	σ_0 , S/m
NLIG	0.012	1.77	23075
C100	0.097	1.86	5724
C150P	0.188	1.96	3981

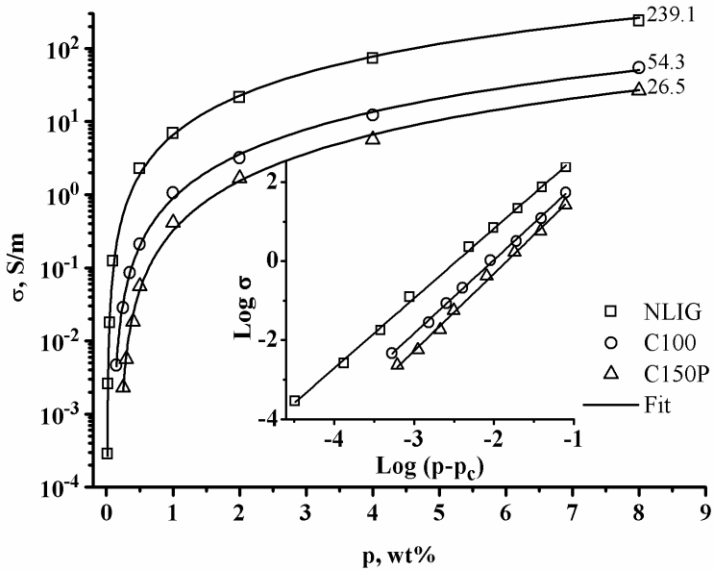

Figure 3.2. Percolation curves of the considered MWCNTs, giving the DC conductivity as a function for the CNT loading [81].

3.2 Shielding Effectiveness of MWCNT Composites

The shielding effectiveness of our nanocomposites was experimentally investigated over a wide frequency range, up to 26.5 GHz, using rectangular waveguides. As shown in Figure 3.3, we have used G-, X-, Ku- and K-band rectangular waveguides with dimensions of 47.548 × 22.148 mm, 22.86 × 10.16 mm, 15.8 × 7.9 mm and 10.668 × 4.318 mm, respectively. Using an Agilent-E8364B network analyzer, which can operate from 10 MHz to 50 GHz, the measured SE of NLIG samples with different MWCNT

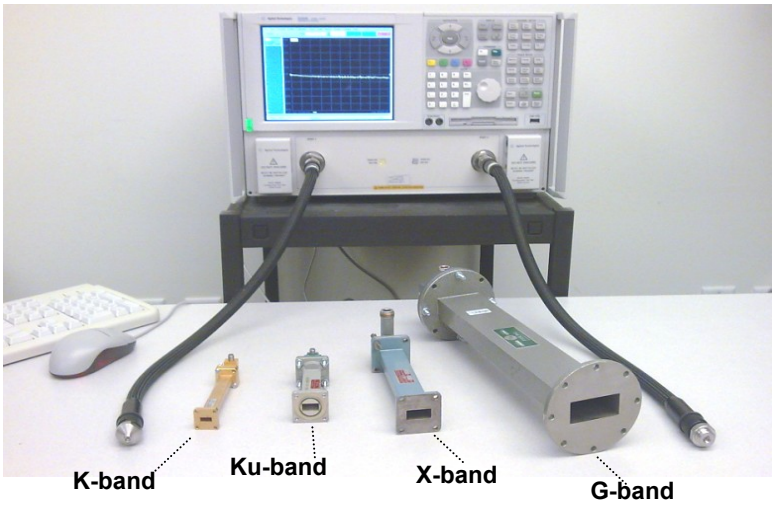

Figure 3.3. G-, X-, Ku- and K-band waveguides with cables and the network analyzer.

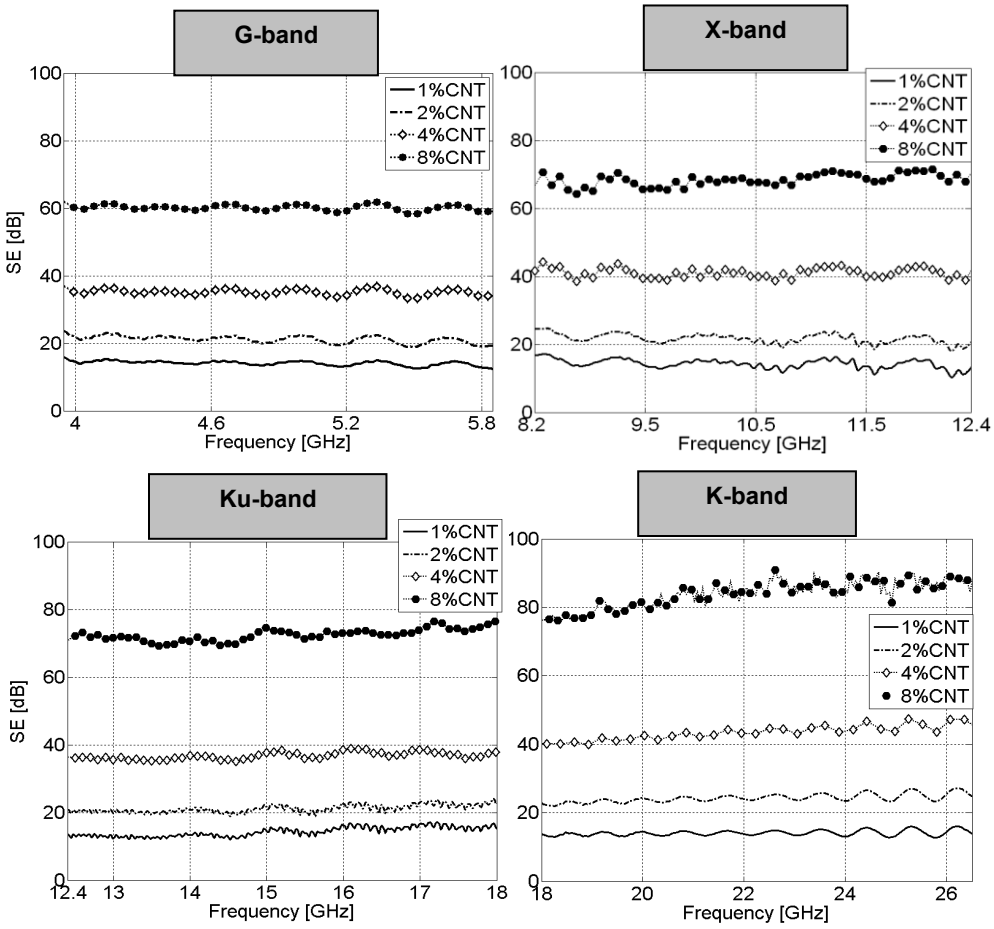

Figure 3.4. Measured SE of NLIG samples over G-, X-, Ku- and K-band frequency ranges.

Table 3.3: Specifications of Tested NLIG Samples

MWCNT (% *wt*)	Volume fraction (% *vf*)	Thickness (mm)
1	0.602	1.65
2	1.210	1.67
4	2.439	1.8
8	4.959	1.9

loading is presented in Figure 3.4. The sample specifications are given in Table 3.3. The SE increases from less than 20 dB from 1 %*wt* to 20 to 25 dB for 2 %*wt*, 35 to 45 dB for 4 %*wt* to 60 to 90 dB for 8 %*wt*. The SE is roughly constant with frequency at G and X band, and increases with frequency at higher frequencies and higher CNT loadings, especially at K band up to 26.5 GHz. This increasing can be explained by considering the skin depth of the composite, which will be addressed in next section.

In Figure 3.5 we have compared the shielding properties of our samples containing 4 and 8 %*wt* NLIG with similar composites reported in the literature. It is observed that our nanocomposites based on NLIG with lower nanotube loading and smaller thickness have a much higher SE than those reported in [55], [74]-[76]. It should be noted that the MWCNT samples reported in [55] are characterized over an 8-10 GHz frequency range so that the corresponding shielding performance in Figure 3.5 is calculated only over that frequency band.

Figure 3.6 presents the SE of nanocomposites made of MWCNTs with different aspect ratios (Table 3.1). The DC conductivity in Figure 3.2 is strongly dependent on the aspect ratio. Figure 3.6 shows that the SE is much higher using nanotubes with a high aspect ratio. Thus the SE with NLIG is 60 to 90 dB over the 4 to 26 GHz frequency range, much larger than C100 which has an SE of 30 to 40 dB.

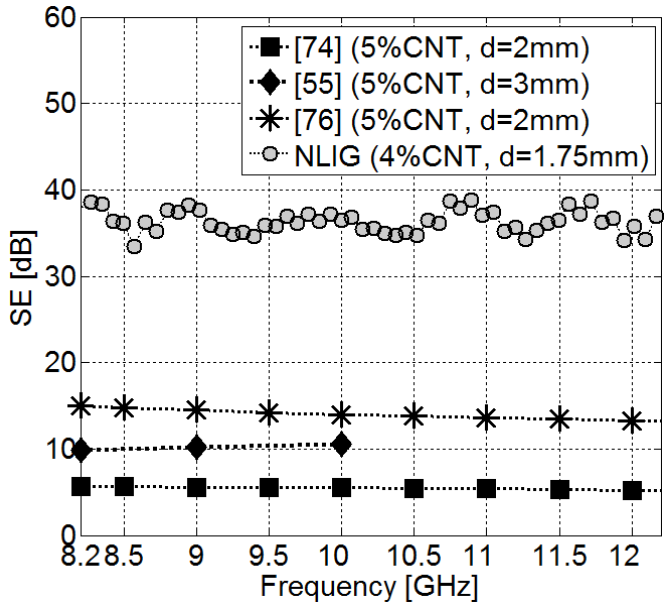

(a)

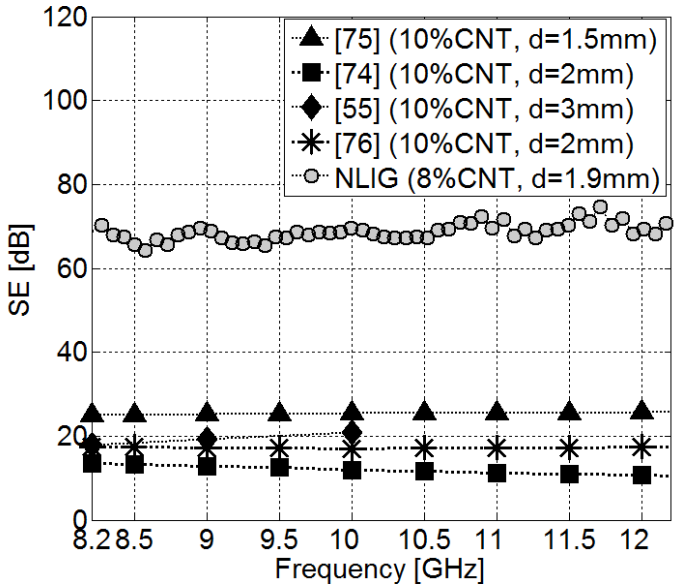

(b)

Figure 3.5. Comparison of NLIG shielding performance with other samples from the literature: (a) 4%wt and (b) 8%wt MWCNT NLIG.

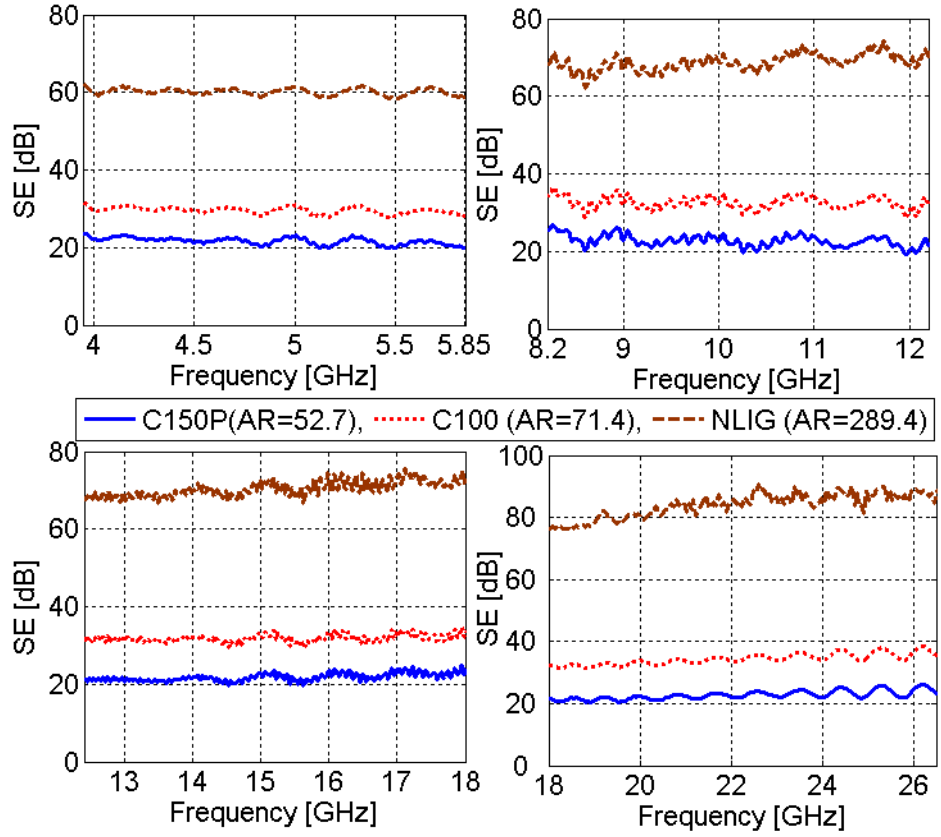

Figure 3.6. The effect of aspect ratio on the SE of proposed nanocomposites.

3.3 Effective Conductivity of NLIG-MWCNT Samples and Simulation Results

In Section 3.1, D.C. conductivity (σ_{DC}) of the nanocomposites was reported along with the percolation curves (Figure 3.2). However, since composite materials may show noticeably frequency-dependent behavior, it is important to characterize the effective parameters (conductivity, permittivity and permeability) of samples over a wide frequency range. In this section, we obtain the effective conductivity (σ_{eff}) of the nanocomposites by minimizing the difference between the measured scattering

parameters and simulations provided by CST MWS. The effective conductivity is also obtained by using analytical method and the results are compared with CST MWS results. Furthermore, for design purposes, the SE/thickness diagrams of 1%, 2%, 4% and 8%*wt* MWCNT NLIG samples are provided for the whole frequency range of interest by using the effective parameters of sample. The results are also verified experimentally.

3.3.1 Effective Conductivity

The scattering parameters of the slab of composite material in the waveguide could be determined by mode matching [85]. The slab is assumed to be homogeneous effective parameters (ε_{reff}, μ_{reff}), where the complex permittivity is used to include the effect of loss. Our composite materials are non-magnetic so the permeability is that of free space [55] [42][86]. The dominant mode inside the waveguide and slab is TE_{10} mode. Evanescent modes exist in the waveguide both inside the slab and in the air near the surfaces of the slab, and store energy. Based only on the dominant mode, the scattering parameters of the slab in the waveguide are

$$S_{11} = 20\log\left(\frac{E_R}{E_i}\right) \tag{3.2}$$

$$S_{21} = 20\log\left(\frac{E_T}{E_i}\right) \tag{3.3}$$

where

$$\frac{E_R}{E_i} = \frac{r_1 + r_2 e^{-j2\beta_{TE10}d}}{1 + r_1 r_2 e^{-j2\beta_{TE10}d}} \tag{3.4}$$

and

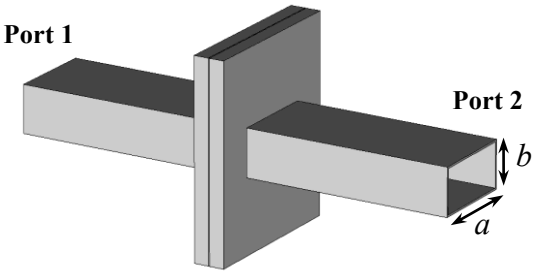

Figure 3.7. The electromagnetic model of waveguide setup developed in CST MWS.

$$\frac{E_T}{E_i} = \frac{t_1 t_2 e^{-j\beta_{TE10} d}}{1 + t_1 t_2 e^{-j2\beta_{TE10} d}} \tag{3.5}$$

where E_i, E_R, and E_T are incident, reflected and transmitted electric fields in the waveguide, respectively. Parameter d is the thickness of the slab. The other parameters are

$$r_1 = \frac{\sqrt{\mu_{reff} / \varepsilon_{reff}} - 1}{\sqrt{\mu_{reff} / \varepsilon_{reff}} + 1} \tag{3.6}$$

$$r_2 = -r_1 \tag{3.7}$$

$$\beta_{TE10} = \sqrt{\omega^2 \mu_0 \mu_{reff} \varepsilon_0 \varepsilon_{reff} - (\pi / a)^2} \tag{3.8}$$

and

$$t_1 = \frac{2\sqrt{\mu_{reff} / \varepsilon_{reff}}}{\sqrt{\mu_{reff} / \varepsilon_{reff}} + 1} \tag{3.9}$$

$$t_2 = \frac{2}{\sqrt{\mu_{reff} / \varepsilon_{reff}} + 1} \tag{3.10}$$

and $\omega = 2\pi f$ and a is the width of the waveguide. The accuracy of the model could be improved by accounting for higher-order modes, which are cutoff but which store energy.

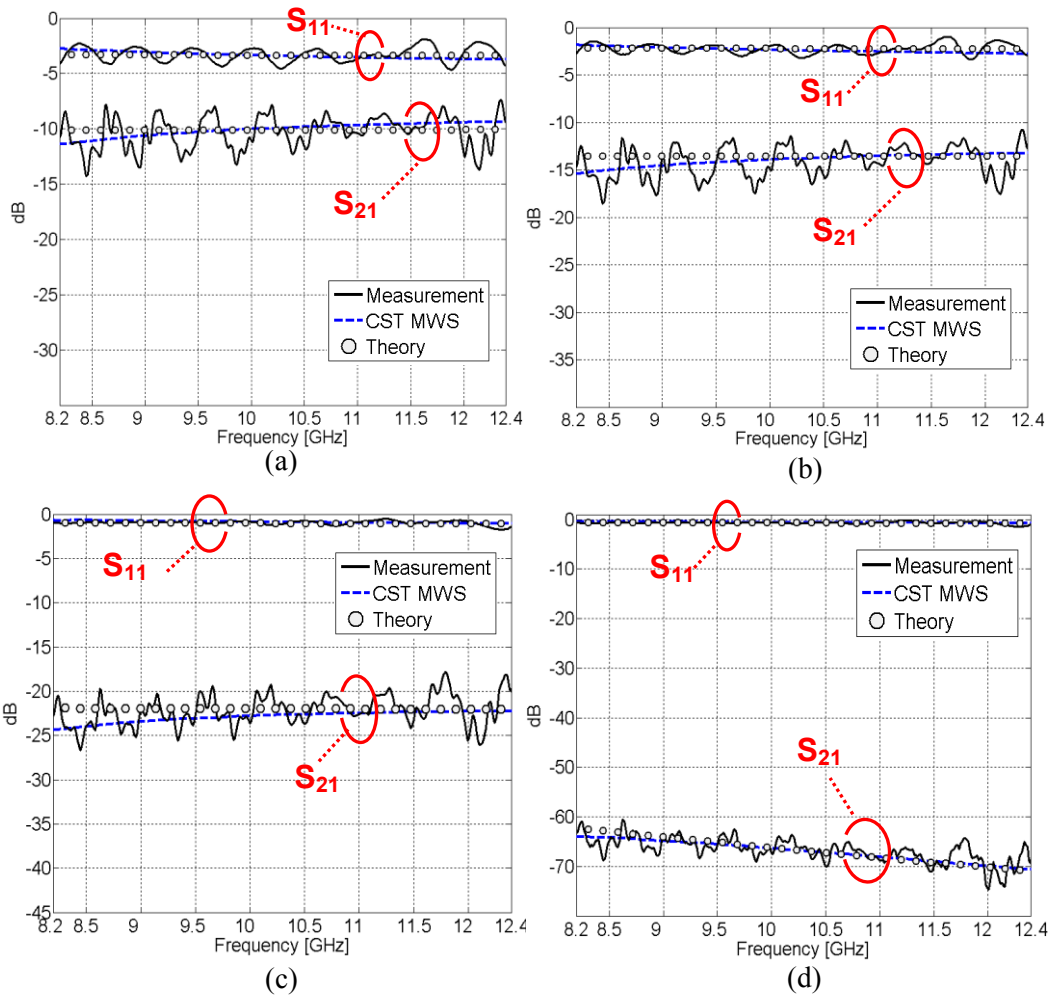

Figure 3.8. The magnitude of scattering parameters of the proposed MWCNT nanocomposites, (a) 1%*wt*, $d = 0.9$ mm. (b) 2%*wt*, $d = 0.9$ mm, (c) 4%*wt*, $d = 0.5$ mm and (d) 8%*wt*, $d = 2$ mm.

Figure 3.7 shows a realistic model of the waveguide measurement setup for analysis with CST MWS software. CST MWS is based on the finite integration technique (FIT) [87]-[89], which discretizes the integral form of Maxwell equations, and so inherently accounts for the energy-storage effects of cutoff waveguide modes in the slab and near the surfaces of the slab, and so is expected to be more accurate than the dominant-mode analysis presented above.

Table 3.4: Effective Conductivity of NLIG Samples versus MWCNT Concentration

Simulation Setup	MWCNT (% *wt*)			
	1	**2**	**4**	**8**
CST MWS	10 S/m	20 S/m	110 S/m	215 S/m
Analytical Model	13 S/m	22 S/m	118 S/m	228 S/m
DC Measurement	6.9 S/m	21.5 S/m	73.6 S/m	239.1 S/m

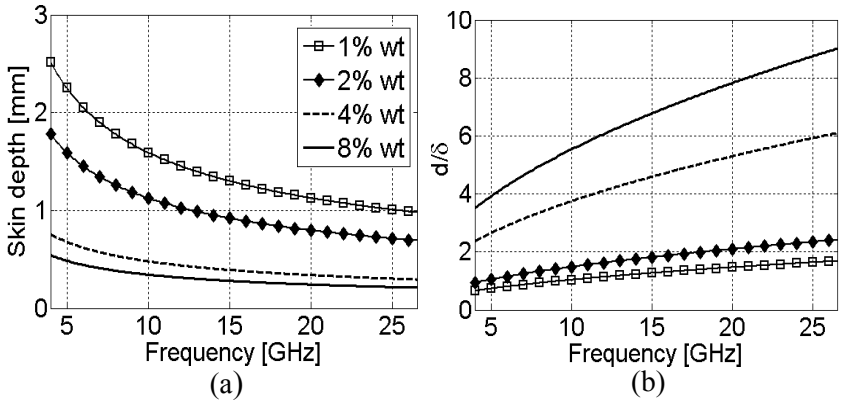

Figure 3.9. (a) Skin depth of NLIG samples given in Table 3.3 versus frequency, (b) Thickness to skin depth ratio of NLIG samples.

In order to find the effective conductivity of the slab, we try to minimize the difference between measured and simulated S_{11} and S_{21} scattering parameters, for various complex permittivity values so that the conductivity can be extracted from the imaginary part of the complex permittivity. We match the mean value of the simulated scattering parameters to the mean value of the measured parameters over the desired frequency range, and choose the complex permittivity that makes the mean values closest. For conciseness, only the X-band results are shown in Figure 3.8.

Table 3.4 shows the conductivity for samples with 1%, 2%, 4% and 8% MWCNT, from both the CST MWS model and analytical model of (3.2) to (3.10). The conductivity

values obtained by the two models are comparable, but differ somewhat. The more accurate values are those obtained by the MWS model, which inherently accounts for higher-order modes in the slab and near the surfaces of the slab.

Table 3.4 shows the measured DC conductivity σ_{DC} of the samples. The values for 2% and 8% loading are comparable to the effective values determined from the MWS model, but the values for 1% and 4% loading are considerably different. By changing MWCNT loading from 1% to 8%, the effective relative permittivity of samples varies from 4 to 15, respectively. Due to the skin depth phenomenon, since for highly conductive materials the conductivity of material has major contribution in SE rather than relative permittivity, here we just discuss the conductivity of samples. Figure 3.9(a) shows the skin depth, $\delta = 1/\sqrt{\pi f \mu_0 \sigma}$, of the NLIG samples versus nanotube loading. Figure 3.9(b) shows the ratio of sample thickness to skin depth (d/δ) for NLIG samples given in Table 3.3. It is observed that for NLIG with 8%wt loading, the d/δ ratio increases significantly with frequency. This explains why the SE in Figure 3.4 increases with frequency between 18 and 26 GHz where d gets greater than about 8δ. In fact, as the frequency increases, the skin depth decreases and the SE increases, even if the conductivity is constant.

3.3.2 Effect of Sample Thickness on Shielding Properties

For design purposes, we may need to control the shielding level by considering the cost limitations. It was observed that the level of SE could be controlled by using different MWCNT loadings. One of the important factors which can be used to adjust the level of SE is sample thickness. Therefore, providing the SE/thickness table for any kind of composite sample can be efficiently used for design purposes in different applications.

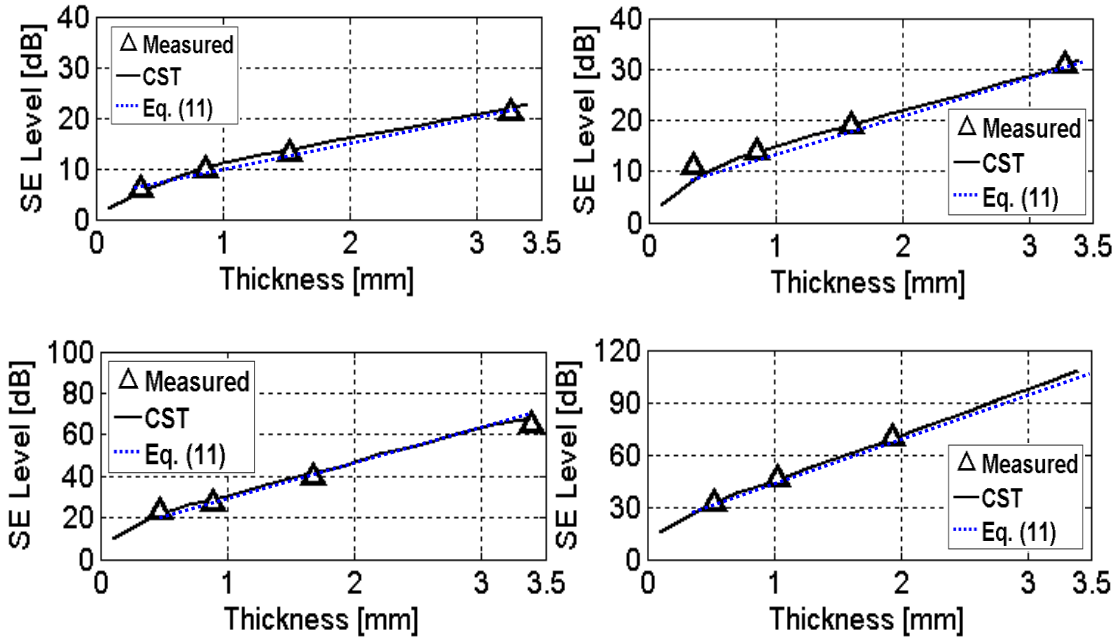

Figure 3.10. The SE of NLIG sample versus sample thickness over X-band frequency range.

Table 3.5: SE / Thickness of NLIG Samples with Different MWCNT Concentrations

MWCNT	X-band	Ku-band	K-band
1 %	4.7 ± 0.4 dB/mm	5.1 ± 1 dB/mm	4.6 ± 0.6 dB/mm
2 %	6.8 ± 0.4 dB/mm	7.3 ± 2 dB/mm	8.7 ± 1.3 dB/mm
4 %	14 ± 1.5 dB/mm	16 ± 1.7 dB/mm	16.8 ± 1.7 dB/mm
8 %	26 ± 0.5 dB/mm	32 ± 2 dB/mm	34 ± 4 dB/mm

For a slab of conductive material where the skin depth is much less than the slab thickness, SE can be estimated by ignoring interactions between the surfaces as follows [90]:

$$SE = 20\log\left|\frac{(\eta_0+\eta_s)^2}{4\eta_0\eta_s}\right| + 8.686\left(\frac{d}{\delta}\right) \tag{3.11}$$

where η_s and η_0 are the intrinsic impedances for the TE_{10} mode for the slab and for air, respectively. Equation (3.11) shows that the SE increases linearly with thickness d for highly-conductive composite samples.

Using the waveguide simulation setup (developed in MWS) and using the characterized effective parameters of the previous section, we have investigated the effect of the sample thickness on SE of NLIG samples over the considered frequency range. Figure 3.10 shows the simulated SE vs. thickness curves over the X-band frequency range. By fabricating samples with different thicknesses, the experimental results (points on Figure 3.10) are in good agreement with those of the simulations and (3.11). The SE of the composites shows a nearly linear dependence on the sample thickness with the slope given by (3.11). The slope representing the SE per unit thickness of the composite with different NLIG loadings over the X-, Ku- and K bands is presented in Table 3.5. We also provide a margin for SE level which is obtained from minimum and maximum variation of SE versus sample thickness over the desired frequency range. The results were also verified experimentally which is not shown here.

3.4 Summary

In this chapter, the electromagnetic and shielding properties of CNT composites were investigated. Three roll milling was successfully used to form highly conductive homogeneous MWCNT-epoxy dispersions with nanotube loading up to 8 *wt*%. The shielding performance of the proposed highly conductive MWCNT composites was investigated over a wide frequency range up to 26.5 GHz. In addition to non frequency dependant behavior, the SE level can reach to 90 dB over a part of K-band and more than 60 dB over G-, X- and Ku-band frequency ranges by loading sample with only 8%*wt* MWCNT. The proposed nanocomposites show an outstanding shielding improvement compared to the other type of CNT composites introduced in literature so far. The effect

of aspect ratio was also investigated. It was found that higher aspect ratio results in lower percolation threshold and higher conductivity. As the MWCNT aspect ratio increases 5.5 times, the SE of the corresponding composites increases by more than 40 dB. The effective conductivity of the proposed nanocomposites was calculated by fitting the mean of simulated and measured scattering parameters of waveguide setups. Showing very high shielding effectiveness for low MWCNT loading (<10%), nanocomposite made of long MWCNTs and epoxy resin is a good candidate for aerospace and aircraft industry.

Chapter 4 : Green's Function of a Dielectric Slab Grounded by CFC Materials

The fuselage of many modern aircraft is made of composite material. Since the fuselage can be used as the ground plane for the antennas installed on it, investigating the performance of such antennas operating on a composite ground is an issue to be addressed. Moreover, composites are increasingly used in antenna and microwave circuits, such as full composite antennas discussed in the previous chapters. There have been very few published works on EM characterization of specific composite circuits [91]. From the EMC point of view, the crosstalk between transmission lines and the coupling between printed composite antennas on the substrate is another issue which needs to be addressed. Hence, evaluating the Green's function of a dielectric slab with a composite ground plane when both source and observation points located at the air-dielectric interface becomes imperative. Many papers investigate the Green's function of a dielectric slab backed by a perfect electric conductor (PEC) as a ground plane [92]-[100]. In [100], an imperfectly-conducting ground plane is considered, but the small ohmic loss approximation (conductivity > 10^6 S/m) is used for EM field calculation, showing that the fields at the air-dielectric interface do not depend on the conductivity of ground plane. However, the ohmic loss of CFCs, with a conductivity of about 10^4 S/m, is

much higher than copper or other kinds of metals. Furthermore, in addition to the high loss, RCCF is also an anisotropic material, making the solution completely different than that for an isotropic ground plane.

In this Chapter, using the spectral domain method, we calculate the exact solution for the Green's function of a dielectric slab backed by a CFC ground plane and excited by a horizontal electric dipole (HED). The assumed CFCs are efficiently modeled by the corresponding surface impedance sheets; a lossy anisotropic sheet for RCCF and a lossy isotropic sheet for CNT. The expression for the electric field is obtained and the numerical integration is addressed in detail. Finally, some numerical results are presented and compared to that of the slab with a PEC ground plane.

4.1 HED on Dielectric Slab Grounded by RCCF Composite

Figure 4.1 shows an *x*-directed horizontal electric dipole (HED) on a dielectric slab of infinite extent in the transverse direction, backed by an RCCF sheet. Because of its high conductivity, the RCCF sheet can be modeled by an anisotropic impedance surface $\left(Z_x, Z_y\right)$ as follows

$$Z_i = (1+j)\sqrt{\left(\frac{\omega\mu_0}{2\sigma_i}\right)} \qquad i = x, y \tag{4.1}$$

where $\omega = 2\pi f$ and $\mu_0 = 4\pi \times 10^{-7}$. We will find the solution for an anisotropic ground plane, and for the isotropic case, we can set $Z_x = Z_y = Z$. Without loss of generality, the electric source current distribution can be as assumed to be polarized along *x*. Figure 4.1 shows that we divide the solution into region I for the dielectric layer and region II for the

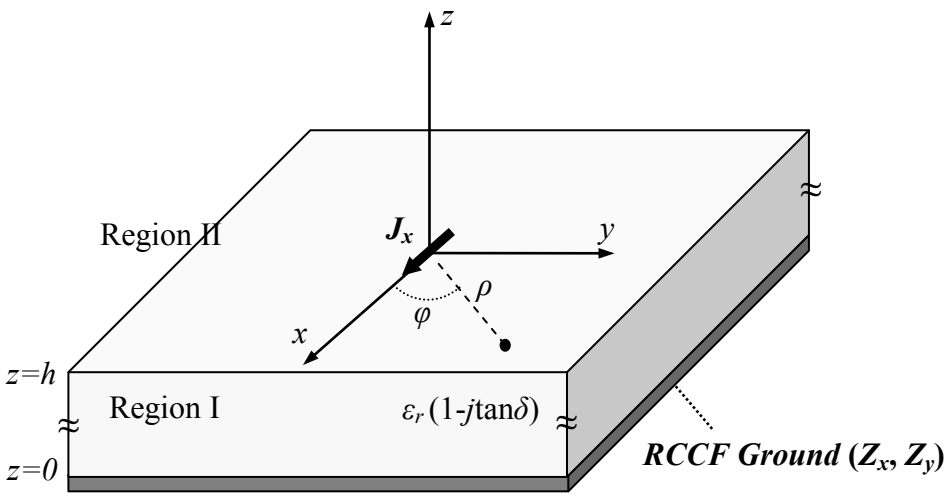

Figure 4.1. HED located on the slab grounded by RCCF composite material.

air above it. Then the source-free Maxwell equations are solved to calculate the *z*-components of EM fields in each region.

From the Maxwell equations, the wave equation in each region is expressed as

$$\nabla^2 \boldsymbol{E} + k^2 \boldsymbol{E} = 0 \tag{4.2}$$

$$\nabla^2 \boldsymbol{H} + k^2 \boldsymbol{H} = 0 \tag{4.3}$$

where

$$k = \begin{cases} k_0 = \omega\sqrt{\mu_0\varepsilon_0} & \text{Region II}\,(z > h) \\ k_e = \omega\sqrt{\mu_0\varepsilon_0\varepsilon_r} & \text{Region I}\ (0 < z < h) \end{cases} \tag{4.4}$$

By defining the two-dimensional Fourier transform as

$$\tilde{\boldsymbol{E}}\left(k_x, k_y, z\right) = \int_{-\infty}^{+\infty}\int_{-\infty}^{+\infty} \boldsymbol{E}\left(x, y, z\right) e^{-jk_x x} e^{-jk_y y}\, dxdy, \tag{4.5}$$

the solution in the spectral domain for the *z*-component of the EM field in each region can be obtained as

$$\tilde{E}_{z2} = Ae^{-jk_2(z-h)} \qquad \mathrm{Im}(k_2) < 0 \tag{4.6}$$

$$\tilde{H}_{z2} = Be^{-jk_2(z-h)} \qquad \mathrm{Im}(k_2) < 0 \tag{4.7}$$

$$\tilde{E}_{z1} = C\cos k_1(z-h) + D\sin k_1(z-h) \tag{4.8}$$

$$\tilde{H}_{z1} = E\cos k_1(z-h) + F\sin k_1(z-h) \tag{4.9}$$

where

$$k_2^2 = k_0^2 - \beta^2 \tag{4.10}$$

$$k_1^2 = k_e^2 - \beta^2 \tag{4.11}$$

$$\beta^2 = k_x^2 + k_y^2. \tag{4.12}$$

where A, B, …, F are unknown coefficients. The other components of fields are obtained from the Maxwell's equations using

$$\tilde{E}_x = \left(\frac{jk_x}{\beta^2}\right)\frac{\partial \tilde{E}_z}{\partial z} + \left(\frac{\omega\mu_0 k_y}{\beta^2}\right)\tilde{H}_z \tag{4.13}$$

$$\tilde{E}_y = \left(\frac{jk_y}{\beta^2}\right)\frac{\partial \tilde{E}_z}{\partial z} - \left(\frac{\omega\mu_0 k_x}{\beta^2}\right)\tilde{H}_z \tag{4.14}$$

$$\tilde{H}_x = \left(\frac{jk_x}{\beta^2}\right)\frac{\partial \tilde{H}_z}{\partial z} - \left(\frac{\omega\varepsilon k_y}{\beta^2}\right)\tilde{E}_z \tag{4.15}$$

$$\tilde{H}_y = \left(\frac{jk_y}{\beta^2}\right)\frac{\partial \tilde{H}_z}{\partial z} + \left(\frac{\omega\varepsilon k_x}{\beta^2}\right)\tilde{E}_z. \tag{4.16}$$

Then, the unknown coefficients are calculated by imposing the following boundary conditions

$$E_{x1} = E_{x2} \qquad \text{at} \quad z = h \tag{4.17}$$

$$E_{y1} = E_{y2} \qquad \text{at} \quad z = h \tag{4.18}$$

$$H_{x1} = H_{x2} \qquad \text{at} \quad z = h \tag{4.19}$$

$$H_{y1} - H_{y2} = \tilde{J}_x \qquad \text{at} \quad z = h \tag{4.20}$$

$$E_{x1} = -Z_x H_{y1} \qquad \text{at} \quad z = 0 \tag{4.21}$$

$$E_{y1} = Z_y H_{x1} \qquad \text{at} \quad z = 0. \tag{4.22}$$

After a considerable algebraic procedure, the coefficients inside the slab are found to be

$$\begin{aligned} C = & \left(\frac{-\beta^2 \tilde{J}_x}{\Delta} \right) \times \\ & \Big[-\left(\omega^2 \mu_0^2 k_x k_1 k_2 \beta^4 \cos k_1 h \right) T_3 + \left(Z_x k_x^2 + Z_y k_y^2 \right) \left(-j\omega^3 \mu_0^2 \varepsilon_0 \varepsilon_r k_x k_2 \beta^2 \sin k_1 h \right) T_3 \\ & - \left(Z_x k_y^2 + Z_y k_x^2 \right) \left(-j\omega \mu_0 k_x k_1^2 k_2 \beta^2 \cos k_1 h \right) T_4 \\ & - Z_x Z_y \left(\omega^2 \mu_0 \varepsilon_0 \varepsilon_r k_x k_1 k_2 \beta^4 \sin k_1 h \right) T_4 + \left(Z_x - Z_y \right) \left(\omega^3 \mu_0^2 \varepsilon_0 k_x k_y^2 k_1^2 \beta^2 \right) \Big] \end{aligned} \tag{4.23}$$

$$\begin{aligned} D = & \left(\frac{\beta^2 \tilde{J}_x}{\Delta} \right) \times \\ & \Big[-\left(\omega^2 \mu_0^2 k_x k_1 k_2 \beta^4 \sin k_1 h \right) T_3 + \left(Z_x k_x^2 + Z_y k_y^2 \right) \left(j\omega^3 \mu_0^2 \varepsilon_0 \varepsilon_r k_x k_2 \beta^2 \cos k_1 h \right) T_3 \\ & - \left(Z_x k_y^2 + Z_y k_x^2 \right) \left(j\omega \mu_0 k_x k_1^2 k_2 \beta^2 \sin k_1 h \right) T_4 \\ & + Z_x Z_y \left(\omega^2 \mu_0 \varepsilon_0 \varepsilon_r k_x k_1 k_2 \beta^4 \cos k_1 h \right) T_4 + \left(Z_x - Z_y \right) \left(j\omega^3 \mu_0^2 \varepsilon_0 \varepsilon_r k_x k_y^2 k_1 k_2 \beta^2 \right) \Big] \end{aligned} \tag{4.24}$$

$$\begin{aligned} E = & \left(\frac{-\beta^2 \tilde{J}_x}{\Delta} \right) \times \\ & \Big[-\left(\omega^3 \mu_0^2 \varepsilon_0 k_y k_1 \beta^4 \cos k_1 h \right) T_2 + \left(Z_x k_x^2 + Z_y k_y^2 \right) \left(j\omega^4 \mu_0^2 \varepsilon_0^2 \varepsilon_r k_y \beta^2 \cos k_1 h \right) T_1 \\ & - \left(Z_x k_y^2 + Z_y k_x^2 \right) \left(j\omega^2 \mu_0 \varepsilon_0 k_y k_1^2 \beta^2 \sin k_1 h \right) T_2 \\ & - Z_x Z_y \left(\omega^3 \mu_0 \varepsilon_0^2 \varepsilon_r k_y k_1 \beta^4 \sin k_1 h \right) T_1 - \left(Z_x - Z_y \right) \left(j\omega^2 \mu_0 \varepsilon_0 \varepsilon_r k_1 k_2^2 k_x^2 k_y \beta^2 \right) \Big] \end{aligned} \tag{4.25}$$

and

$$F = \left(\frac{\beta^2 \tilde{J}_x}{\Delta} \right) \times$$
$$\left[\left(\omega^3 \mu_0^2 \varepsilon_0 k_y k_1 \beta^4 \sin k_1 h \right) T_2 + \left(Z_x k_x^2 + Z_y k_y^2 \right) \left(j\omega^4 \mu_0^2 \varepsilon_0^2 \varepsilon_r k_y \beta^2 \sin k_1 h \right) T_1 \right.$$
$$- \left(Z_x k_y^2 + Z_y k_x^2 \right) \left(j\omega^2 \mu_0 \varepsilon_0 k_y k_1^2 \beta^2 \cos k_1 h \right) T_2$$
$$\left. - Z_x Z_y \left(\omega^3 \mu_0 \varepsilon_0^2 \varepsilon_r k_y k_1 \beta^4 \cos k_1 h \right) T_1 - \left(Z_x - Z_y \right) \left(\omega^2 \mu_0 \varepsilon_0 \varepsilon_r k_1^2 k_2 k_x^2 k_y \beta^2 \right) \right] \tag{4.26}$$

where

$$\Delta = \left(\beta^6 \omega^2 \mu_0 \varepsilon_0 \right) . \left[\left(j\omega\mu_0 T_3 + Z_x k_1 T_4 \right) \left(k_1 T_2 - Z_y j\omega\varepsilon_0 \varepsilon_r T_1 \right) + k_x^2 T_2 T_4 \left(Z_x - Z_y \right) \right] \tag{4.27}$$

$$T_1 = k_1 \cos k_1 h + j\varepsilon_r k_2 \sin k_1 h \tag{4.28}$$

$$T_2 = k_1 \sin k_1 h - j\varepsilon_r k_2 \cos k_1 h \tag{4.29}$$

$$T_3 = k_1 \cos k_1 h + jk_2 \sin k_1 h \tag{4.30}$$

$$T_4 = -k_1 \sin k_1 h + jk_2 \cos k_1 h. \tag{4.31}$$

Not shown here, the coefficients A and B can be easily calculated from (4.17) and (4.18). The effect of ground plane anisotropy is represented by terms including $Z_x - Z_y$ in (4.23)-(4.27). Since we are interested in electric fields at the air-dielectric interface, $\tilde{E}_x$ and $\tilde{E}_y$ at $z = h$ are obtained from (4.13) and (4.14) as

$$\tilde{E}_x \,|_{z=h} = \left(\frac{jk_x k_1}{\beta^2} \right) D + \left(\frac{\omega\mu_0 k_y}{\beta^2} \right) F \tag{4.32}$$

$$\tilde{E}_y \,|_{z=h} = \left(\frac{jk_y k_1}{\beta^2} \right) D - \left(\frac{\omega\mu_0 k_x}{\beta^2} \right) F. \tag{4.33}$$

Note that by setting $Z_x = Z_y = 0$ in (4.32) and (4.33), $\tilde{E}_x$ and $\tilde{E}_y$ become the coefficients for a PEC ground plane, as reported in the literature [85][96]

$$\tilde{E}_x\,|_{z=h} = \left(\frac{-j}{\omega\varepsilon_0}\right)\left[\frac{-jk_x^2 k_1 k_2}{\beta^2 T_2}\sin k_1 h + \frac{k_y^2 k_0^2}{\beta^2 T_3}\sin k_1 h\right]\tilde{J}_x \tag{4.34}$$

$$\tilde{E}_y\,|_{z=h} = \left(\frac{-j}{\omega\varepsilon_0}\right)\left[\frac{-jk_y^2 k_1 k_2}{\beta^2 T_2}\sin k_1 h + \frac{k_x^2 k_0^2}{\beta^2 T_3}\sin k_1 h\right]\tilde{J}_x. \tag{4.35}$$

By taking the inverse Fourier transform from (4.32) and (4.33), the spatial domain electric field can be obtained as

$$E_i(x,y) = \left(\frac{1}{4\pi^2}\right)\int_{-\infty}^{+\infty}\int_{-\infty}^{+\infty}\tilde{E}_i(k_x,k_y)e^{jk_x x}e^{jk_y y}dk_x dk_y \qquad i = x, y. \tag{4.36}$$

4.2 Electric Field Calculation

Without loss of generality, only E_x is considered for study. By applying the transformation of variables $k_x = \beta\cos\alpha$ and $k_y = \beta\sin\alpha$, (4.36) is converted to

$$E_x(x,y) = \left(\frac{1}{4\pi^2}\right)\int_0^{+\infty}\int_0^{2\pi}\tilde{E}_x(\beta,\alpha)e^{jx\beta\cos\alpha}e^{jy\beta\sin\alpha}\beta d\alpha d\beta \tag{4.37}$$

so that by numerical integration with respect to α, the electric field can be obtained from a single infinite integration as follows

$$E_x(x,y) = \left(\frac{1}{4\pi^2}\right)\int_0^{+\infty}\tilde{F}_x(\beta,x,y)d\beta. \tag{4.38}$$

The zeros of Δ given by (4.27) determine the poles of $\tilde{F}_x$, or the surface wave poles (SWP) of the structure. For the slab grounded by a PEC, when the slab is electrically thin, $f < c_0/4h\sqrt{\varepsilon_r - 1}$, there is only one SWP between k_0 and k_e located at

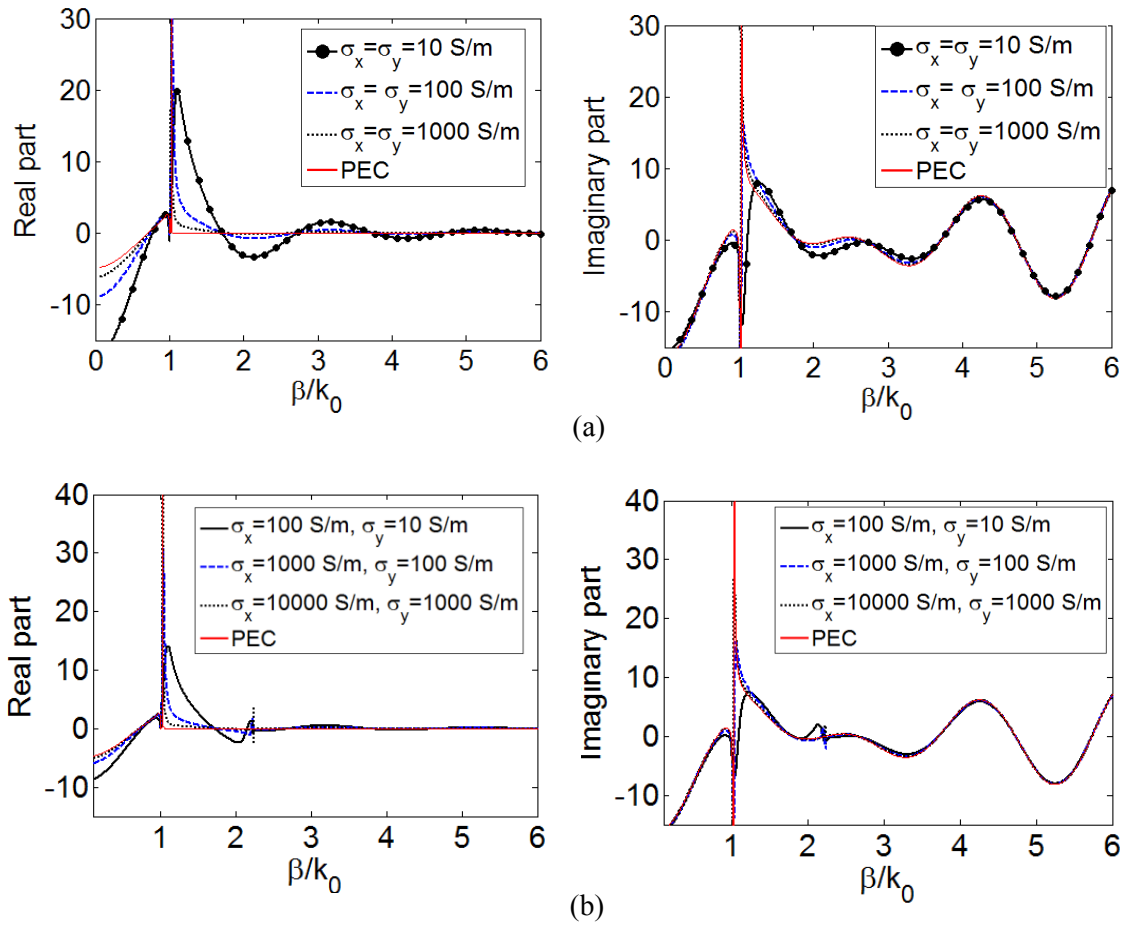

Figure 4.2. The complex integrand $\tilde{F}_x$ for (a) isotropic and (b) anisotropic ground plane.

$$\beta = k_0 \left[1 + \left(\frac{1}{2} \right) \left(\frac{\varepsilon_r - 1}{\varepsilon_r} k_0 h \right)^2 \right] \tag{4.39}$$

which corresponds to the zero of T_2 [85]. For a substrate with small loss, the SWP has a small negative imaginary part. For a CFC ground plane that is highly conductive along the y direction $(Z_y \to 0)$, it can be easily shown from (4.27) that the zeros of T_2 are also the zeros of Δ. Hence, the same TM surface waves of the slab grounded by PEC are excited also in the slab with composite ground. Similarly, we may conclude that when HED is along y direction and $Z_x \to 0$, the same SWPs exist when the slab is grounded by

a CFC or PEC. In order to calculate (4.38) for the slab with a CFC ground plane, first we study the behavior of integrand $\tilde{F}_x$ versus β and compare it with the case that slab is grounded by PEC. The slab is chosen to be electrically thin and also with small loss, which is valid for many practical cases.

By choosing f = 5 GHz, h = 2.5mm, ε_r = 5, and tanδ = 0.002, $\tilde{F}_x$ is evaluated at (x,y)=(λ/2,0) for different conductivity values for the ground plane as shown in Figure 4.2. It is observed that by increasing the conductivity, the integrand gets closer to that of the slab grounded by a PEC, showing an SWP at about $\beta = 1.02k_0$, which could be also calculated from (4.39). At the SWP location, $\tilde{F}_x$ shows a sharp change with noticeable magnitude. A small sharp change is also seen around k_e for anisotropic composites. It is due to this fact that when $\beta \to k_e$, then $k_1 \to 0$, setting the first term in (4.27) to zero which makes Δ to be an small non-zero value, especially when $Z_x - Z_y$ is small. However, $k_1 = 0$ is also a zero of the numerator of D and F coefficients. As a result, a slightly sharp change of $\tilde{F}_x$ occurs around $\beta = k_e$.

Since the observation point and source are at the same level (z = h), the integration in (4.38) converges slowly, which needs special treatment [85],[95]-[100]. Moreover, in order to take the integration over the real axis of complex plane, some techniques like singularity extraction are needed to deal with SWPs [99],[100]. By increasing the frequency or the dielectric thickness, the number of SWPs may increase, leading to a complicated problem which includes locating the poles and performing the integration near them. Some works uses a deformed integration path to avoid dealing with SWPs [101]. Following [101], we consider the contour P shown in Figure 4.3 and defined by

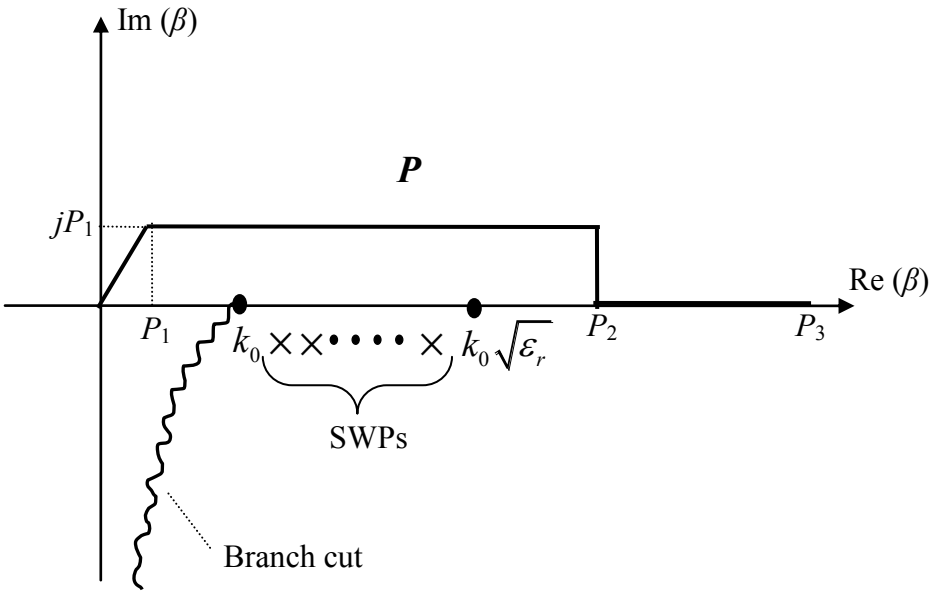

Figure 4.3. The integration contour path in the complex β-plane.

parameters P_1, P_2, and P_3. Without crossing the branch cut, the path fulfills the condition $\mathrm{Im}(k_2) < 0$. There is no concern about $\mathrm{Im}(k_1) < 0$ since (4.32) and (4.33) are even functions with respect to k_1. The path is deformed over $[k_0, k_e]$ so that no knowledge about SWP locations is required. Then it returns to the real axis at P_2 and is truncated at P_3 when convergence of the integral has been obtained.

The imaginary part of the integrand $\tilde{F}_x$ is oscillatory and diverges as β increases, as shown in Figure 4.2(b), making (4.38) converge slowly as beta increases. However, it should be noted that when $\beta \to \infty$ the behavior of both real and imaginary parts of $\tilde{F}_x$ for the slab with CFC ground plane converges to that of the slab grounded by PEC, independent of the CFC conductivity and anisotropy. The physical interpretation is that $\beta \to \infty$ implies $f \to 0$, hence from (4.1) we have $Z_x, Z_y \to 0$, making the ground plane to be like PEC. It is mathematically proven as follows. When $\beta \to \infty$, we have $k_1 \to j\beta$,

$k_2 \to -j\beta$, $\sin k_1 h \to je^{\beta h}/2$, and $\cos k_1 h \to e^{\beta h}/2$. The asymptotic values of D and F can be calculated from (4.24) and (4.26) as

$$D^{\infty} = \left(\frac{\beta^2 \tilde{J}_x e^{2h\beta}}{2\Delta^{\infty}}\right).\Big[\left(\omega^2\mu_0^2 k_x \beta^7\right) + Z_x Z_y\left(\omega^2\mu_0\varepsilon_0\varepsilon_r k_x\beta^7\right) + \left(Z_x k_x^2 + Z_y k_y^2\right)\left(j\omega^3\mu_0^2\varepsilon_0\varepsilon_r k_x\beta^4\right) - \left(Z_x k_y^2 + Z_y k_x^2\right)\left(j\omega\mu_0 k_x\beta^6\right)\Big] \tag{4.40}$$

$$F^{\infty} = \left(\frac{\beta^2 \tilde{J}_x e^{2h\beta}\varepsilon_{eff}}{2\Delta^{\infty}}\right).\Big[\left(\omega^3\mu_0^2\varepsilon_0 k_y \beta^6\right) + Z_x Z_y\left(\omega^3\mu_0\varepsilon_0^2\varepsilon_r k_y\beta^6\right) + \left(Z_x k_x^2 + Z_y k_y^2\right)\left(j\omega^4\mu_0^2\varepsilon_0^2\varepsilon_r k_y\beta^3\right) - \left(Z_x k_y^2 + Z_y k_x^2\right)\left(j\omega^2\mu_0\varepsilon_0 k_y\beta^5\right)\Big] \tag{4.41}$$

where superscript ∞ refers to $\beta \to \infty$. After some mathematical manipulation, $\tilde{E}_x^{\infty}$ is obtained from (4.32) as

$$\tilde{E}_x^{\infty} = \tilde{J}_x \frac{\left(k_0^2\varepsilon_{eff}k_y^2 - \beta^2 k_x^2\right)\left(\omega\mu_0\beta^3 e^{2h\beta}\right)}{2\Delta^{\infty}} \times \Big[-j\beta^4 Z_x + \beta^2 Z_y\left(j\omega^2\mu_0\varepsilon_0\varepsilon_r\right) + Z_x Z_y\omega\varepsilon_0\varepsilon_r\beta^3 + \omega\mu_0\beta^3 + \left(Z_x - Z_y\right)k_x^2\left(j\omega^2\mu_0\varepsilon_0\varepsilon_r + j\beta^2\right)\Big] \tag{4.42}$$

where $\varepsilon_{eff} = \left(\varepsilon_r + 1\right)/2$ and Δ^{∞} is the asymptotic value of (4.27) given by

$$\Delta^{\infty} = \beta^6\omega^2\mu_0\varepsilon_0\left(\frac{\varepsilon_r + 1}{4}\right)e^{2h\beta} \times\Big[-\beta^2\left(\beta Z_x + j\omega\mu_0\right)\left(-j\omega\varepsilon_0\varepsilon_r Z_y - \beta\right) - \beta^2 k_x^2\left(Z_x - Z_y\right)\Big]. \tag{4.43}$$

By considering the highest degree terms in the numerator and denominator of (4.42) and after more simplifying, $\tilde{E}_x^{\infty}$ is converted to

$$\tilde{E}_x^{\infty} = \tilde{J}_x \frac{\left(k_0^2 \varepsilon_{eff} - k_x^2\right)\left(-jZ_x \beta^2\right)}{\omega \varepsilon_0 Z_x \left(\varepsilon_r + 1\right)\beta^3} = \tilde{J}_x \frac{\left(k_0^2 \varepsilon_{eff} - k_x^2\right)}{\left(\varepsilon_r + 1\right)\beta}\left(\frac{-j}{\omega \varepsilon_0}\right). \tag{4.44}$$

When the slab is grounded by a PEC, $\tilde{E}_x^{\infty}$ is obtained directly from (4.34), which can be easily shown that it is equal to (4.44). Therefore,

$$\tilde{E}_x^{\infty}\,|_{CFC} = \tilde{E}_x^{\infty}\,|_{PEC} = \left(\frac{-j}{2\omega \varepsilon_0}\right)\left[\frac{k_0^2 \varepsilon_{eff} - k_x^2}{\varepsilon_{eff}\,\beta}\right] \tag{4.45}$$

and consequently,

$$\tilde{F}_x^{\infty}\,|_{CFC} = \tilde{F}_x^{\infty}\,|_{PEC} \tag{4.46}$$

where $\tilde{F}_x^{\infty}$ is the asymptotic, or also called as the static part of $\tilde{F}_x$. We get an advantage from the asymptotic equality in (4.46) to overcome the convergence problem of (4.38) as follows. The static part of the integrand in (4.38) is subtracted and added as

$$\int_0^{+\infty} \tilde{F}_x d\beta = \int_0^{+\infty} \left[\tilde{F}_x - \tilde{F}_x^{\infty}\,|_{CFC}\right] d\beta + \int_0^{+\infty} \tilde{F}_x^{\infty}\,|_{CFC}\; d\beta \tag{4.47}$$

so that in the right hand side of (4.47), the first term is a more rapidly converging integral, easily evaluated numerically. Substituting (4.46) in (4.47), the second term can be replaced by $I_x^{\infty} = \int_0^{+\infty} \tilde{F}_x^{\infty}\,|_{PEC}\; d\beta$. Pozar showed that I_x^{∞} has a closed-form expression as [102]

$$I_x^{\infty} = \left(\frac{-j}{4\pi\omega \varepsilon_0 \varepsilon_{eff}}\right)\left(\varepsilon_{eff} k_0^2 + \frac{\partial^2}{\partial x^2}\right)\left(\frac{e^{jk_0\sqrt{\varepsilon_{eff}}R_1}}{R_1} - \frac{e^{jk_0\sqrt{\varepsilon_{eff}}R_2}}{R_2}\right) \tag{4.48}$$

where $R_1 = \sqrt{x^2 + y^2}$, and $R_2 = \sqrt{x^2 + y^2 + 4h^2}$. In fact, (4.48) is the Green's function of an HED located at (0, 0, *h*) in the homogeneous medium with permittivity of ε_{eff}, and

grounded by PEC at z = 0. By replacing (4.48) in (4.47), the electric field can be calculated from (4.38).

In order to calculate E_y, by replacing (4.33) in (4.36), the above procedure can be applied so that I_y^{∞} can be obtained from

$$I_y^{\infty} = \left(\frac{-j}{4\pi\omega\varepsilon_0\varepsilon_{eff}} \right) \left(\frac{\partial^2}{\partial x \partial y} \right) \left(\frac{e^{jk_0\sqrt{\varepsilon_{eff}}R_1}}{R_1} - \frac{e^{jk_0\sqrt{\varepsilon_{eff}}R_2}}{R_2} \right). \tag{4.49}$$

4.3 Numerical Results

In this section, we evaluate the electric field E_x at the air-dielectric interface for the ground plane with different conductivity characteristics, and at different frequencies. The strength of HED moment is one (*Idx* = 1). By using the slab parameters given in previous section, the magnitude of E_x is calculated along the x-axis at y = 0 as shown in Figure 4.4. The results are obtained at two operating frequencies, f = 5 and 10 GHz. The results are compared with computations using CST MWS. Good agreement is seen. In the CST model, the 8λ × 8λ slab and ground plane are terminated by PML layers to approximate the assumption of a slab of infinite extent. We used about 1,800,000 mesh cells in CST simulations to get accurate results.

Figure 4.5 shows the effect of the conductivity tensor of the ground plane on E_x at z = h. Some fluctuation is observed for low values of σ_x and σ_y, but by increasing the conductivity in both directions, the electric field behavior moves toward that of the slab grounded by a PEC. When Z_x and Z_y gets small, $Z_x - Z_y$ gets small, hence, the anisotropic characteristic of the ground plane vanishes, making the behavior of the structure like isotropic case.

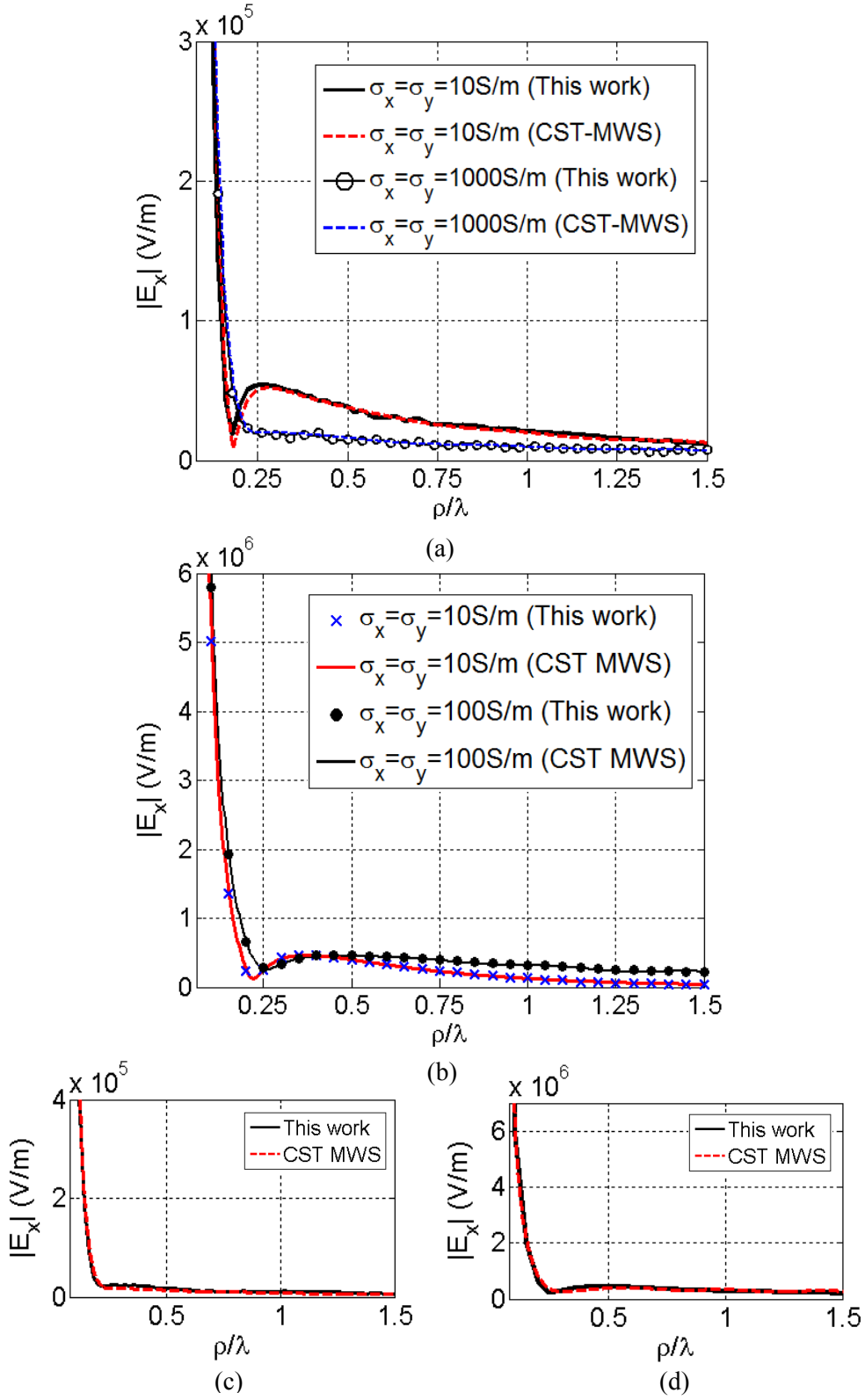

Figure 4.4. The magnitude of E_x along x-axis, (a) isotropic ground at f = 5 GHz, (b) isotropic ground at f = 10 GHz, (c) anisotropic ground with (σ_x, σ_y) = (1000, 100) S/m at f = 5 GHz, (d) anisotropic ground with (σ_x, σ_y) = (1000, 100) at f = 10 GHz.

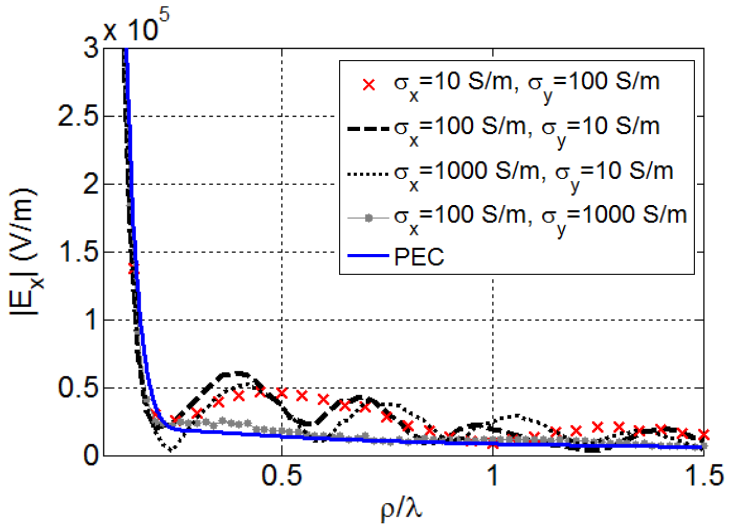

Figure 4.5. The effect of ground anisotropy on E_x at f = 5 GHz.

4.4 Summary

In this chapter, the Green's function was calculated for an infinitesimal HED on a dielectric slab over a CFC ground plane. The Green's function was evaluated for a RCCF CFC which is highly anisotropic, and a CNT CFC which has isotropic conductivity. Because these materials have high conductivity, they were modeled using a surface impedance. Using the spectral domain method, the expressions for the electric field components were derived. The numerical integration required to evaluate the Green's function was addressed in detail. It was shown that the electromagnetic fields at the air-dielectric interface depend on both the conductivity and anisotropic characteristics of the composite ground plane. The presented Green's function is versatile and can be used in the numerical modeling of any kind of microstrip structure with a CFC ground plane.

Chapter 5 : Reinforced Continuous Carbon Fiber Composites for Antenna Applications

Metals such as copper or aluminum are commonly used for the radiating element of antennas. However, the cost, fabrication procedure, and weight are some of the important parameters which limit the usefulness of metal antennas. In harsh environments, corrosion resistance and the adhesion between the radiating element and the substrate are major issues. Some recent studies have used various alternative materials as replacements for metals in the antenna structure [26]-[31]. In [26], a conducting-polymer patch antenna is proposed. Silver nanoparticle ink [28][29] and the metallo-organic conductive ink [30] are used to prepare the high-conductive material as a replacement of metal for RFID tag antennas. In [31], metalized foam is used to make a microstrip-patch antenna.

Copper is conductive but its conductivity is fixed. To change the frequency response of a copper antenna, a change in the geometry or dimensions is made. Composite antennas have an additional degree of freedom: the conductivity tensor of the composite. To change the frequency response of a composite antenna, it may be sufficient to change the value or tensor of the composite conductivity from which the antenna is made, without changing the geometry or dimensions.

In this chapter, we explore the use of RCCF composites in the antenna structures as an efficient alternative for copper. We also produced RCCF/MWCNT composite with improved conductivity which comprises RCCF material mixed with some MWCNTs. Many applications are considered for study: RFID, UWB, wireless, and mm-wave communication systems. The antennas are modeled with CST MWS and the simulation results are verified by experimental results.

High oxidation stability recommends RCCF composites for applications where metals cannot be used because of corrosion. Also, RCCF has a higher conductivity than many other kinds of composites. It is an effective replacement for metal when high shielding is required. As discussed in Chapter 2, the RCCF conductivity is anisotropic, being high along the direction of fibers, but low in the perpendicular direction. The anisotropic conductivity may cause a different surface current distribution than that in the isotropic case, which can affect the antenna performance.

5.1 RFID Tag Antenna Applications

RFID technology is extensively used in tracking and identifying objects in many applications [29],[30],[103]-[109]. The mostly used RFID frequency bands are UHF-RFID (902–928 MHz in North America, 866–869 MHz in Europe and 950–956 MHz in Japan) and the unlicensed wireless bands (2.4-2.484 GHz and 5.15-5.875 GHz). The main part of an RFID system is the antenna tag, which should be inexpensive, light and easy to fabricate.

In what follows, a well-known type of RFID antennas, namely the T-match bow-tie antenna [29], is considered for study. The return loss, radiation efficiency, gain, and

bandwidth of the antenna are obtained with the radiating element made of composite and compared with a metal element [110].

The T-match folded bow-tie RFID antenna is shown in Figure 5.1(a). The antenna is excited by a lumped port between arms of the T. The impedance of the lumped port is chosen as 380 Ω to match the input resistance of the RFID microchip (TI RI-UHF-Strap-08 IC) [111] at the port. The radiation element is placed on a 130 mm × 80 mm substrate with dielectric constant $\varepsilon_r = 3.4$, $\tan\delta = 0.08$. The return loss of the antenna with a copper radiation element is shown in Figure 5.1(b). The gain and radiation efficiency of the copper antenna are 2.4 dB and 97%, respectively.

For antenna EM simulations, we characterize one specific RCCF composite sample with a conductivity of 3500 S/m along fiber direction and 10 S/m perpendicular to the fibers. CST MWS enables us to model anisotropic materials using the permittivity tensor. Since the direction of fibers, leading to anisotropic conductivity, plays an important role on the performance of antenna, two antennas were modeled: one having the fibers oriented in the *x* direction in Figure 5.1(a), and the other with the fibers in the *y* direction. The antenna with the fibers oriented in the direction of current flow on the metal antenna, that is, the *x* direction, has similar behavior to the metal antenna. The return loss of the RCCF antenna with *x*-directed fibers is shown in Figure 5.2(a) for different thicknesses of composite. Compared to the metal antenna, the resonant frequency is been shifted upwards to about 2450 MHz in the RFID upper band. The reason of this shift can be explained by comparing the current flow on the composite radiating element in Figure 5.2(b) with that on the metal antenna. The current flow on the metal antenna resembles

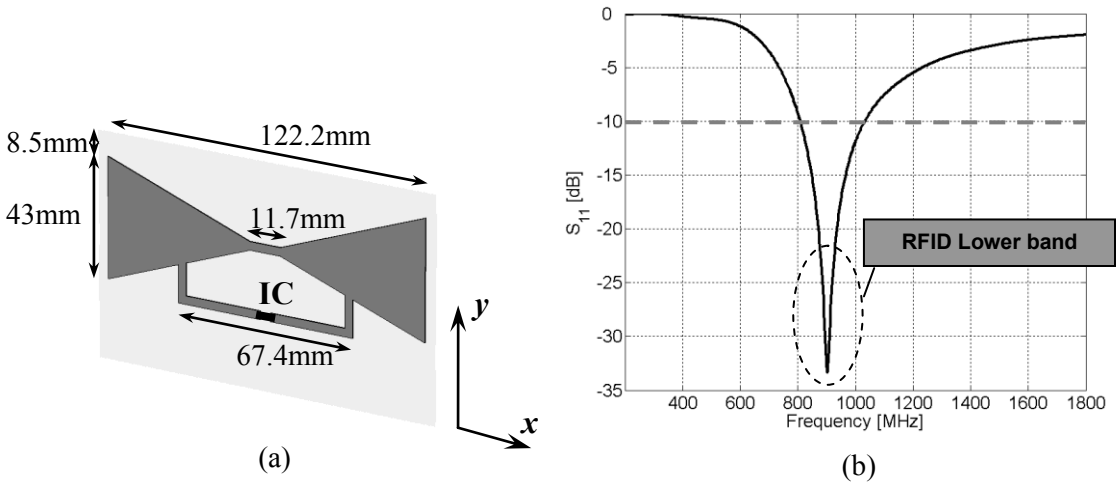

Figure 5.1. (a) T-match folded bow-tie RFID antenna, (b) Return loss of the antenna with radiation element made of copper.

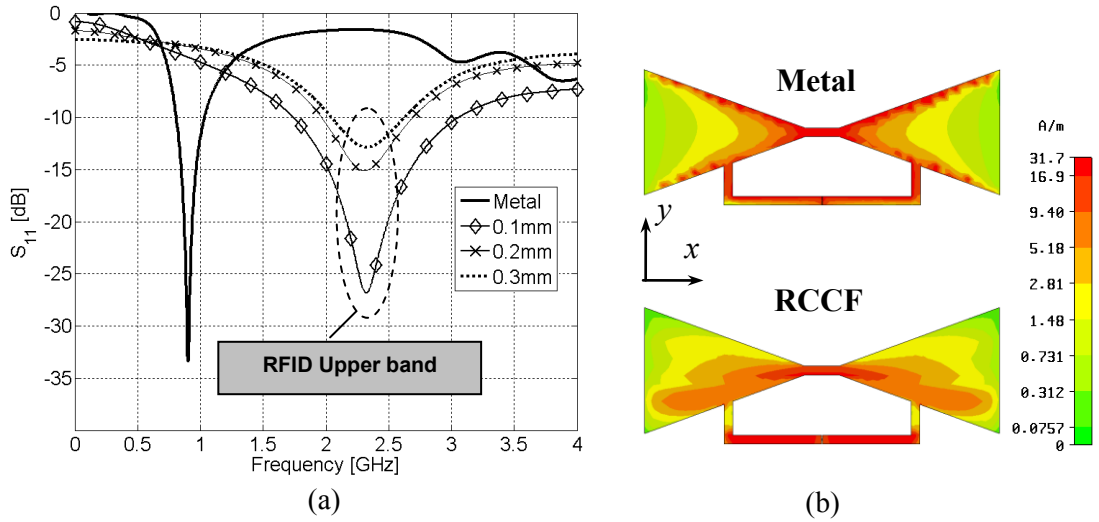

Figure 5.2. (a) Reflection coefficient of RCCF antenna, (b) Current distribution on the radiation element at resonant frequency.

that on a dipole, using the full length of the antenna, corresponding to resonance at lower RFID band. However, the current flow on the composite antenna is confined to the section of the antenna adjacent to the T-match, and the behavior is more like that of a short dipole antenna, with a correspondingly higher resonant frequency. The current flow at the ends of the T-match section is quite small.

Due to the much lower conductivity of composites compared to metals, the ohmic loss (R_{Loss}) of the composite radiating element is higher. Therefore, the gain and radiation efficiency (η) of composite antenna are lower than of a metal antenna. The ohmic loss of a conductive box with effective conductivity of σ_{eff} can be expressed as

$$R_{loss} = \frac{L}{\sigma_{eff} A_{eff}} \tag{5.1}$$

where A_{eff} is the effective area along a current path of length L. For a composite antenna the current flows inside the volume of radiating element, A_{eff} can be controlled by changing the conductivity itself and hence the skin depth, and the thickness t. Hence the gain of the composite antenna can be adjusted by changing both t and σ_{eff}.

The maximum read-range ($d_{\max}$) of an RFID antenna is obtained from [106]

$$d_{\max} = \frac{\lambda}{4\pi}\sqrt{\frac{G_{tag}.EIRP_t}{P_{chip}}} \tag{5.2}$$

where G_{tag}, $EIRP_t$ and P_{chip} are the gain of RFID tag, maximum value of transmitting power of reader and the sensitivity power level of RFID IC, respectively. With $EIRP_t$ = 0.5 W, the maximum allowed value, and P_{chip} = 1 mW [105], $d_{\max}$ of antenna with a copper radiating element is 76.52 cm.

The radiation efficiency and gain of the antenna made of 0.2 mm-thick RCCF are computed as 39.27% and -0.2 dB, respectively. Using (5.2), the maximum read-range of RCCF antenna is obtained as $d_{\max}$ = 21.3 cm. The radiation efficiency and -10dB bandwidth of the antenna for different thicknesses is reported in Table 5.1. Although the

Table 5.1: Radiation Efficiency and -10dB BW of the RCCF Composite Antenna

Thickness (mm)	η (%)	BW (MHz)
0.1	35.17	1320
0.2	39.27	730
0.3	40.1	581

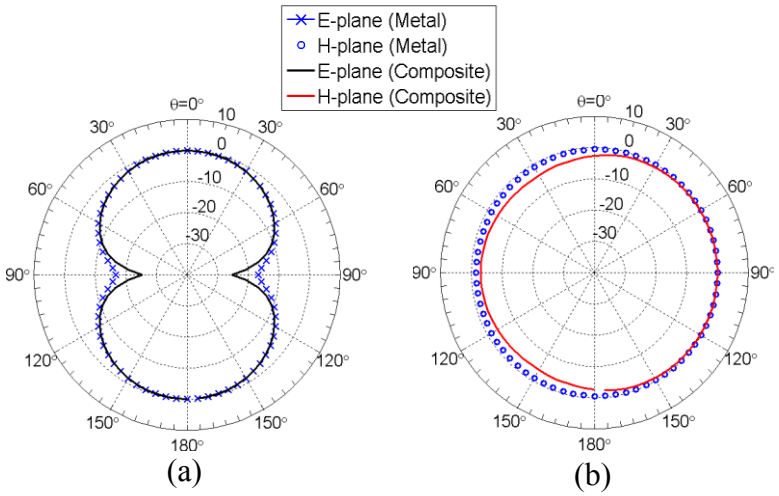

Figure 5.3. Normalized radiation pattern of bow-tie antenna, (a) *E*-plane, (b) *H*-plane.

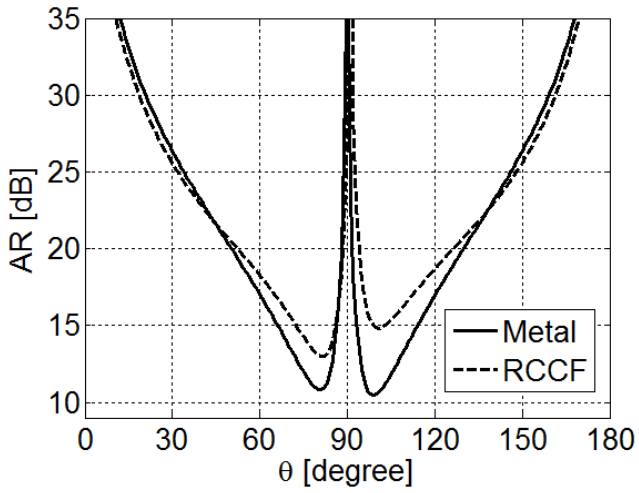

Figure 5.4. *E*-plane axial ratio of bow-tie antenna with different radiating element.

gain/read-range of the composite antenna is relatively low compared to the metal antenna, it should be noted that the antenna covers the microwave RFID frequency band

centered at 2.45 GHz along with a wide bandwidth (BW = 1.32 GHz) due to the interesting properties of RCCF composite material.

The normalized radiation pattern in both the *E*- and *H*-plane at frequency of resonance is shown in Figure 5.3. It is observed that using an RCCF composite instead of metal hardly changes the radiation pattern at all. However, the polarization property of the RCCF antenna would be affected due to the anisotropic property of the RCCF material. Figure 5.4 shows the axial ratio of bow-tie antenna at *E*-plane. It is observed that the polarization purity of RCCF composite antenna is improved compared to the metal antenna.

5.2 Wideband and UWB Applications

UWB technology has experienced a significant rise in popularity in the past few years. The Federal Communication Commission (FCC) allocated the spectrum from 3.1 to 10.6 GHz for UWB technology with EIRP less than -41.3 dBm/MHz [112]. So far different kinds of UWB antennas have been introduced in the literature [114]-[118]. These antennas exhibit good impedance stability over the very large frequency band.

We explore using RCCF composites for wireless and UWB antenna applications [119]. The metal radiating element of a wideband monopole antenna is replaced with composite material, and the performance is investigated by measurement and by numerical simulation. In order to enhance the conductivity of the RCCF composite, a small volume fraction of MWCNTs is added to the RCCF material. MWCNTs are about 1000 times smaller than the fibers in RCCFs.

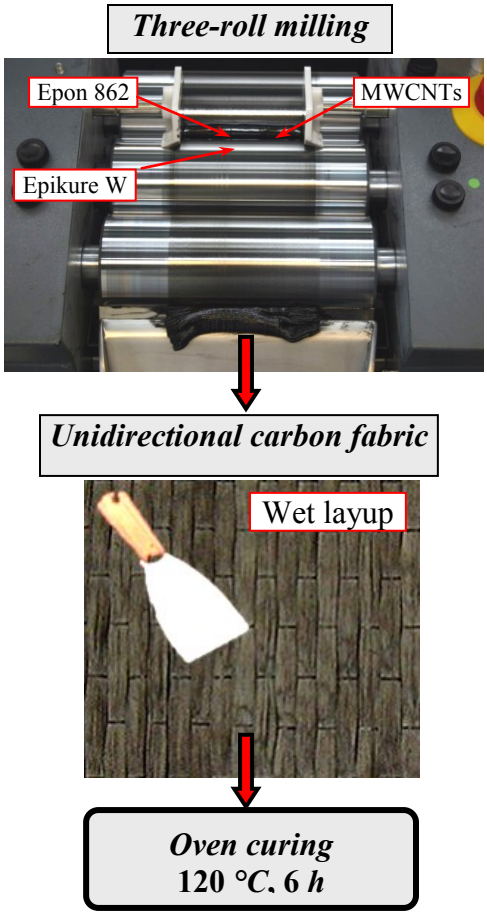

Figure 5.5. Fabrication procedure for RCCF/MWCNT composite material [119].

The method of preparation of an RCCF sample loaded with MWCNTs is illustrated in Figure 5.5. The composite samples were produced by CONCOM and details are given in [119]. The epoxy resin, the curing agent (26.4 wt%) and a volume fraction of MWCNTs produced by NanoLab are weighed and three-roll-milled. After degassing the mixture in a vacuum oven, one ply of unidirectional carbon cloth is impregnated with the mixture and placed between two aluminum plates and cured at 120 °C for 6 hours. An MWCNT loading of 2% is used for this antenna study.

In order to characterize the composite sample, we use standard G-band (3.95-5.85 GHz) and X-band (8.2-12.4 GHz) rectangular waveguides. The thickness of composite is

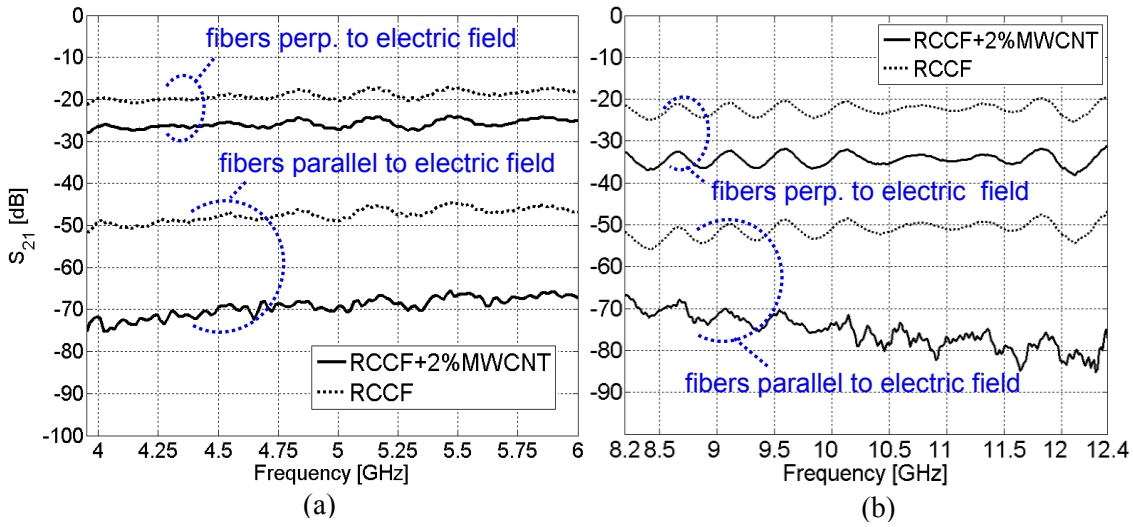

Figure 5.6. Measured S_{21} parameter using standard waveguides. (a) magnitude of S_{21} parameter over G-band, (c) magnitude of S_{21} parameter over X-band.

0.6 mm. The scattering parameters were measured with the fibers parallel to and perpendicular to the TE_{10} electric field vector, to obtain the magnitude of S_{21} reported in Figure 5.6. The figure shows that by adding 2% wt of MWCNT, the magnitude of S_{21} decreases by about 20 dB with the fibers parallel to the electric field, and by about 8 dB with the fibers perpendicular. The effective conductivity of the RCCF/MWCNT composite over the desired frequency range is found to be 4000 S/m along fiber direction and 150 S/m perpendicular to the fibers. As expected, the conductivity of RCCF is not significantly frequency dependent [25].

Figure 5.7 shows the EM model of monopole antenna developed in CST MWS. The antenna is fed through a 50-ohm SMA connector at the bottom of radiating element. The antenna geometrical parameters are $G_1 = G_2 = 200$ mm, $L_1 = 65$ mm, $L_2 = 66$ mm, $g = 1.5$ mm and $d = 1$ mm. The monopole antenna thickness is $t = 0.6$ mm. In simulations, we consider composite material as a homogeneous anisotropic medium as characterized by standard waveguides. As a result, the composite antenna performance depends on the

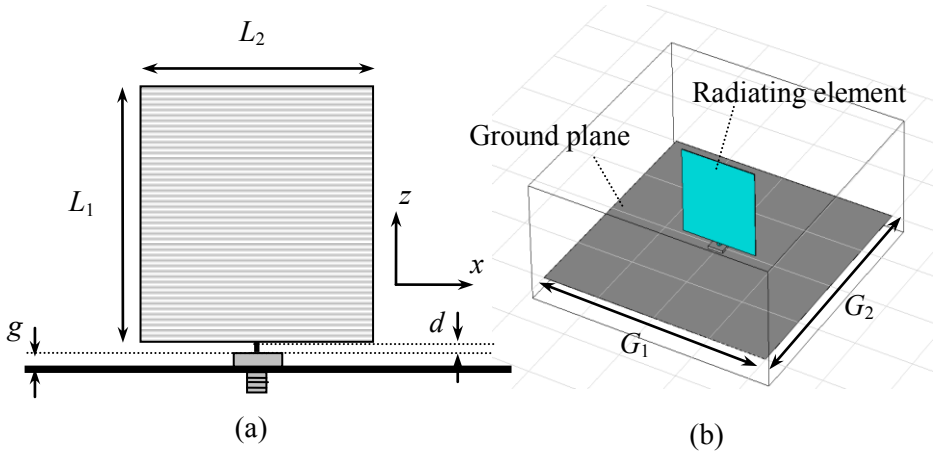

Figure 5.7. Monopole antenna, (a) Schematic front view, and (b) EM model in CST MWS.

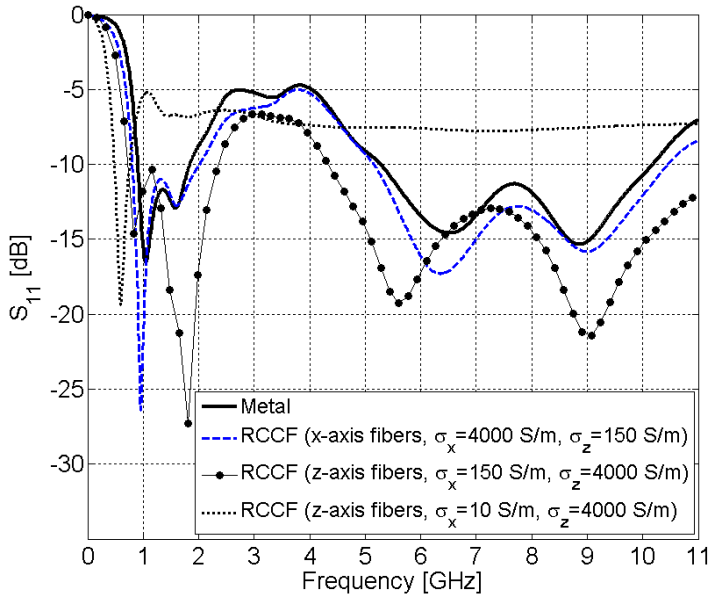

Figure 5.8. Simulated reflection coefficient of the monopole antenna with metal and composite radiating element.

direction of fibers inside the radiating element. In order to address this issue, we study two different configurations: fibers along the *x*-axis and the *z*-axis. The calculated reflection coefficient of the monopole composite antenna is shown in Figure 5.8 for different fiber orientations. When the direction of carbon fibers is along *x*-axis, parallel to the ground plane, the composite antenna's reflection coefficient is very similar to the

metal antenna. However, when the fibers are parallel to z-axis, the reflection coefficient of the composite antenna is quite different for σ_x =10 S/m and 150 S/m. With the low value, the reflection coefficient is almost constant with frequency. With the high value, the reflection coefficient is somewhat similar to the metal antenna. This phenomenon can be understood by plotting the current distribution on the radiating element, as shown in Figure 5.9. With the fibers horizontal or parallel to the ground plane, part (b) of the figure shows that the current on the horizontal edges is similar to that on the metal antenna in part (a). Note that there is more current on the vertical edges of the metal antenna, particularly at 900 MHz. But with the fiber vertical and low conductivity in the horizontal direction, part (c) shows that the current distribution is reminiscent of a monopole antenna and quite unlike that of the metal antenna. When the horizontal conductivity is increased to 150 S/m, the current distribution in part (d) resembles that of the metal antenna of part (a), including the currents on the vertical edges. Note that the frequencies in Fig. 6 of 2, 6 and 9 GHz were chosen near the minima in the reflection coefficient curves of Figure 5.8. However, for the top row the frequencies of 900 MHz, 800 MHz, 750 MHz and 560 MHz were chosen to be the lowest frequency where the reflection coefficient in Figure 5.8 is -10 dB. Orienting the fibers in the horizontal direction (x-directed) supports current flow along the bottom edge of the patch, making the current in Figure 5.9(a) and (b) similar, especially at 2, 6 and 9 GHz. Current in the vertical direction is suppressed. When the fibers are vertical with a low conductivity of 10 S/m in the horizontal direction, Figure 5.9(c), the current is forced to flow in the center of the radiating element, and is effectively suppressed in the horizontal edges. As a result, the resonant modes are then quite different than those of the metal antenna.

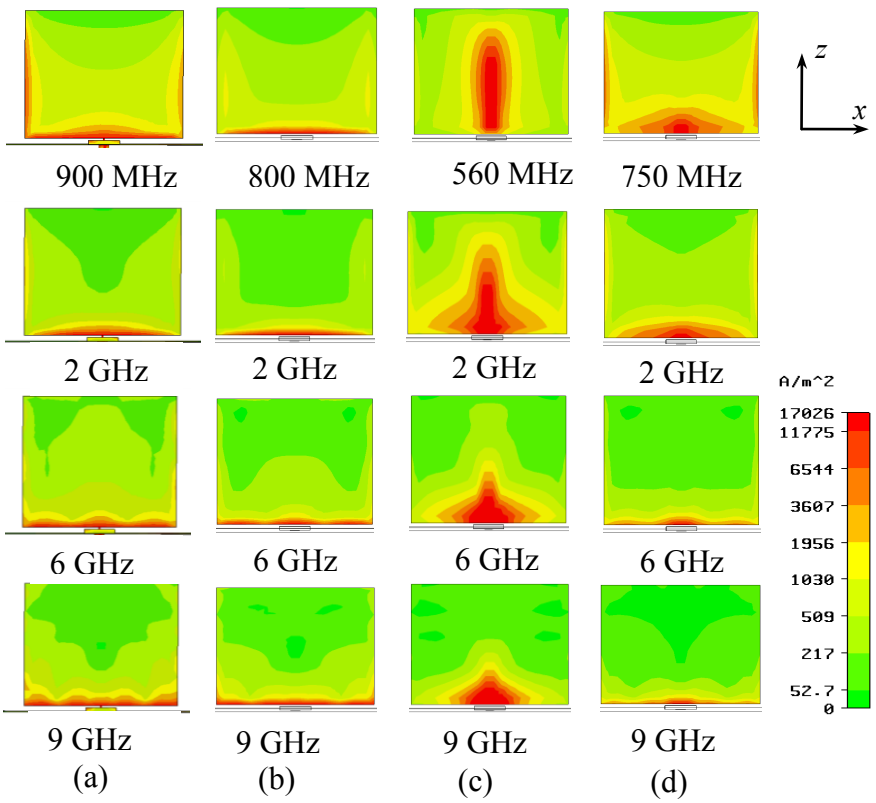

Figure 5.9. The current distribution on monopole antenna at different frequencies, (a) Metal antenna, (b) Composite antenna with *x*-directed fibers, (c) Composite antenna with *z*-directed fibers (σ_x=10 S/m), and (d) Composite antenna with *z*-directed fibers (σ_x=150 S/m).

The current of Figure 5.9(c) is like a monopole at its fundamental resonance, at 560 MHz. The second and third resonances might be expected at 1680 and 2800 MHz, but the reflection coefficient of Figure 5.8 shows no resonant behavior at these frequencies. Figure 5.9(d) shows that increasing the horizontal conductivity to 150 S/m restores the behavior to be similar to that of the metal antenna.

Figure 5.10 shows a computational study, using the CST MWS model, of the effect of the sample thickness and the conductivity on the composite antenna performance. No data is provided in the frequency range from 2 to 5 GHz, where the reflection coefficient, see Figure 5.8, is between -10 and -4 dB, and the antenna is not useful. In Figure 5.10(a),

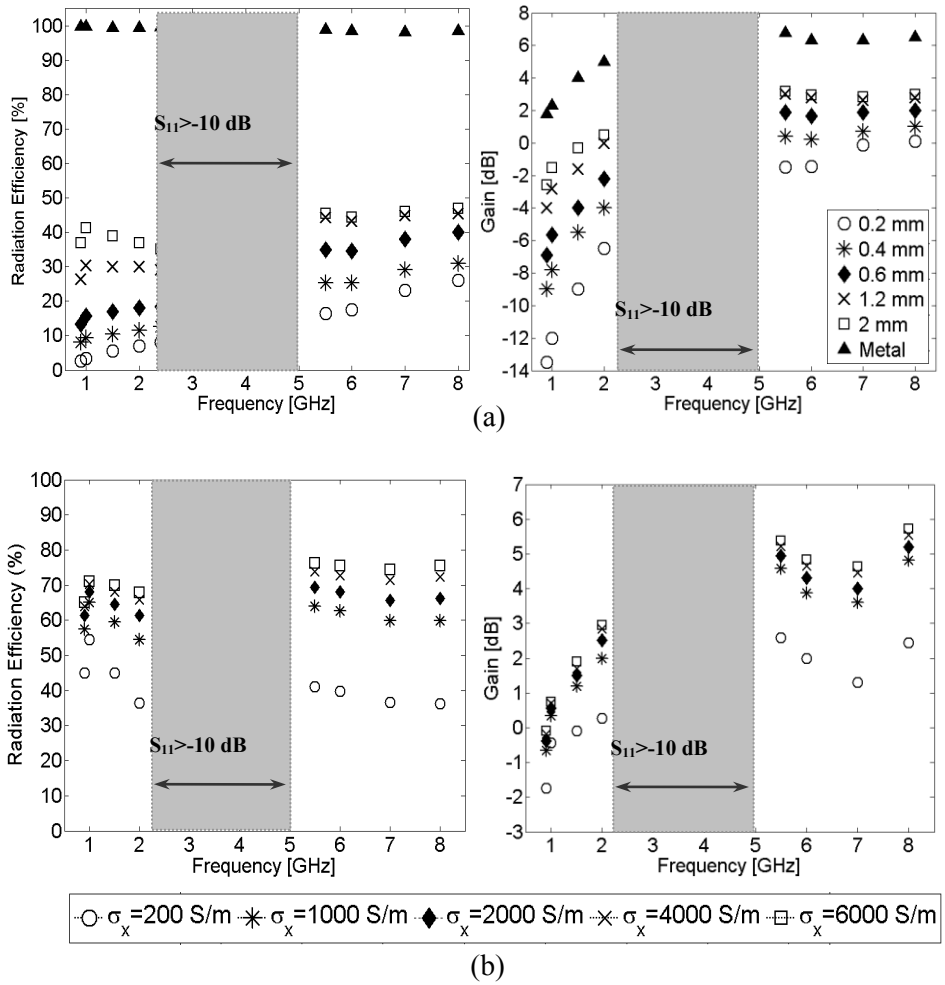

Figure 5.10. The efficiency and peak gain of composite antenna versus: (a) Thickness for a horizontal conductivity of 4000 S/m and a vertical conductivity of 10 S/m; and (b) Conductivity in the horizontal direction for a thickness of 0.6 mm and a vertical conductivity of 150 S/m.

the conductivity in the *x*- or horizontal direction is 4000 S/m and in the *z*- or vertical direction is 10 S/m. Figure 5.10(a) shows that the radiation efficiency can be improved 20 to 30% by increasing *t*. but increasing the thickness beyond the skin depth does not much increase the efficiency. Figure 5.10(a) also shows that the gain of the composite antenna is about 4 dB lower than metal antenna for the thickest composite. Figure 5.10(b), for a thickness of 0.6 mm and a vertical conductivity of 150 S/m, shows that if the horizontal

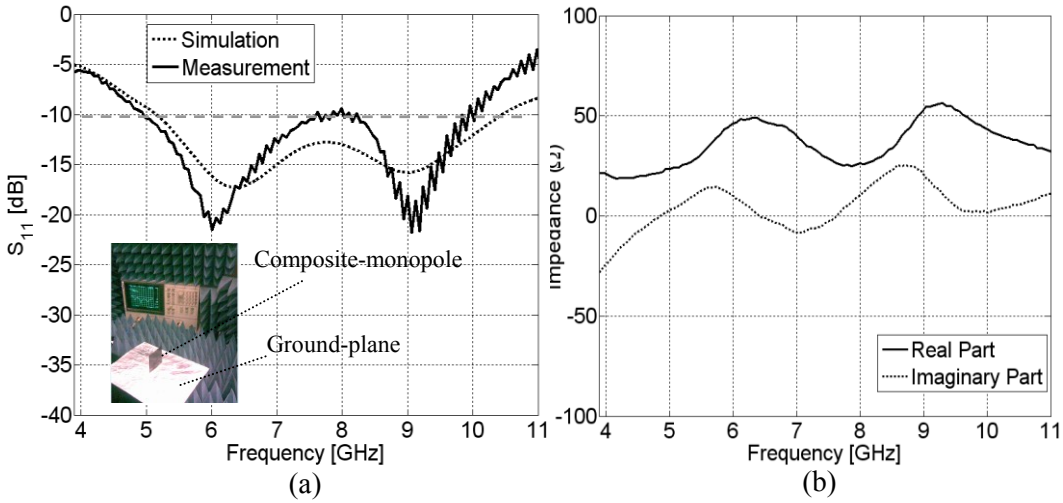

Figure 5.11. (a) Reflection coefficient of monopole RCCF/MWCNT composite antenna, (b) Measured input impedance.

conductivity can be increased, then the gain and efficiency also increase. By adding MWCNTs to the RCCF composite, we can increase the conductivity of composite along both fiber directions, leading to enhance the gain and radiation efficiency.

In order to investigate the composite antenna performance experimentally and to verify the simulation results, the composite monopole antenna of Figure 5.7 is fabricated using the produced RCCF/MWCNT composite material. The composite antenna is installed such that the direction of fibers is parallel to *x*- or horizontal axis. The antenna geometrical parameters are $G_1 = G_2 = 200$ mm, $L_1 = 65$ mm, $L_2 = 66$ mm, $t = 0.6$ mm, $g = 1.5$ mm and $d = 1$ mm. A thin aluminum sheet is used as a ground plane and the composite antenna is fed through 50-ohm SMA connector.

Using the HP8720 network analyzer, the reflection coefficient of fabricated RCCF/MWCNT monopole antenna is measured as displayed in Figure 5.11(a). Good agreement is observed between simulated and measured results. The reflection coefficient is better than 10 dB from 4.9 to 10 GHz, which includes the WLAN frequency range of

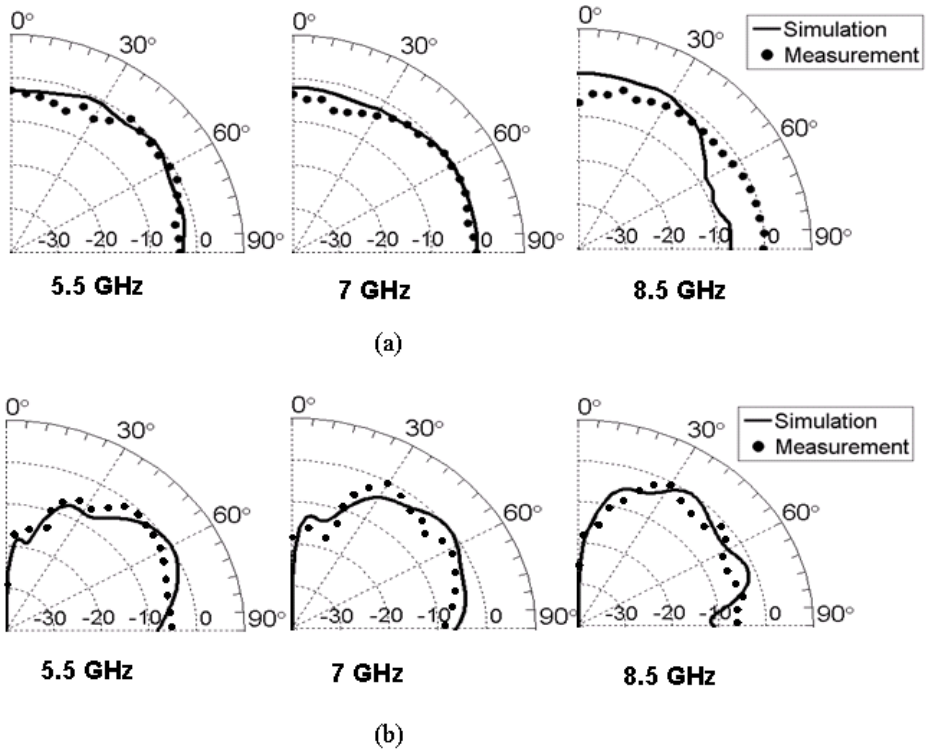

Figure 5.12. Normalized radiation pattern of composite antenna at (a) *H*-plane (*xy*), and (b) *E*-plane (*yz*).

5.15 to 5.825 GHz. The input impedance of the composite antenna is displayed in Figure 5.11(b).

The normalized radiation patterns in the *E*- and *H*-planes were measured using a standard ridge horn antenna (EMCO-3115) as a receiver. Figure 5.12 shows the radiation patterns at 5.5, 7 and 8.5 GHz. Due to the symmetry, only one-quarter of the *H*- plane and half of *E*-plane is considered. The polarization of the composite antenna at boresight angle ($\theta = \varphi = 90^{\circ}$) is also evaluated. The ratio of antenna gain for θ-polarization to φ-polarization, namely G_θ/G_φ, is displayed in Figure 5.13 (a). It can be seen that G_θ is 5 dB greater than G_φ in the measurement over almost the entire frequency range. We also investigated the polarization for $\varphi = 0^{\circ}$, 30°, 45°, and 60°, not shown here, and we found that the antenna shows almost $G_\theta/G_\varphi > 5$ dB at these angles.

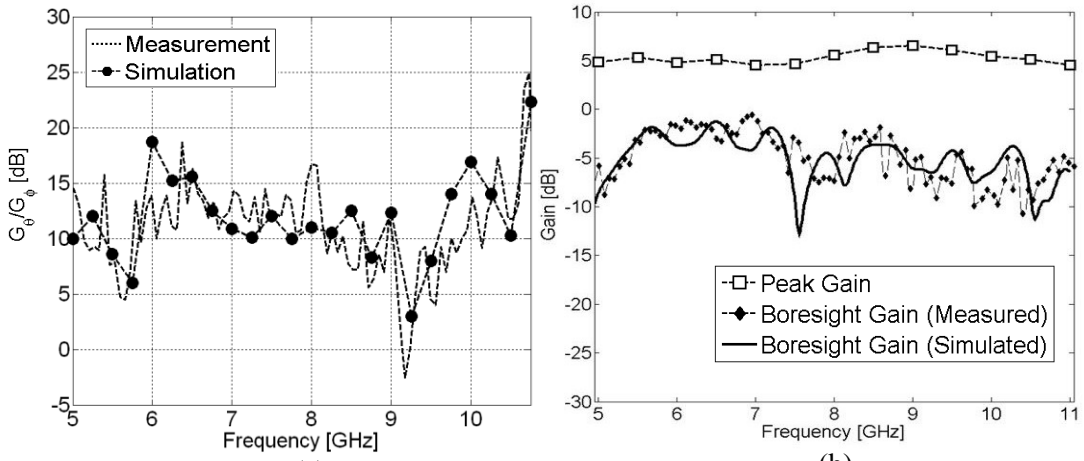

Figure 5.13. (a) G_θ/G_φ at boresight angle (θ=φ=90°), and (b) Boresight and peak gain of the monopole composite antenna.

According to Figure 5.10(b), the largest gain over wireless frequency band of the composite antenna in the CST MWS simulation varies between 4.7 dB and 5.2 dB. In order to validate the simulation results, the boresight gain of the composite antenna is measured. The IEEE standard antenna gain can be obtained by means of the antenna transfer function. Two identical composite antennas are considered in a Tx/Rx setup in front of each other, so that the $S_{21}(f)$ of two antennas can be written as

$$S_{21}(f) = H_{Tx}(f) H_{CH}(f) H_{RX}(f) \tag{5.3}$$

where $H_{TX}(f)$ and $H_{RX}(f)$ are the Tx and Rx antenna transfer functions, respectively. Furthermore, $H_{CH}(f)$ is the channel transfer function in free space defined as $\lambda/4\pi R$, where R is the separation distance between the antennas. The antenna gain can be calculated from

$$G(f) = H_{TX}(f) H_{RX}(f) \left(\left(1 - |S_{11}(f)|^2\right) . \left(1 - |S_{22}(f)|^2\right) \right)^{-\frac{1}{2}} \tag{5.4}$$

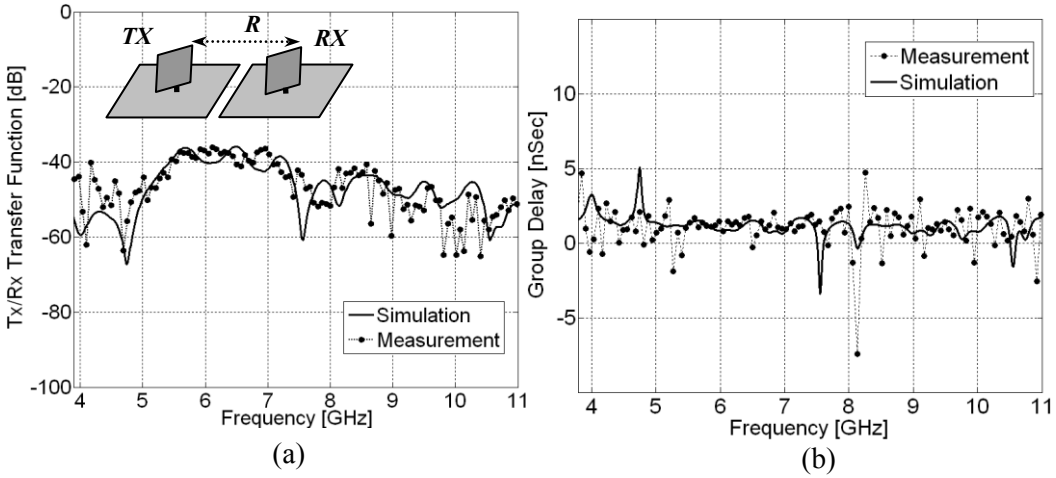

Figure 5.14. Composite antenna Tx/Rx setup transfer function, (a) Magnitude, (b) Group delay.

where $S_{11}(f)$ and $S_{22}(f)$ are the input reflection coefficient of the Tx and Rx antennas, respectively. By using (5.3), (5.4) can be written as

$$G(f) = S_{21}(f)\left(H_{CH}(f)\right)^{-1}\left(\left(1-|S_{11}(f)|^2\right).\left(1-|S_{22}(f)|^2\right)\right)^{-\frac{1}{2}} \tag{5.5}$$

which gives the measured boresight gain of the antenna. Figure 5.13(b) shows the measured boresight gain, using two identical composite antennas separated by R = 25 cm. Since the composite antenna has a wide impedance bandwidth of 4.9 to 10 GHz, it could be used in ultra-wideband (UWB) communication systems in the 3.1 to 10.6 GHz band. The dispersive behavior of an ultra-wideband antenna should be considered [114]-[117], in both the frequency domain and the time domain. The frequency domain antenna dispersion characteristics can be defined by the magnitude of Tx/Rx transfer function $|S_{21}|$ and the group delay $-d\varphi/df$, where φ is the angle of S_{21}. The Tx/Rx transfer function of the composite antennas in the front of each other ($\theta = 90^{\circ}$, $\varphi = 90^{\circ}$) is displayed in Figure 5.14. A fairly constant group delay shows that the antenna has low dispersion. When the group delay of antennas shows a highly frequency dependant behavior, the time domain

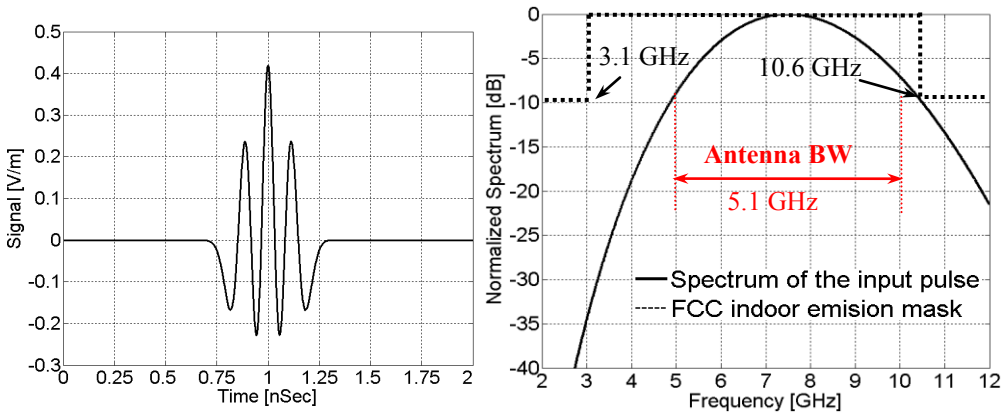

Figure 5.15. The single-band scheme, (a) Pulse signal, (b) Normalized spectrum.

pulse is considerably distorted due to the nonlinearity of phase. Specifically for UWB pulse signals, the group delay variations may lead to high level of error in wireless/UWB communication systems. It is very desirable to have an almost constant group delay over the frequency range of interest. In time domain characterization, the antenna can be verified for single-band and multiband cases [120]. In a single-band scheme which is usually considered in antenna analysis, the entire frequency band is allocated to one pulse. Time domain analysis is performed to calculate the fidelity factor between transmitted and received UWB pulses in Tx/Rx setups [115]-[117], [121].

A UWB pulse source is designed using the derivatives of a Gaussian pulse [122], to cover the desired frequency range. To cover 4.9 to 10 GHz, the eighth derivative of the Gaussian pulse function was used, so the pulse source is given by

$$s(t) = A_{\max}\left[105 - 420\left(\frac{t}{\delta}\right)^2 + 260\left(\frac{t}{\delta}\right)^4 - 38\left(\frac{t}{\delta}\right)^6 + \left(\frac{t}{\delta}\right)^8\right].\exp\left(\frac{-t^2}{2\delta^2}\right) \qquad (5.6)$$

where A_{max} is the peak power spectral density that FCC allows for UWB applications. The parameter δ can be selected in order to satisfy the FCC spectral mask. With A_{max} =

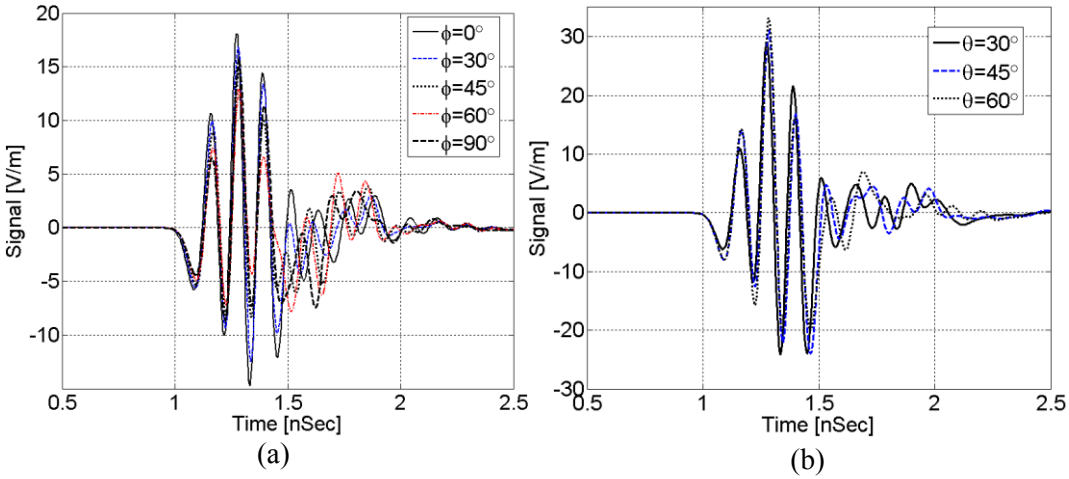

Figure 5.16. Virtual probes signals: (a) *H*-plane, (b) *E*-plane.

3.2 mV/m and δ = 60 ps, the pulse signal and its normalized Fourier transform are shown in Figure 5.15.

For wireless systems using UWB antennas, it is critical to evaluate the dispersive behavior for different angles between Tx and Rx antennas. This is due to the fact that the antenna could have low dispersion in some limited angular ranges, but have high dispersion for other angles. Using MWS, we simulated a transceiver setup consisting of the composite antenna as the transmitter and nine virtual probes (co-pol) as receivers. The virtual probes are located in both the *xy*- or *H*- plane at $\varphi = 0^{\circ}, 30^{\circ}, 45^{\circ}, 60^{\circ}$ and 90° and in the *yz*- or *E*-plane at $\theta = 30^{\circ}, 45^{\circ}, 60^{\circ}$. Note that the probe located at $\theta = 90^{\circ}$ is identical for the *H*- and *E*-planes and also the transmission/reception at $\theta = 0^{\circ}$ of *E*-Plane would be very poor because it is a null in the radiation pattern. The received probe signals are illustrated in Figure 5.16. The fidelity factor between virtual probe signals and the transmitted pulse is derived from the response in Figure 5.16, and is reported in Table 5.2. It is observed that the fidelity factor for the composite antenna is 0.83 or greater showing that the antenna does not impose significant distortion on the transmitted UWB pulse.

Table 5.2: Fidelity Factor between Transmitted Pulse and Virtual Probes Signal

***H*-plane (*xy*)**					***E*-plane (*yz*)**		
$\varphi = 0^\circ$	$\varphi = 30^\circ$	$\varphi = 45^\circ$	$\varphi = 60^\circ$	$\varphi = 90^\circ$	$\theta = 30^\circ$	$\theta = 45^\circ$	$\theta = 60^\circ$
0.93	0.946	0.91	0.83	0.899	0.882	0.914	0.938

Table 5.3: Fidelity Factor of TX/RX Setups

Tx/Rx Setups	**Face to Face**	**Side to Side**
Simulation	0.911	0.917
Measurement	0.89	0.93

To verify the calculations for Table 5.2, the fidelity factor was computed using the frequency domain transfer function S_{21} as follows. Consider a transceiver setup composed of two identical composite antennas, and transmit the pulse of (5.6) with spectrum $S_t(f)$ shown in Figure 5.15(b). The received signal in the time domain is given by the inverse Fourier transform as

$$s_r(t) = \Im^{-1}\left[S_t(f).S_{21}(f)\right]. \tag{5.7}$$

This relation was used to find the pulse response for both face-to-face ($\theta = \varphi = 90^\circ$) antennas and side-to-side ($\theta = 90^\circ$, $\varphi = 0^\circ$) antennas, and the fidelity factor was calculated as in Table 5.3. The calculation was done using the transfer function calculated with CST MWS, and using the measured transfer function, and Table 5.3 shows reasonable agreement. Also, the values in Table 5.3 agree reasonably with the direct calculation of Table 5.2.

5.3 Performance of Microstrip Patch Antenna on an RCCF Composite Ground Plane

There are many antennas mounted on or integrated to the surface of the mobile vehicles for different communication systems, radar, navigation, surveillance and so on. Showing low level of drag and being suitable for conformal applications, planar microstrip antennas are a very good candidate to be installed on such vehicles [123]. In many cases, the body of vehicle is used as the ground plane for the antennas. Therefore, investigating the performance of such antennas operating on a composite ground plane is of interest.

We investigated the performance of a metal patch antenna operating on a ground plane made of RCCF composite material, both numerically and experimentally [124]. The effect of fibers direction on the impedance bandwidth of the antenna was studied. Due to the lower conductivity of composite material compared to the metals, the antenna with composite ground plane is more lossy, leading to lower radiation efficiency. The gain and radiation pattern of the antenna with composite ground plane was evaluated and also compared to that of antenna with copper ground plane.

A sheet of RCCF composite material was provided by CONCOM using the preparation method explained in [124]. Standard G-band (3.95-5.85 GHz) waveguides with cross-section dimension of 47.548 × 22.148 mm^2 were used for characterization. The effective conductivity of the RCCF composite over the desired frequency range is 1500 S/m along fiber direction and 15 S/m perpendicular to the fibers.

Figure 5.17(a)-(b) show the EM model of a microstrip patch antenna developed in CST MWS, operating in a frequency band centered at 5.6 GHz. The antenna is fed

through a 50-ohm SMA connector from the bottom of the ground plane. The square patch (W = 16.5 mm) is printed on RT/Duroid 5880 substrate (ε_r = 2.2, tanδ = 0.0009) with thickness of 1.5 mm. The size of substrate is $L_1 \times L_2$ = 25×28 mm^2. Other geometrical parameters are d = 12.5, and g = 7.25 mm. The ground plane of the antenna is a 0.8 mm-thick RCCF composite material where the direction of carbon fibers is equally oriented by α degree with respect to x-axis. The size of the RCCF ground plane is $D_1 \times D_2$ = 60 × 60 mm^2.

The reflection coefficient of the antenna with copper and RCCF ground plane is shown in Figure 5.17(c). It is observed that the resonant behavior of the antenna is taken away by rotating fibers toward so that they are parallel to the y-axis ($\alpha = 90^{\circ}$) the antenna is no longer resonant. The reason can be explained by the current distribution on the ground plane. In Figure 5.18, the surface current distribution of the copper ground plane is compared with that of RCCF for $\alpha = 0\circ$ and $\alpha = 90^{\circ}$. It is observed that the x-directed fibers support a current distribution quite similar to that on the copper ground, leading to similar resonant behavior and impedance matching. However, for y-directed RCCF ground plane ($\alpha = 90\circ$), the current is forced to flow in y-direction, leading to a current distribution completely different from that in copper ground, and to poor impedance matching. Therefore, when the fibers are oriented in the direction of current flow in the copper ground plane, the RCCF ground plane can support the same current distribution as the copper ground plane.

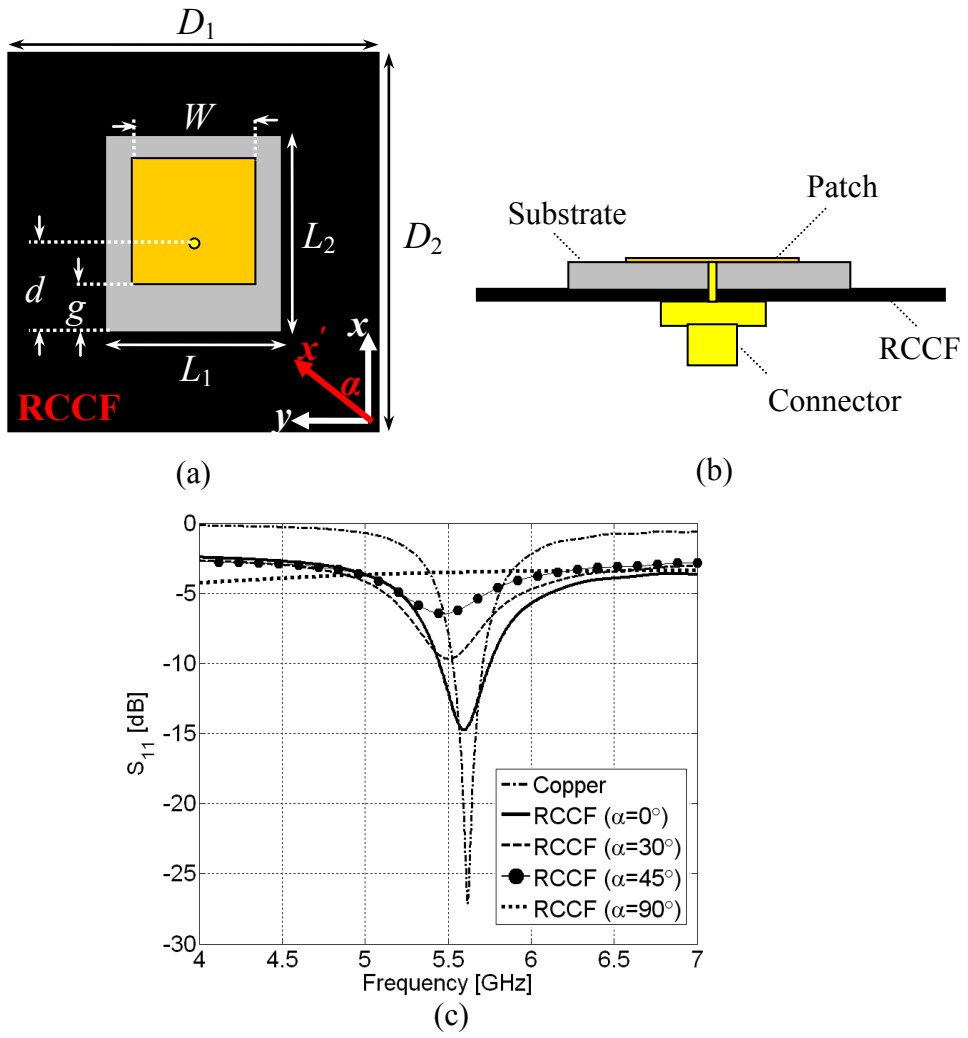

Figure 5.17. Microstrip patch antenna grounded by RCCF, (a) antenna geometry, (b) cross-view, (c) S_{11} of the patch antenna.

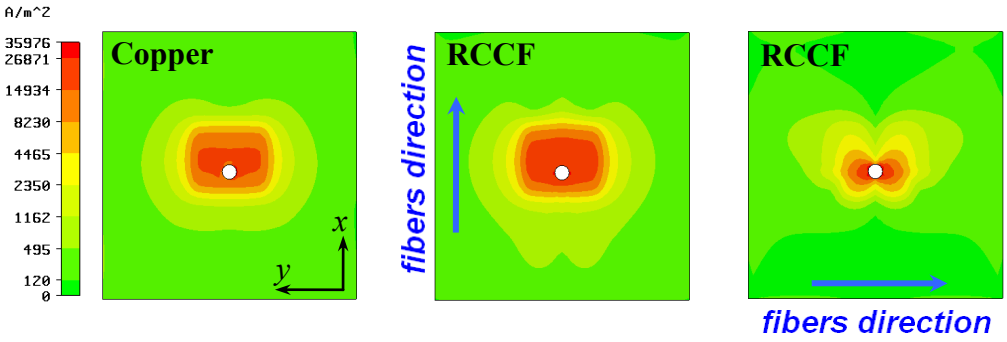

Figure 5.18. Surface current distributions on the ground plane of patch antenna.

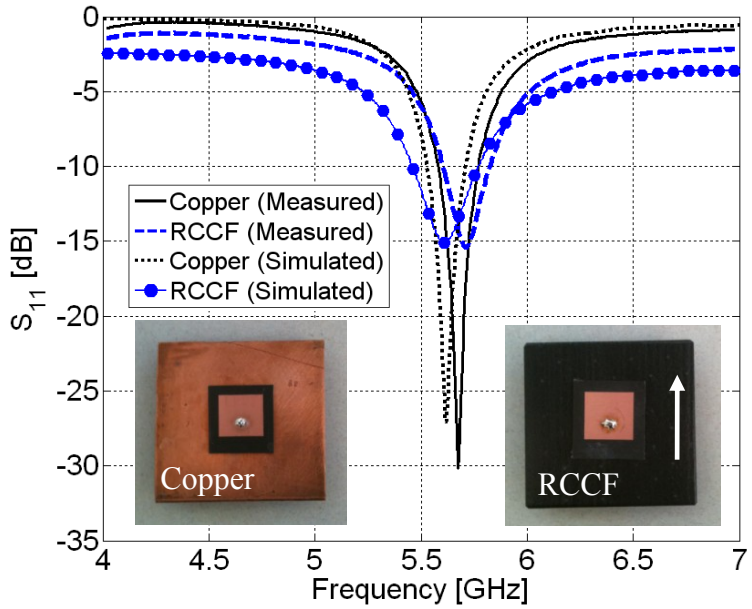

Figure 5.19. Reflection coefficient of the fabricated patch antennas.

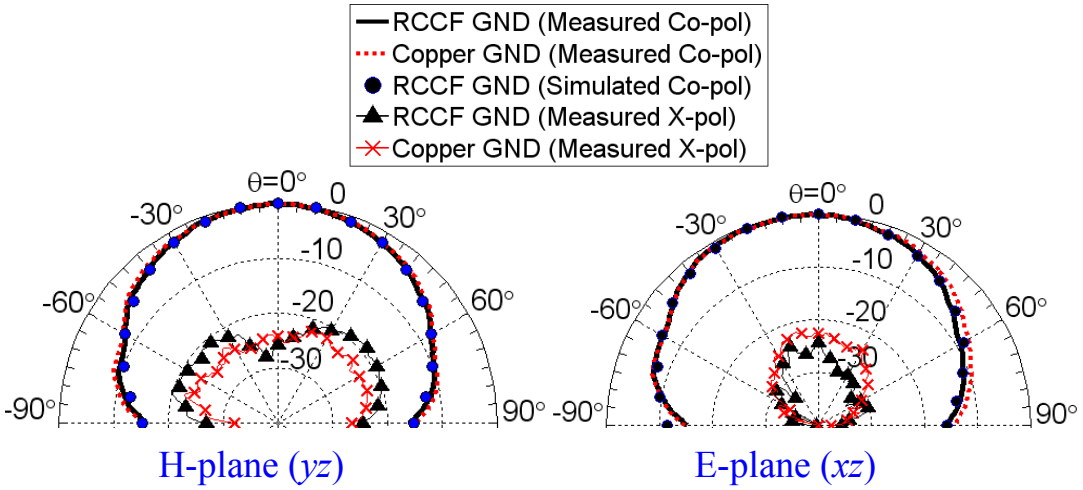

Figure 5.20. Normalized radiation pattern of the patch antenna.

The patch antennas with copper and RCCF ($\alpha = 0^{\circ}$) ground plane were fabricated for measurement. An HP8720 network analyzer was used to measure the reflection coefficient as shown in Figure 5.19. Good agreement is observed between measured and simulated results. It is observed that the -10 dB bandwidth of the composite antenna is higher than that of the copper antenna.

Table 5.4: Peak gain of the patch antenna

Type of Ground Plane	Simulation	Measurement
RCCF ($\alpha = 0^{\circ}$)	5.1 dB	5.8 dB
Copper	8.23 dB	8.58 dB

The normalized radiation pattern in both *H*- and *E*-planes at the frequency of resonance, 5.6 GHz, is shown in Figure 5.20. It is observed that using RCCF composite ground plane instead of the copper ground changes the radiation pattern very little. However, the ohimc loss of RCCF composite reduces the gain and radiation efficiency. The peak gain of the antenna with RCCF ground plane is measured at resonant frequency and reported in Table 5.4. It is observed that the gain drops by about 3dB when RCCF ground plane is used.

5.4 Summary

In this chapter, the use of RCCF composites was investigated for building antennas for different antenna applications, namely RFID, UWB, and WLAN antennas. Metal in the antenna structure was replaced with CFC. The gain of the antenna degrades due to the low conductivity of composites compared to metals. The composite antenna performance was evaluated both numerically and experimentally, and good agreement was found between the simulations and the measurements.

The RCCF composite was used in T-match folded bow-tie RFID antenna. The performance of the patch antenna operating over RCCF ground plane was also investigated. It was observed that when the fibers are oriented in the direction of current flow in the copper ground plane, the RCCF ground plane can support the same current

distribution as the copper ground plane. Generally, the anisotropic conductivity of RCCF composite allows the antenna designer to largely restrict current flow to one direction, and this may lead to novel antenna designs. The RCCF composite material was also used to build a wideband monopole antenna, showing to have suitable properties for an ultra wideband antenna.

Chapter 6 : Carbon Nanotube Composite Materials for Antennas Applications

Due to the favorable mechanical and electrical properties, CNTs have been of interest in nanoelectronics and nanoantenna applications [125]-[134]. Showing high thermal conductivity of about ten times that of copper, CNTs are attractive for high heat-transfer applications in microelectronic circuits [127]. However, CNT dipoles show extremely low efficiency in the order of 10^{-8} for microwave applications [127][128], due to their high resistance per unit length, of about 10 kΩ/μm [127]. Therefore, CNT arrays and composites are proposed to improve the efficiency [135]-[140].

Among CNT composites, SWCNT buckypaper is one of the most highly conductive materials. The high conductivity recommends buckypaper as an attractive replacement for metals in various antenna and microwave applications. In the following, a new fabrication method is proposed to print an arbitrarily-shaped full-composite SWCNT antenna on any type of substrate for various antenna applications such as RFID, multiband wireless, X-band, and mm-wave antennas. The antenna performance is fully investigated by numerical calculation and by measurement.

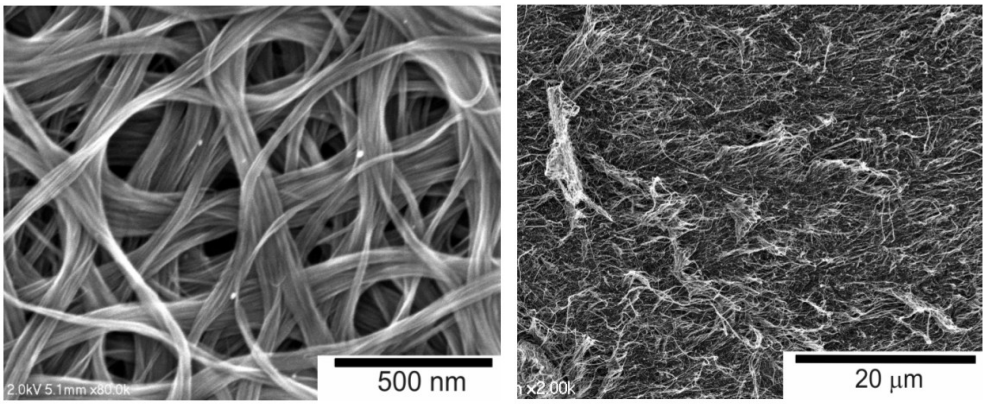

(a) (b)

Figure 6.1. SEM micrographs of the (a) buckypaper and (b) fractured surface of the buckypaper composite [138] .

6.1 SWCNT Buckypaper Material and Method of Composite Antenna Preparation

The thin film made of SWCNTs, called buckypaper, is shown in Figure 6.1. For antenna fabrication, we printed buckypaper on a substrate and then cut out the desired antenna geometry using a high-precision milling machine. The buckypaper is a flexible and soft material that needs to be hardened by resin infiltration in order to be processed on the milling machine. The DC conductivity of the as-prepared buckypapers measured by the van der Pauw method is typically around 70 kS/m. During the infiltration the buckypaper expands, which causes a slight drop in DC conductivity to a typical value of 40 kS/m.

Manufacturing the buckypaper antennas comprises the following three steps as shown in Figure 6.2: buckypaper preparation, plating the substrate with buckypaper impregnated with epoxy resin, and cutting out the antenna. The geometry of antennas is cut out on the substrate using the milling machine shown in Figure 6.3.

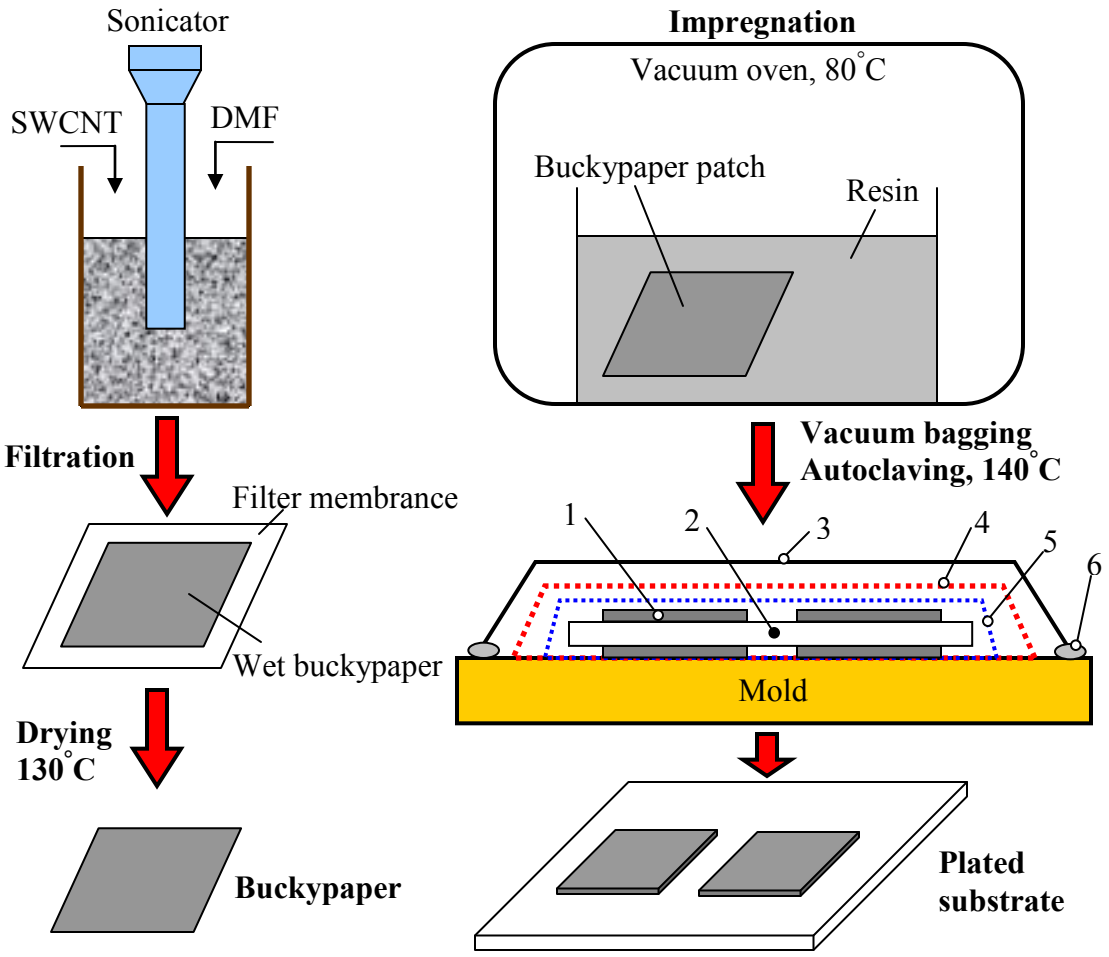

Figure 6.2. (a) Buckypaper preparation, (b) Substrate plating with buckypapers; 1-impregnated buckypaper-patch; 2-substrate; 3-vacuum bag; 4-breather; 5-release film; 6-sealant [140].

The buckypaper composite is produced and printed on the substrate in the CONCOM Laboratory using the method explained in [140]. In the following Sections 6.1.1 and 6.1.2, the detailed method of buckypaper preparation and substrate plating, as provided by Dr. Rosca from CONCOM, is given.

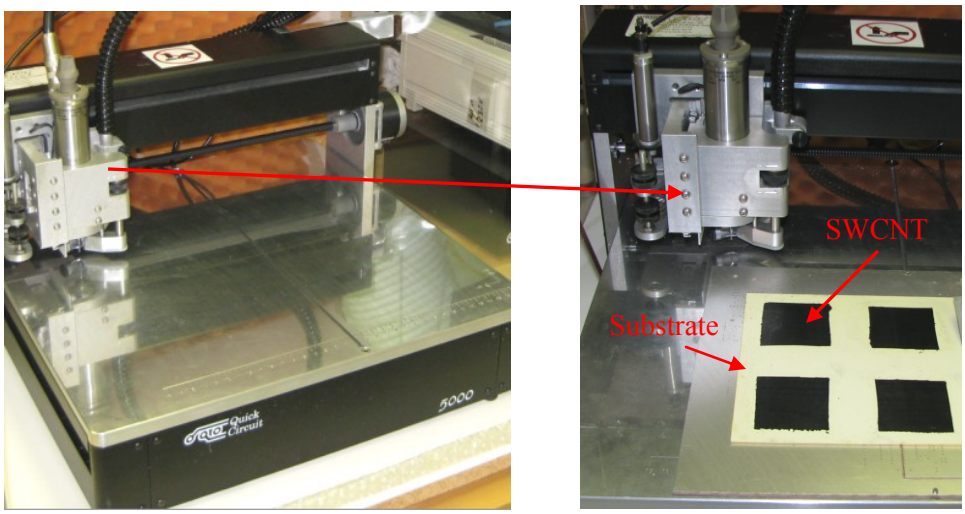

Figure 6.3. Highly precise milling machine to cut out the antenna pattern.

6.1.1 Buckypaper Preparation

The buckypaper preparation is schematically shown in Figure 6.2(a). SWCNTs from Nikkiso Co. (0.5 g) are dispersed in N, N dimethylformamide (DMF) by a horn sonicator (Misonix 3000) at 42W of power for 30 min. Next the SWCNT suspension is filtered on nylon membrane-filter with pore size of 45 micron. After filtration the buckypaper and the membrane are placed between several filter-papers (Whatman no. 1) and lightly pressed between two aluminum plates to absorb the excess solvent. The wet buckypaper is then separated from the filter membrane and dried at 130°C for 12 hours to form a sheet of 140 ×140 mm^2 and 50 μm thickness.

6.1.2 Substrate Plating and Antenna Fabrication

Patches of arbitrary size are cut out from a buckypaper sheet. As shown in Figure 6.2(b), the patches are impregnated with a mixture of epoxy resin (Epon 862) and hardener (26.4 wt% Epikure W, Hexion Specialty Chemicals) in a vacuum oven at 80°C

for 30 min. Next, the impregnated patches were placed on each side of the substrate, vacuum-bagged and cured in an autoclave at 140°C for 4 hours under 40 psi of pressure.

6.2 RFID Tag Antenna Applications

In Section 5.1, we studied the T-match bowtie RFID tag made of RCCF material. It was shown that the antenna performance noticeably depends on the direction of fibers which is the reason for an anisotropic conductivity tensor, and also depends on the conductivity value of composite. However, since CNT composites show isotropic conductivity, the only parameter which matters is the conductivity value. In this section, in addition to the T-match bowtie, we also consider the meander line antenna (MLA) as the RFID tags [138]. By characterizing several fabricated SWCNT composite samples using the coaxial setup, the conductivity in the RFID frequency band is found to be about 25-30 kS/m.

6.2.1 T-match Bowtie Antenna

The geometry of T-match bowtie antenna was introduced in chapter 5. The radiation element is then changed to the SWCNT composite material and the return loss of the RFID antenna tag for different thicknesses of composite material is shown in Figure 6.4. The resonant frequency of the RFID antenna with the composite radiation element is not much different from that with the metal element of Figure 5.1(b). According to (5.1), the gain of the composite antenna can be adjusted by changing either the thickness or the conductivity of the composite material, or both parameters. Table 6.1 and Table 6.2 show the effect of the thickness and the conductivity on the composite antenna's performance,

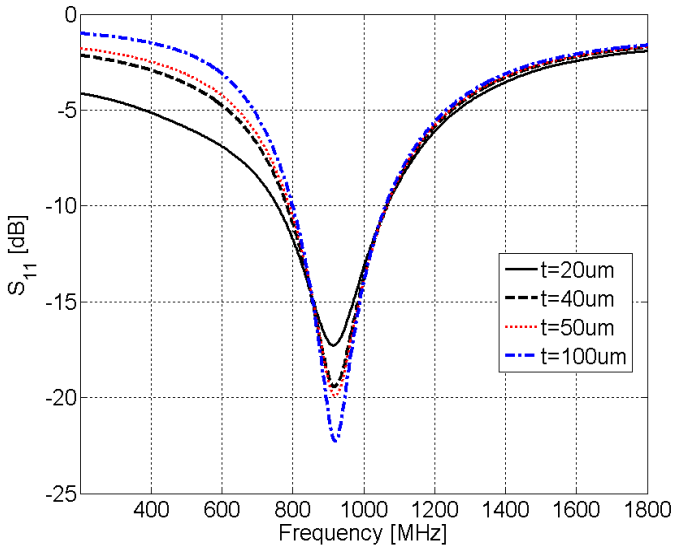

Figure 6.4. Return loss with radiation element made of SWCNT.

Table 6.1: Radiation Efficiency of the Nanotube Composite Antenna

Thickness (μm)	**σ = 10K (S/m)**	**σ = 15K (S/m)**	**σ = 20 K (S/m)**	**σ = 25 K (S/m)**
20	37.83 %	46.94 %	54.25 %	59.35 %
40	55.78 %	62 %	68.57 %	72.34 %
50	59.4 %	67 %	74.3 %	76 %
100	72.42 %	79.15 %	82.8 %	85.2 %

Table 6.2: Peak Gain of the Nanotube Composite Antenna

Thickness (μm)	**σ = 10 K (S/m)**	**σ = 15 K (S/m)**	**σ = 20 K (S/m)**	**σ = 25 K (S/m)**
20	-1.94 dB	-0.61 dB	-0.01 dB	0.37 dB
40	0.005 dB	0.63 dB	0.97 dB	1.19 dB
50	0.37 dB	0.9 dB	0.92 dB	1.4 dB
100	1.2 dB	1.57 dB	1.76 dB	1.88 dB

computed using the CST MWS model. The values can be compared with the copper antenna's gain of 2.4 dB and efficiency of 97%. Note that using the parameters of the characterized sample, t = 40 μm and σ = 25 kS/m, the radiation efficiency and gain are 72.34% and 1.19dB, respectively. Moreover, using (5.2), the maximum read-range (d_{max})

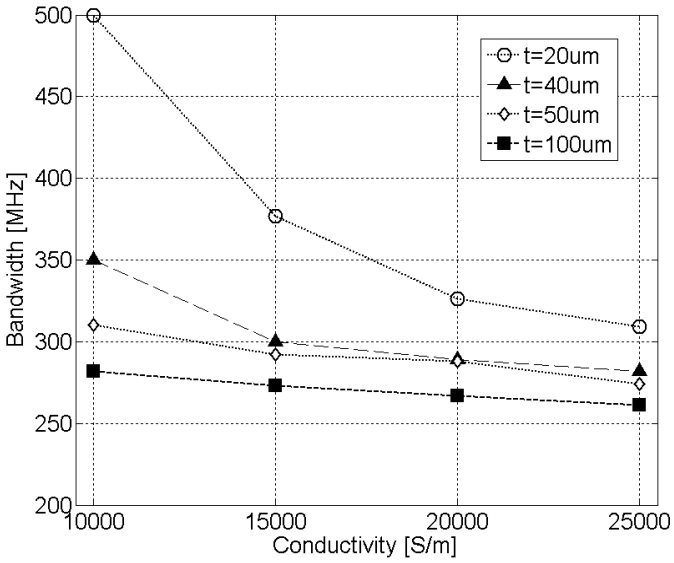

Figure 6.5. The bandwidth of SWCNT antenna versus conductivity.

of the SWCNT composite antenna is found to be 66.54 cm where d_{max} of metal antenna is 76.52 cm.

The tables show that as the conductivity and thickness of the composite increases, both the gain and the efficiency increase to approach the values for the metal antenna of 2.4 dB and 97%. However, as shown in Figure 6.5, the -10dB bandwidth of the antenna is reduced by decreasing the antenna loss. In resonant circuits, as the ohmic loss decreases, the bandwidth decreases and the Q-factor increases, and the composite antenna shows the same behavior. The -10dB bandwidth of the antenna with a metal radiating element is 822 to 1053 MHz, or 231 MHz, which is lower than a composite antenna. For example, the composite antenna with the thicknesses of 20 μm and 40 μm shows a 310 MHz and 270 MHz bandwidth, respectively. It is seen that more flexibility of design is attained by using a composite material instead of metal.

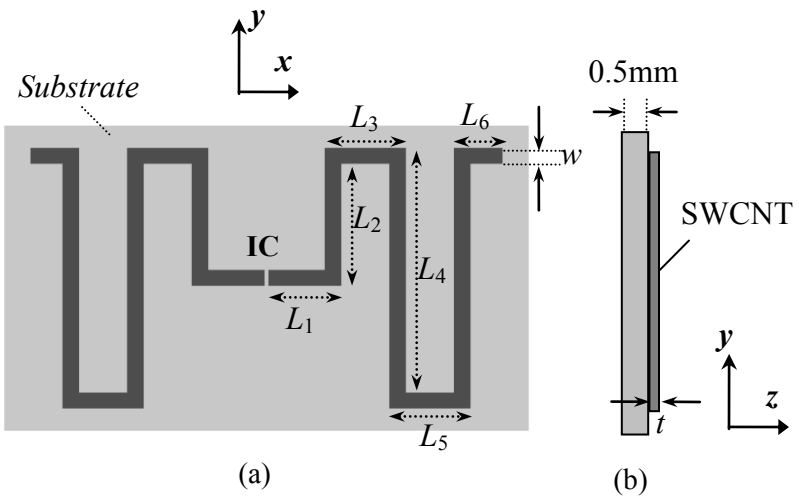

Figure 6.6. (a) MLA structure, (b) Cross-view.

6.2.2 Meander Line Antenna (MLA)

Figure 6.6 shows a meander-line antenna (MLA). Due to its small size and space-filling geometry, the MLA is one of the most desirable antennas for RFID applications [109][141]. In the MLA design, a straight dipole is bent to take less length on the substrate, and this also lowers the resonant frequency. In addition, the radiation resistance is changed, which should be taken into account for matching-circuit design. The planar MLA of Figure 6.6 with dimensions L_1 = 9 mm, L_2 = 15.25 mm, L_3 = 10 mm, L_4 = 30.5 mm, L_5 = 10 mm, L_6 = 6 mm, and w = 2 mm resonates in the RFID lower frequency band around 950 MHz.

The substrate is 0.5mm-thick epoxy with ε_r = 3 and loss tangent tanδ = 0.0013. The gain, radiation resistance and d_{max} of MLA with a copper radiating element are given in Table 6.3. The -10 dB bandwidth of maximum 24 MHz is achieved.

Table 6.4 gives the performance of the MLA when the radiating element is a SWCNT composite, with a width of 2 mm, for various thicknesses of the SWCNT material. It is

Table 6.3: MLA Performance with a Copper Radiating Element (t =40 μm)

w (mm)	f_o (MHz)	η (%)	Gain (dB)	R_r (Ω)	d_{max} (cm)
1	873	96.71	1.84	12.51	75.57
2	914	97.94	1.86	14.82	72.35
3	959	98.22	1.87	15.3	69

Table 6.4: MLA Performance with an SWCNT Radiating Element (w=2mm)

Thickness (μm)	f_0 (MHz)	η(%)	Gain (dB)	R_r(Ω)	BW (MHz)	d_{max}(cm)
30	966.5	15.24	-6.21	106	239	27
40	954.6	18.7	-5.32	81.5	162	30.3
50	950.4	22	-4.6	67.61	149.3	33
100	976.35	37.12	-2.35	43.58	93	42

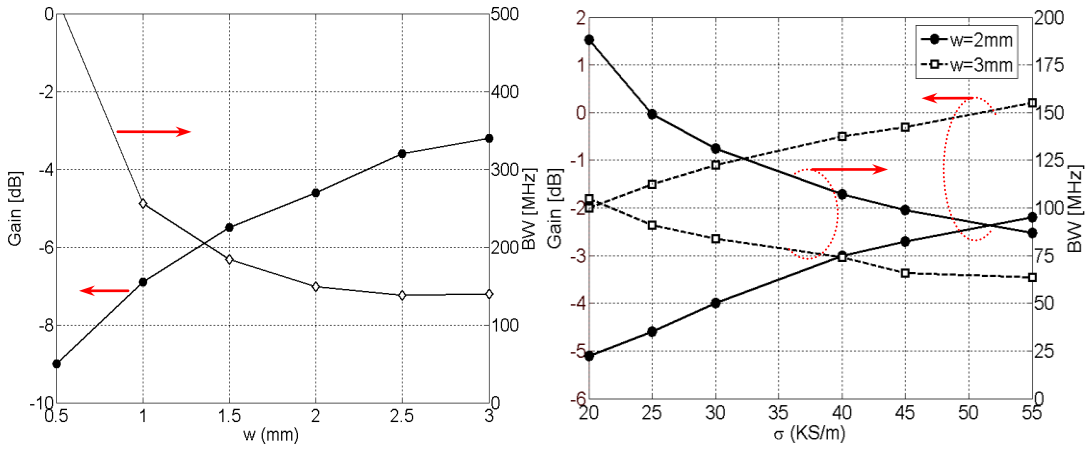

Figure 6.7. Gain-bandwidth diagram of SWCNT MLA versus (a) w (σ = 25 kS/m, t = 50μm), (b) σ (t = 100μm).

observed that the bandwidth for a 30 μm thickness is much wider than the bandwidth of 24 MHz of the metal antenna. The bandwidth decreases with increasing thickness of the composite as the resistance per unit length of the arms of the antenna decreases. However, the gain is low compared to the metal antenna. The input impedance of the MLA is quite different from the RFID IC's impedance of 380 ohms, needing a matching circuit between antenna and IC. The 30 μ m composite antenna has a resistance of 106

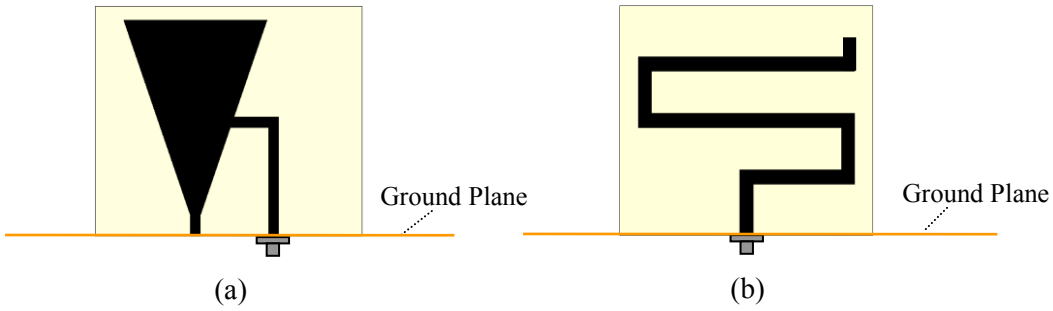

Figure 6.8. Monopole configuration of SWCNT composite antennas, (a) T-match bow-tie, and (b) MLA.

ohms, much closer to the IC's 380 ohms than the resistance of the metal antenna of 12 to 15 ohms, hence the matching circuit could be simplified. The input impedance can also be adjusted by using composites with different values of conductivity, to get closer to 380 ohms. Therefore composites provide more flexibility in the design. The center frequency of resonance for nanotube antenna can be adjusted by tuning the length of the MLA.

The ohmic loss of a nanotube MLA can be controlled by the width of the line (w) and the conductivity (σ) of composite, as well as the thickness of line. The effect of w and σ on the gain and bandwidth of MLA is shown in Figure 6.7. The gain could be improved considerably by using thicker and wider MLA. However, it can be seen that one may compromise between the gain and bandwidth.

6.2.3 Experimental Results

We fabricated the monopole configuration of the SWCNT dipole bow-tie and MLA antennas as shown in Figure 6.8. The monopole composite antenna mounted on a ground plane is fed through a 50-ohm SMA connector from the bottom. The size of ground plane for the bow-tie antenna is 120mm × 160mm, and for the MLA antenna is 100 mm × 100 mm. The composite material thickness is 40 μm. The dimensions of the bow-tie are as

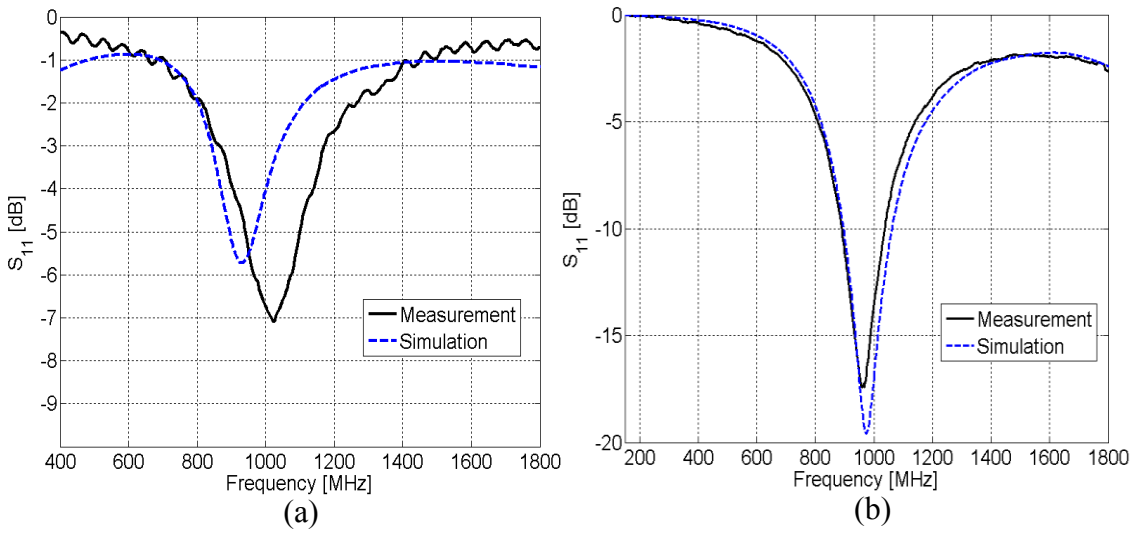

Figure 6.9. Return loss of SWCNT composite antenna, (a) T-match bow-tie, and (b) MLA.

reported in Figure 5.1(a). The MLA parameters are L_1 = 8.5 mm, L_2 = 15 mm, L_3 = 10 mm, L_4 = 30.2 mm, L_5 = 10 mm, and L_6 = 3 mm, and w = 2 mm. Using the HP8720 network analyzer, the return loss of composite antennas is measured as shown in Figure 6.9. Satisfactory agreement is seen between the CST MWS simulation and the measurement. The small shift of measured resonance frequency can be explained by material and manufacturing tolerance.

6.3 Multiband Wireless Applications

There are many types of antennas for different applications, namely radio/TV broadcasting, cell phones, global positioning system (GPS), medical and microwave imaging, RFID, Bluetooth, WLAN, UWB systems, satellite communication, radar systems, millimeter wave applications, wireless personal area network (WPAN) and military applications. Depending on the application, the appropriate antenna should be designed since in each application the specific characteristics are needed to be satisfied

by the antenna. One of the key factors in choosing the type and shape of the antenna is frequency. The whole frequency band, from DC to up to hundreds of gigahertz, has been divided up for many sub-bands allocated to different applications. It would be very demanding if one could design the antenna to cover more than one frequency band making to the multifunctional behavior of antenna. By doing so, one antenna could be used for different applications without changing its geometry. This kind of antenna is called as multiband antenna. One can design a wideband antenna to cover many frequency bands, but when the interference with other communication systems operating at undesirable frequencies is an issue, the multiband antenna is of much more interest compared to the wideband one.

Recently WLANs and the worldwide-interoperability-for-microwave-access (WiMAX) technology have been extensively used in commercial, medical and industrial applications. The allocated spectrum for these WLAN systems is centered at 2.4, 5.2 and 5.8 GHz and for WiMAX at 3.5 GHz. There are many reported antenna designs for wireless systems, whether single-band or multiband antennas [142]-[145]. One of the best known geometries which make one able to have multiband performance is fractal structures [146]-[149]. By using fractal geometry, getting an advantage from the self-similarity characterization of fractal shapes inside the structure, one can cover different frequency bands.

In this section, we explore the use of SWCNT material for multiband wireless applications [140]. As shown in Figure 6.10(a)-(b), a modified Sierpinski fractal antenna, operating at UHF-RFID/Bluetooth/WLAN, is designed and considered for study. The antenna is fed through a 50-ohm microstrip line. Compared to the traditional Sierpinski

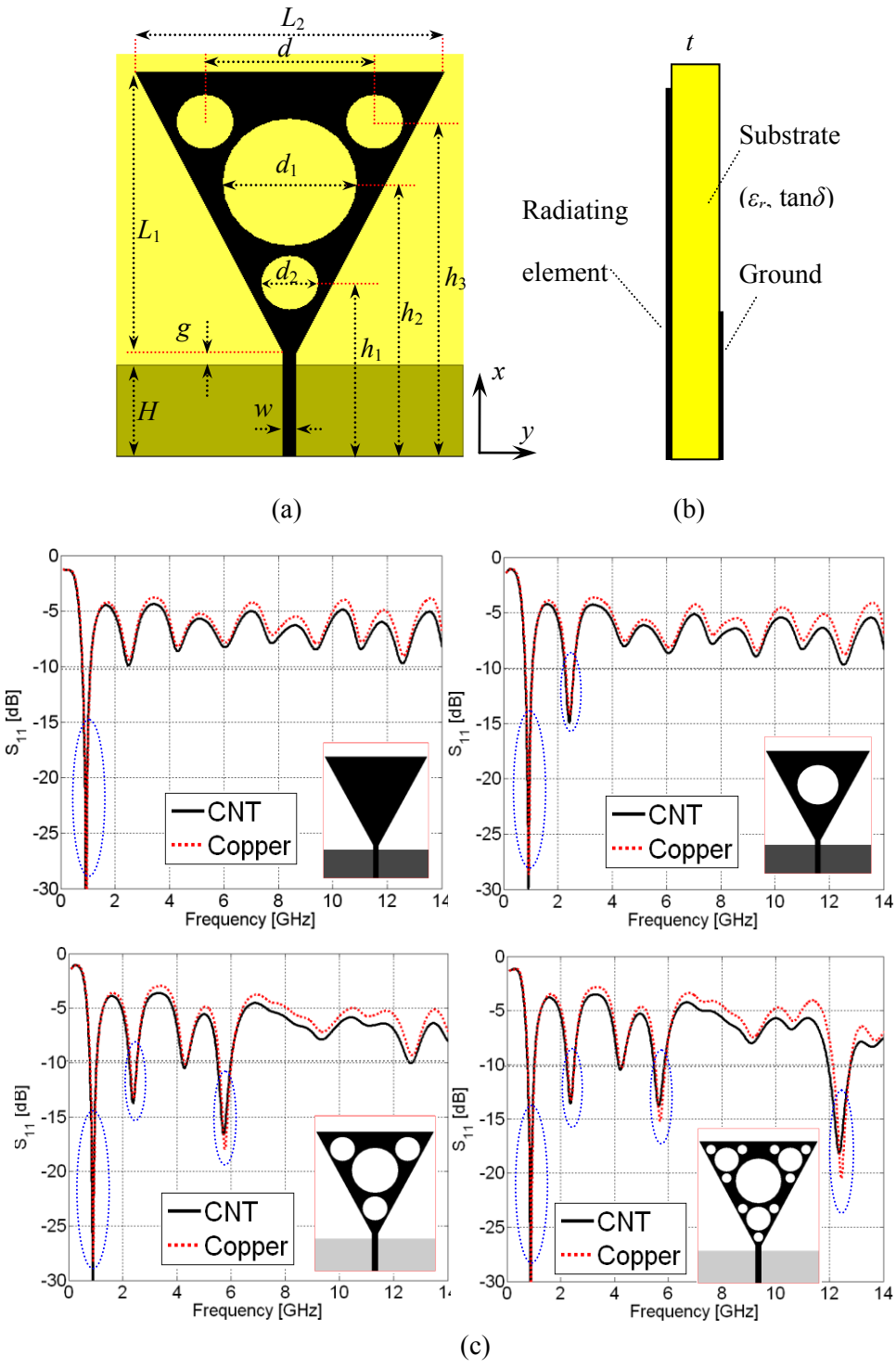

Figure 6.10. (a) Tri-band Sierpinski gasket antenna with circle generation. (b) side view, (c) simulated reflection coefficient (S_{11}) .

gasket, we consider circle generation instead of triangle generation, making the design simpler. The antenna dimensions can be adjusted regarding the desired resonant frequencies and the substrate dielectric constant. For example, using $\varepsilon_r = 3$, $t = 1.5$ mm, $L_1 = 64.7$ mm, $L_2 = 72$ mm, $d = 38.87$ mm, $d_1 = 28$ mm, $d_2 = 15$ mm, $h_1 = 40$ mm, $h_2 = 63.52$ mm, $h_3 = 76.74$ mm, $g = 3.3$ mm, $H = 20$ mm, and $w = 3.5$ mm, the simulated reflection coefficient of the antenna is shown in Figure 6.10(c). The antenna provides reasonable impedance matching at 900 MHz for UHF-RFID, at 2.4 GHz for Bluetooth, and at 5.8 GHz for WLAN. A fourth pass band can be added using the small circular slots shown at right in part c of the figure, of diameter of 6 mm. A slight difference is observed between reflection coefficient of CNT and copper antennas.

For the sake of brevity, we only consider the tri-band case for an experimental study. The composite antenna is fabricated on a 96mm × 72mm epoxy glass (G10/FR4) substrate ($\varepsilon_r = 4.9$, $\tan\delta = 0.025$) as shown in Figure 6.11(a). It should be noted that the SWCNT composite is printed on both sides of the substrate to make a full-composite antenna. The geometrical parameters are $t = 1.5$, $L_1 = 61.4$, $L_2 = 64$, $d = 35.2$, $d_1 = 28$, $d_2 = 12$, $h_1 = 38$, $h_2 = 60$, $h_3 = 73.2$, $g = 2.6$, $H = 20$, and $w = 2.6$ mm. Using the HP8720, the reflection coefficient of the composite antenna is measured as displayed in Figure 6.11(b). In addition to the resonances over the desired frequency bands, matching is also observed around 4.2 GHz which is due to a higher order mode of the main gasket, the third mode.

The simulated peak gain of the composite antenna is compared with the copper one in Table 6.5. As expected, the gain using composite is lower than that using copper.

The normalized radiation pattern of the CNT antennas in both *E*-(*xz*-) and *H*-(*yz*-)

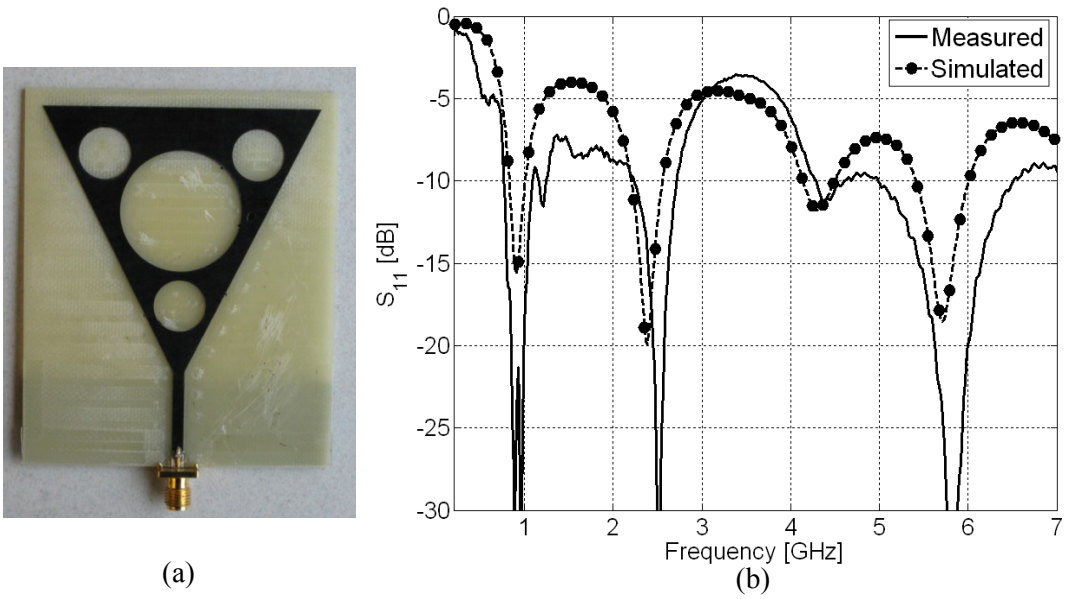

(a) (b)

Figure 6.11. (a) Prototype of the fabricated antenna, (b) S_{11} of the antenna.

Table 6.5: Simulated Peak Gain of the Tri-Band Fractal Antenna

***f* (GHz)**	**Copper antenna gain**	**Composite antenna gain**
0.91	1.42 dB	0.96 dB
2.44	4.69 dB	4.1 dB
5.7	5.7 dB	4.44 dB

planes were measured in an anechoic chamber as shown in Figure 6.12. For the sake of brevity, only the normalized radiation patterns at 2.4 and 5.8 GHz are reported. There is good agreement between simulation and measurements. The CNT antenna shows a low cross-polarized field. Not reported here, the radiation pattern over UHF-RFID band is quite omnidirectional in the *H*-plane and donut shaped in the *E*-plane.

The actual measured peak gain of the CNT antenna at 2.4 and 5.8 GHz is compared with that of the copper antenna in Figure 6.13. As expected, due to the lower conductivity, the gain of the composite antenna is lower than the copper one. The difference is at most 1 dB over the Bluetooth frequency band and 2 dB over the WLAN bands.

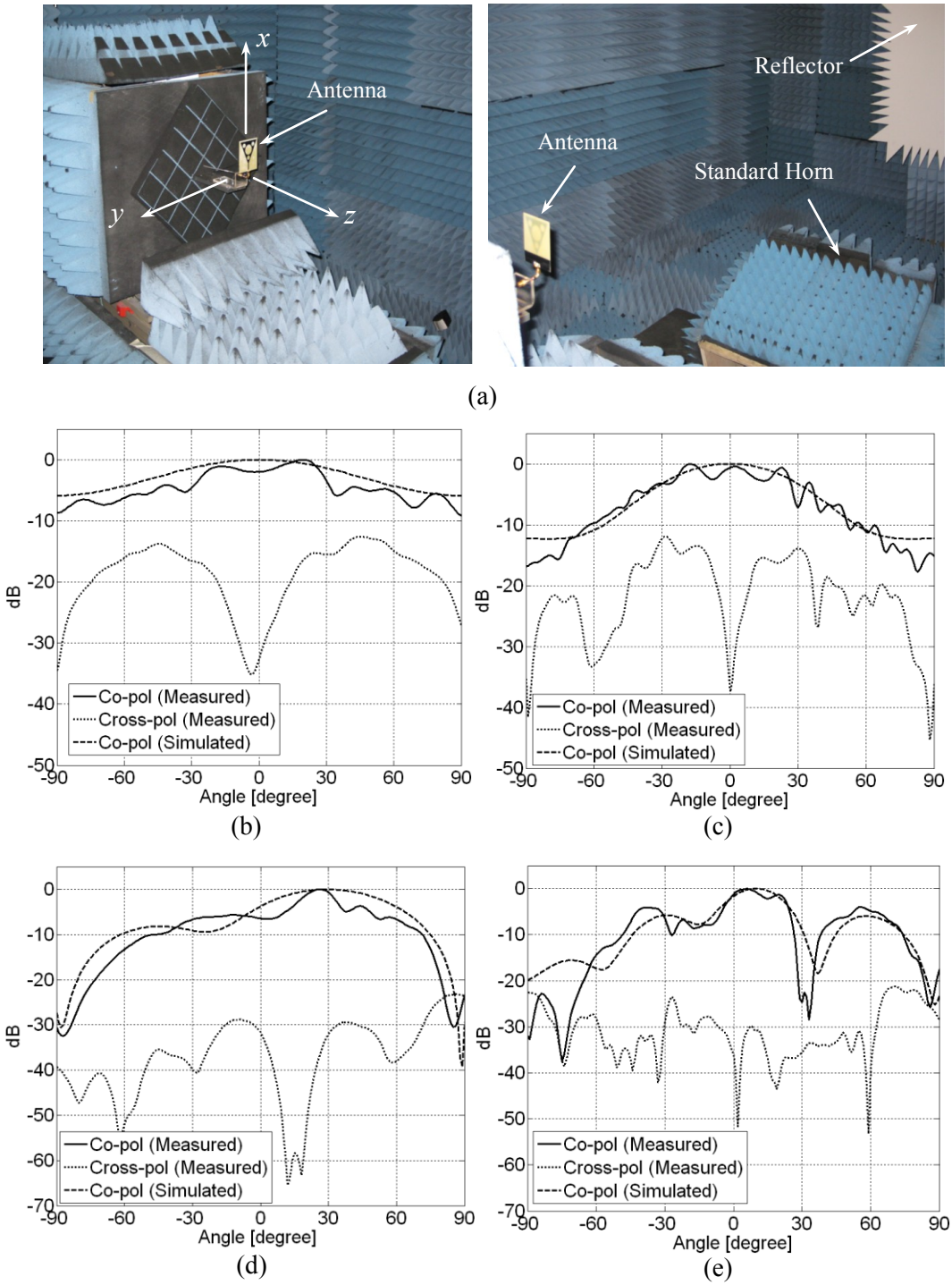

Figure 6.12. Normalized radiation pattern of CNT antenna, (a) antenna in anechoic chamber, (b) H-plane at 2.4 GHz. (c) H-plane at 5.8 GHz, (d) E-plane at 2.4 GHz, (e) E-plane at 5.8 GHz.

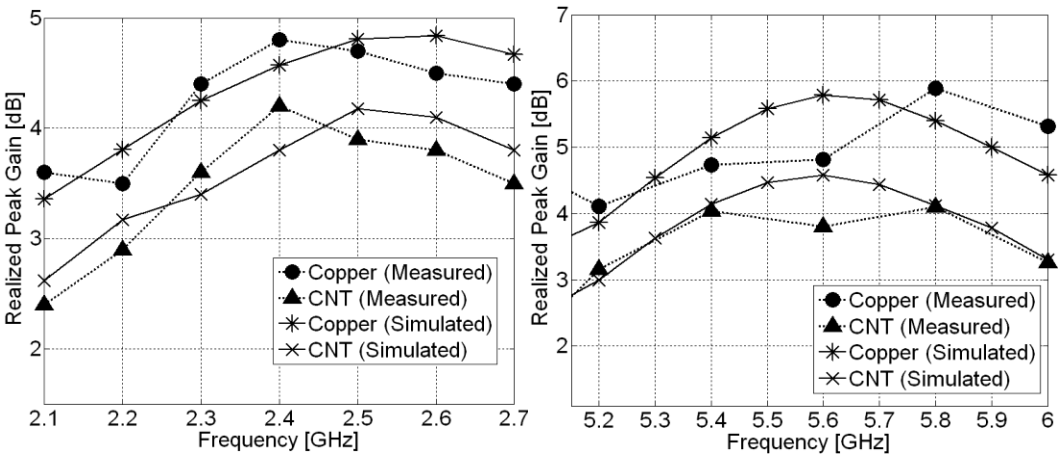

Figure 6.13. Realized peak gain of the fractal antenna at (a) 2.4 GHz, (b) 5.8 GHz.

It should be noted that the loss associated with the length of the microstrip line (*H*) can affect the antenna efficiency and gain. We found that the CNT microstrip line shows about 0.17 dB/cm and 0.22 dB/cm loss at 2.4 and 5.8 GHz frequency ranges, respectively. Therefore, the gain of the CNT antenna can be easily controlled by adjusting the microstrip line length, *H*.

6.4 X-band Antenna Applications

X-band is a part of microwave frequency spectrum which has been used for many applications such as satellite communication, radar, airborne imaging, and military systems [150][153]. X-band phased array antennas are commonly used in aircraft for radar, surveillance, and reconnaissance applications. In this section, a full composite X-band antenna is fabricated and its performance is well compared with a copper antenna [154]. The square ring slot antenna [155] is chosen for study as shown in Figure 6.14. The antenna is excited by a coaxial cable from underneath. The inner conductor of SMA coaxial connector is connected to the radiating element located at the top of substrate

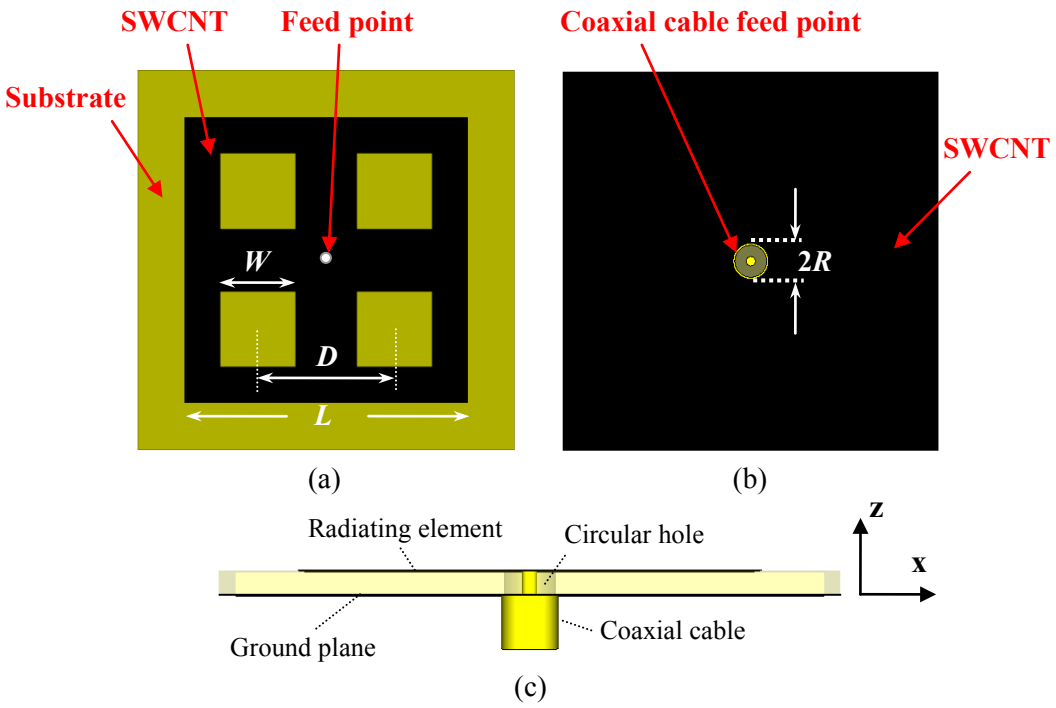

Figure 6.14. Square ring slot antenna, (a) Top view, (b) back view, and (c) side view.

Table 6.6: Gain and radiation efficiency (η) of the square ring slot antenna at resonance frequency

Type of Antenna	*Gain* [dB]	η [%]
Full-SWCNT	5.97	68.27
Copper	7.68	98.63

through a hole in the substrate as displayed in Figure 6.14(c). The substrate is 1.5mm-thick G10/FR4. The geometrical parameters are as follows: W = 8 mm, D = 14.5 mm, R = 1.9 mm. The substrate size is 40×40 mm^2. The antenna is composed of SWCNT composite as a replacement of copper.

The antenna is design to operate over X-band frequencies, resonating at 11 GHz. The gains and radiation efficiencies of the antennas at 11 GHz are reported in Table 6.6. It is observed that due to the lower conductivity, the composite antennas have lower gain

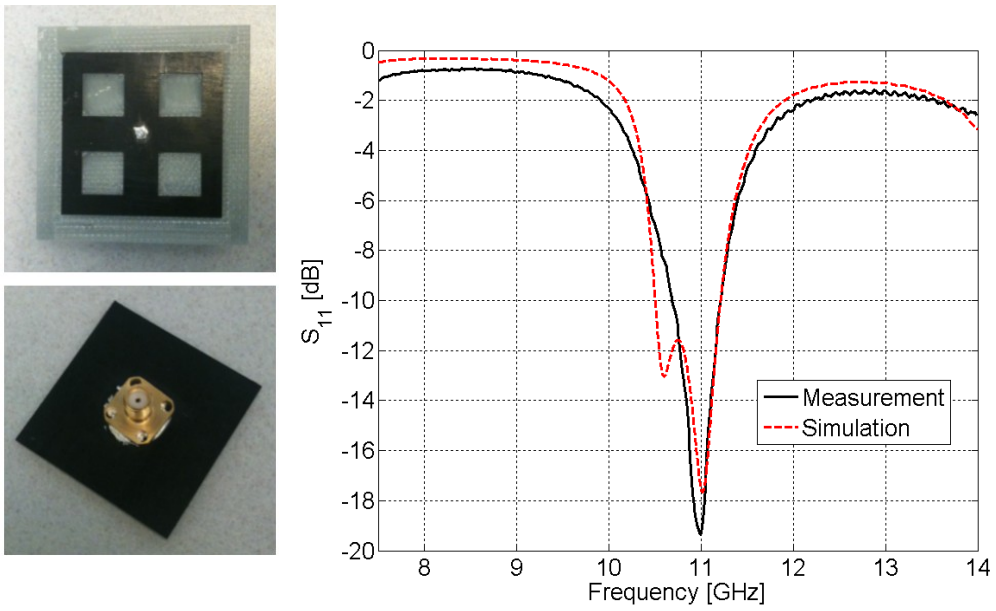

(a) (b)

Figure 6.15. (a) The prototype of the full composite square ring slot antenna, (b) S_{11} of the antenna.

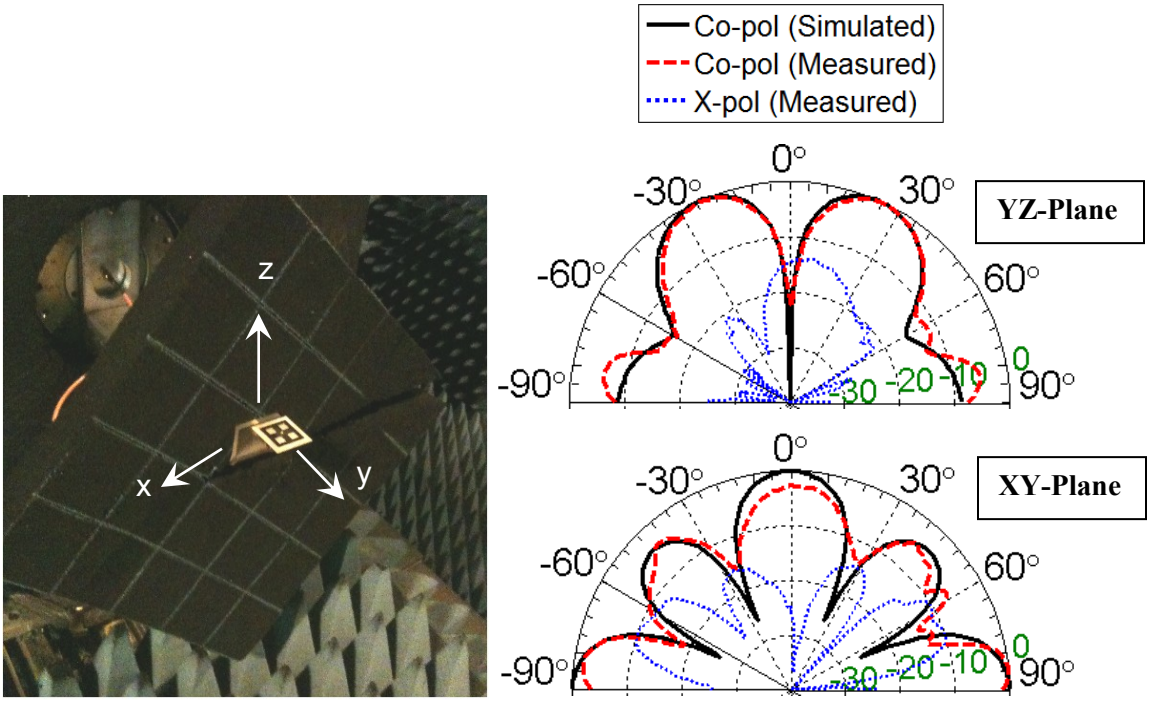

Figure 6.16. Normalized radiation pattern at YZ and XY-planes.

compared to the copper one.

The composite antenna is fabricated as shown in Figure 6.15(a). Using the HP8720, the reflection coefficient is measured as reported in Figure 6.15(b). The normalized radiation pattern is measured in anechoic chamber at both *E*- and *H*-planes. Good agreement is observed between measurement and simulation results.

6.5 Millimeter Wave (mm-wave) Antenna Applications

Due to the high data transmission rate, millimeter-wave (mm-wave) communication systems are increasingly used in many commercial and military applications, such as imaging systems, automotive radars, medicine, high resolution radars and mobile communication systems [156]-[159]. In mobile and military applications where the antenna may be used in harsh environments, replacing metal with a more suitable material increases the system reliability.

In this section, we explore the use of SWCNT material for wideband mm-wave antennas [160]. A low-profile wideband microstrip-fed monopole antenna operating over 24 to 34 GHz is designed and investigated by measurement and by numerical simulation. Then, a two-element array with a matched T-junction feed network is realized and the performance of the CNT antenna is compared with a copper one. Since in reality it is likely that the antenna will be close to other devices or be integrated with different components in the circuit, the housing effect on the copper and CNT antennas performance is investigated.

To develop a model of the composite material for use in computer simulations of mm-wave antennas, we use a standard Ka-band rectangular waveguide with cross-section

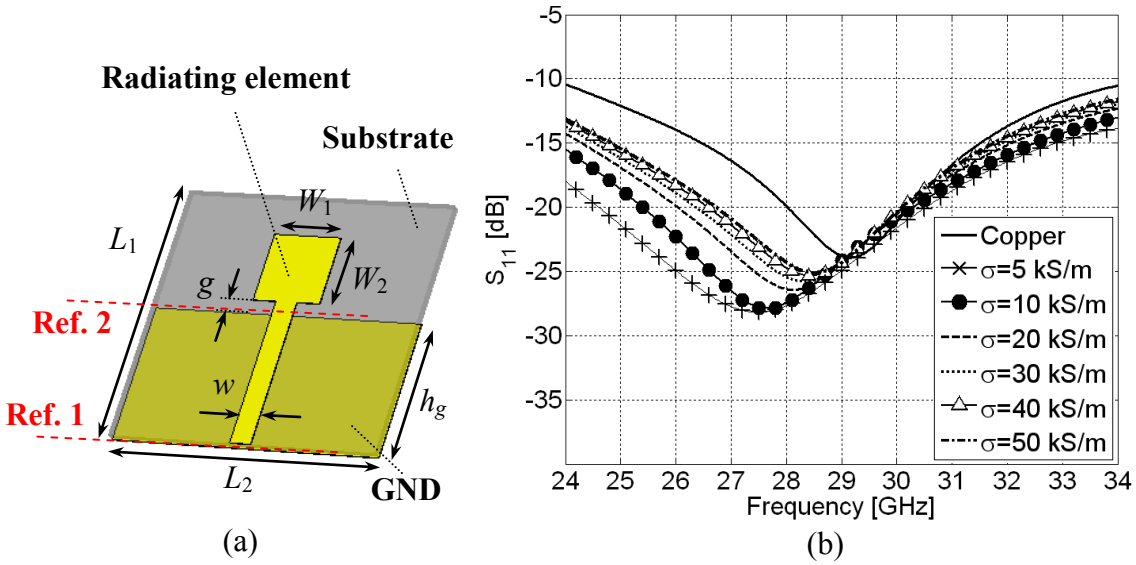

Figure 6.17. (a) The geometry of mm-wave monopole antenna, (b) simulated S_{11} versus conductivity.

Table 6.7: Radiation efficiency of the monopole antenna at Ref. Plane 2

Conductivity (S/m)	24	28	32	34
5×10^3	80.41	82.45	73.11	68.98
1×10^4	84.42	85.9	81.13	76.42
2×10^4	87.76	89.19	84.49	80.54
3×10^4	89.33	90.81	86.69	83.11
4×10^4	90.35	91.88	88.4	84.77
5×10^4	91.1	92.63	89.53	85.98
Copper (5.8×10^7)	97.74	99.2	98.8	97.11
PEC ($\sigma \rightarrow \infty$)	98.01	99.51	99.02	97.47

dimension of 7.11 × 3.55 mm^2 for characterization. The thickness of the composite is 0.2 mm. The sample used to build the antennas has effective relative permittivity ε_r = 5.5 and conductivity σ =10 kS/m, over the desired frequency range.

6.5.1 Single Element Antenna and Measurements

Figure 6.17(a) shows the EM model of monopole antenna developed in CST MWS. The antenna is fed through a 50-ohm microstrip line. The antenna geometrical parameters

are $L_1 = L_2 = 14$ mm, $W_1 = 3.5$ mm, $W_2 = 3.75$ mm, $g = 0.5$ mm, $h_g = 7.5$ mm, and $w = 1.1$ mm. The substrate is Rogers 4350 with a thickness of 0.508 mm, $\varepsilon_r = 3.48$, and $\tan\delta = 0.0037$.

The impedance bandwidth of a monopole antenna for copper and composites with various conductivities is shown in Figure 6.17(b). In the composite antenna both the radiating element and ground plane are made of CNT. It is observed that the bandwidth of the composite antenna is higher than that of the copper antenna operating over the 24 to 34 GHz frequency range. In fact, as the ohmic loss decreases, the bandwidth decreases and the Q-factor increases, and the composite antenna shows this behavior.

Due to the lower conductivity, the gain and radiation efficiency (η) of composite antennas are lower than that of the copper antennas. The radiation efficiency is defined as

$$\eta = \frac{P_{rad}}{P_{rad} + P_{loss}} \tag{6.1}$$

where P_{rad} and P_{loss} are the radiated power and the ohmic losses. The overall ohmic loss is the sum of the power loss in the microstrip feed line plus the power loss in the antenna itself. The antenna efficiency in (6.1) excludes the loss of the feed line, and is calculated at the input of the antenna, reference plane 2. Table 6.7 shows the effect of the conductivity on the composite antenna's radiation efficiency at four different frequencies, 24, 28, 32 and 34 GHz. Note that using the parameters of the sample described in Section II, σ = 10 kS/m, the values can be compared with the copper antenna's peak gain and radiation efficiency.

Figure 6.18 shows the radiation efficiency of the copper and CNT antennas, at both reference planes 1 and 2, over the whole frequency range of interest. The curves labeled

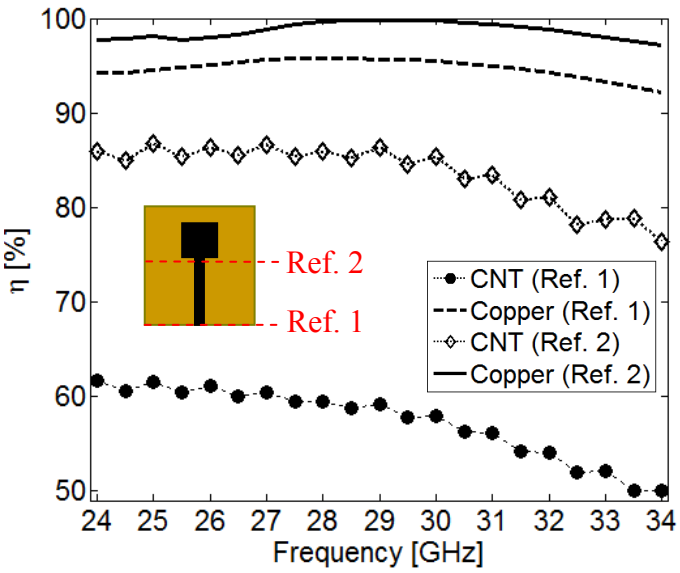

Figure 6.18. The radiation efficiency of the copper and CNT (σ = 10 kS/m) monopole antennas.

Ref. 2 give the radiation efficiency of the antenna alone. The curves labeled Ref. 1 give the efficiency of the system made up of the lossy feed line and the antenna, much lower than that of the antenna alone. The lossy feed line behaves as an attenuator, giving control over the amount of power reaching the antenna itself.

The copper and CNT monopole antennas are fabricated as shown in Figure 6.19(a). The composite antenna is fabricated using the method described in section 6.1. The antennas are fed by solder-free 2.92mm Southwest Microwave connectors [161]. Using an Agilent-E8364B network analyzer, the reflection coefficient of each antenna is measured and shown in Figure 6.19(c) and (d). The connector is included in the simulation model in CST-MWS to better simulate the measurement setup.

The radiation pattern of both the copper and the CNT antennas in both *E*-(*yz*-) and *H*-(*xz*-) planes were measured in an anechoic chamber. The normalized radiation pattern at

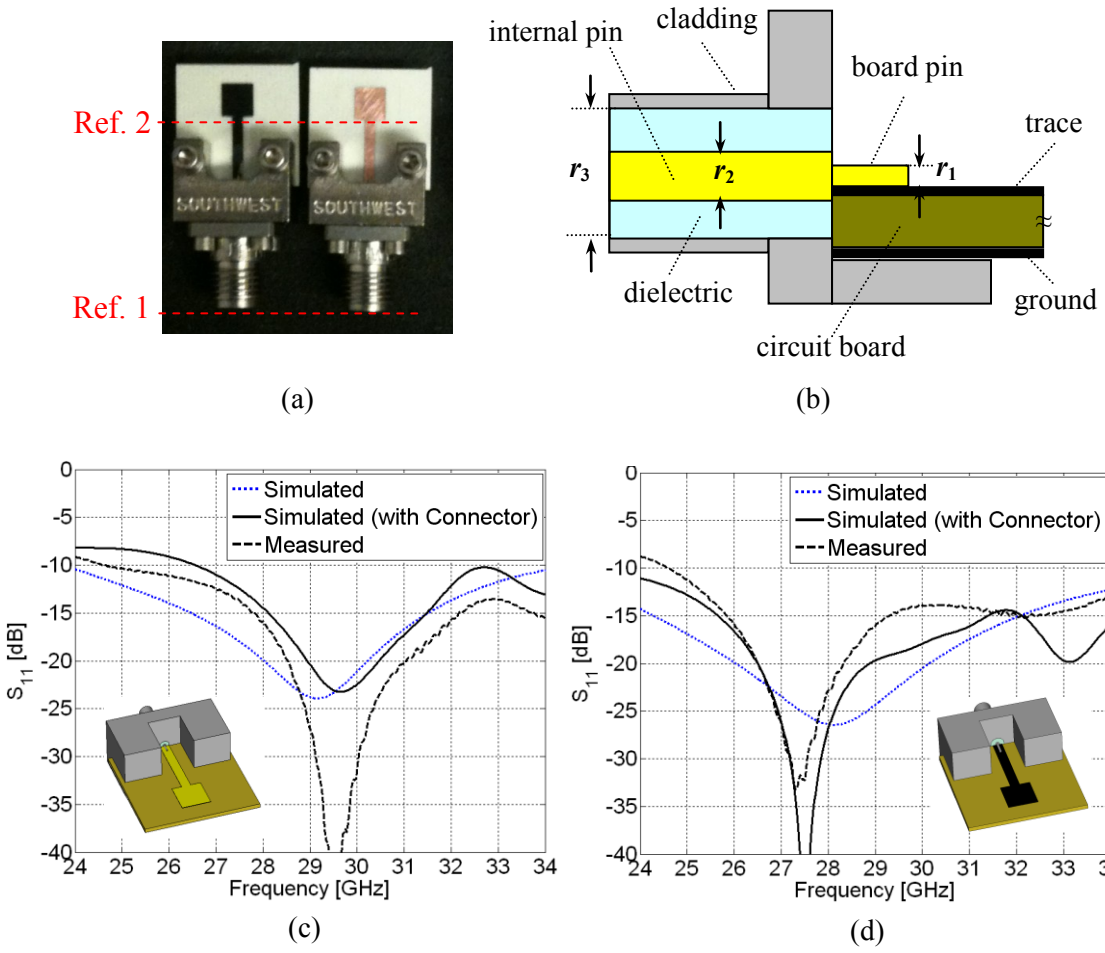

Figure 6.19. (a) Fabricated copper and CNT monopole antennas, (b) connector model (r_1 =0.18, r_2=0.38, r_3= 1.22 mm), (c) S_{11} of copper antenna, (d) S_{11} of CNT antenna.

26.5, 29, and 33.5 GHz are reported in Figure 6.20. It is observed that CNT antenna shows a stable radiation pattern over the frequency range of interest. The radiation pattern is found to be almost omnidirectional in the *H*-plane, which is of most interest for wireless communication systems.

It should be noted that the loss associated with the length of the microstrip line can play an important role on the antenna efficiency. The scattering parameters of a 2 cm CNT microstrip line were measured and are shown in Figure 6.21. After excluding the

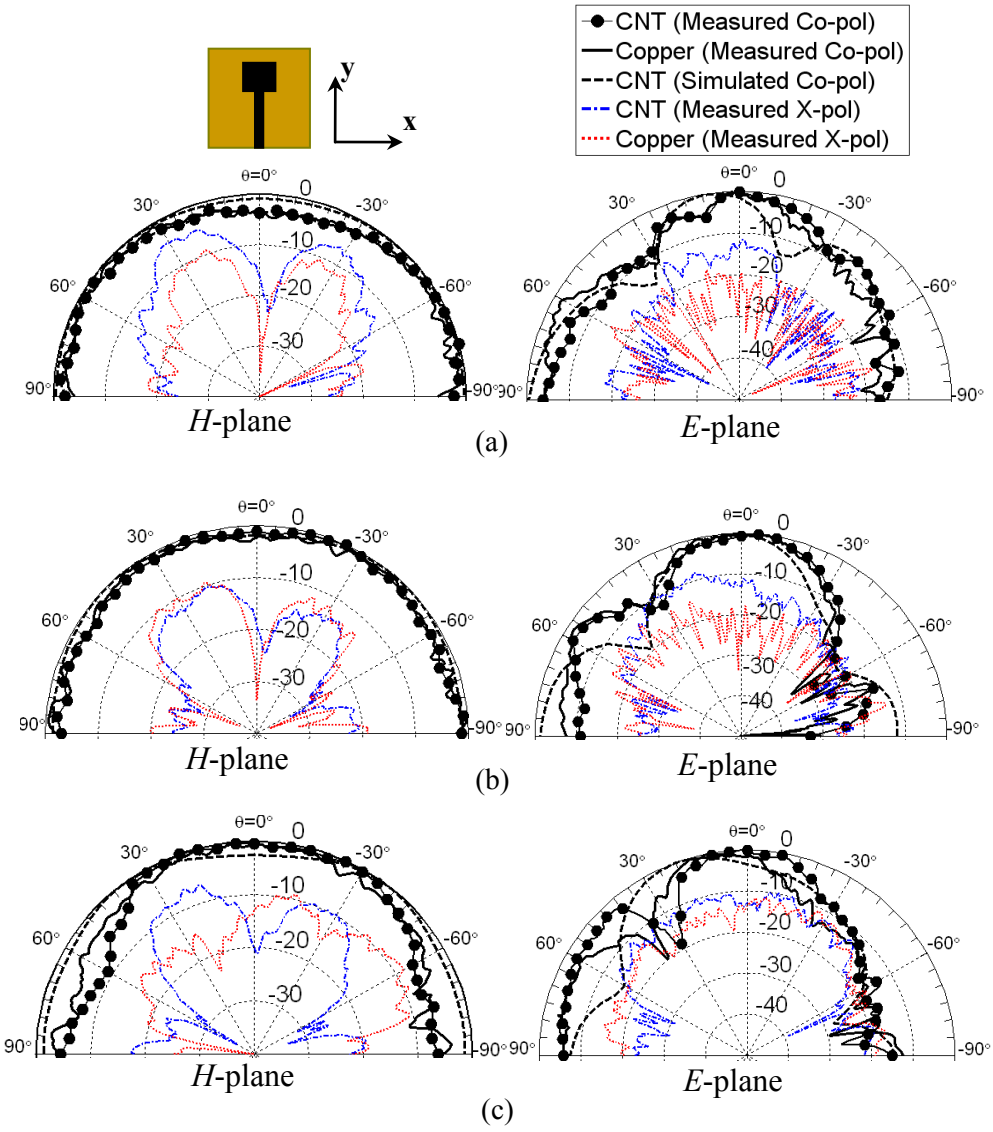

Figure 6.20. Normalized radiation pattern of monopole antenna at: (a) 26.5 GHz, (b) 29 GHz, (c) 33.5 GHz.

loss of two connectors (~1.3 dB in total), we found that the CNT microstrip line shows about 2.6 dB/cm loss over the 24 to 34 GHz frequency range. The loss of copper microstrip line is about 0.35dB/cm. The simulation results show that by changing h_g, for example, from 4.5 to 10.5mm, the peak gain of CNT antenna varies from 2.24 to 0.94 dB

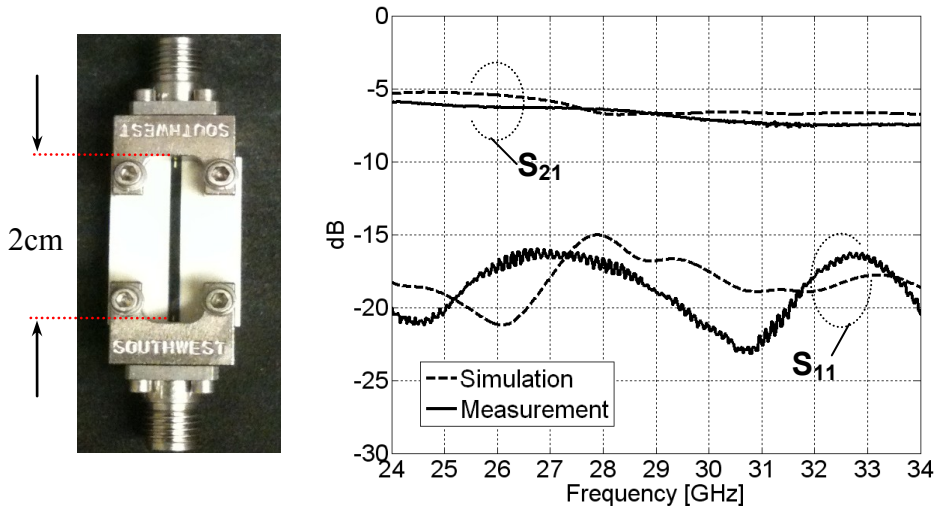

(a) (b)

Figure 6.21. (a) Prototype of CNT microstrip line, (b) S_{11} and S_{21} parameters.

(1.3 dB), where for copper antenna it varies from 3.8 to 3.52 dB (0.28 dB). Therefore, the gain of the CNT antenna can be easily controlled by slightly adjusting the length of microstrip line.

The realized gain at boresight angle ($\theta = 0^{\circ}$, $\varphi = 90^{\circ}$) in reference plane 1, at the connector in Figure 6.19(a), is shown in Figure 6.22(a). By excluding the loss of the connector and the microstrip line, the measured antenna gain at reference plane 2, at the input to the radiating element, is shown in Figure 6.22(b). As expected, it is observed that the average gain of the CNT antenna is lower than the copper one, which is due to the lower conductivity of the composite material.

The transfer function of the antenna is measured by making Tx/Rx setups of two identical antennas at a separation distance of R. Figure 6.23 shows the transfer function of CNT and copper antennas for both face-to-face and side-by-side configurations. The fairly constant group delay of Figure 6.23 shows that the CNT antenna has low dispersion, indicating that it is useful for UWB radios.

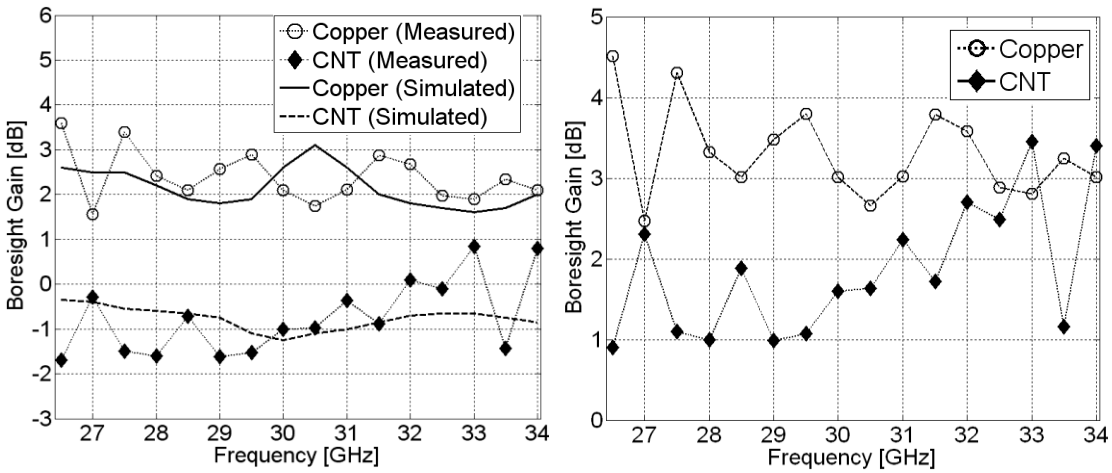

Figure 6.22. Boresight gain of single monopole antenna. (a) measured and simulated gain at Ref. plane 1. (b) measured gain at Ref. plane 2.

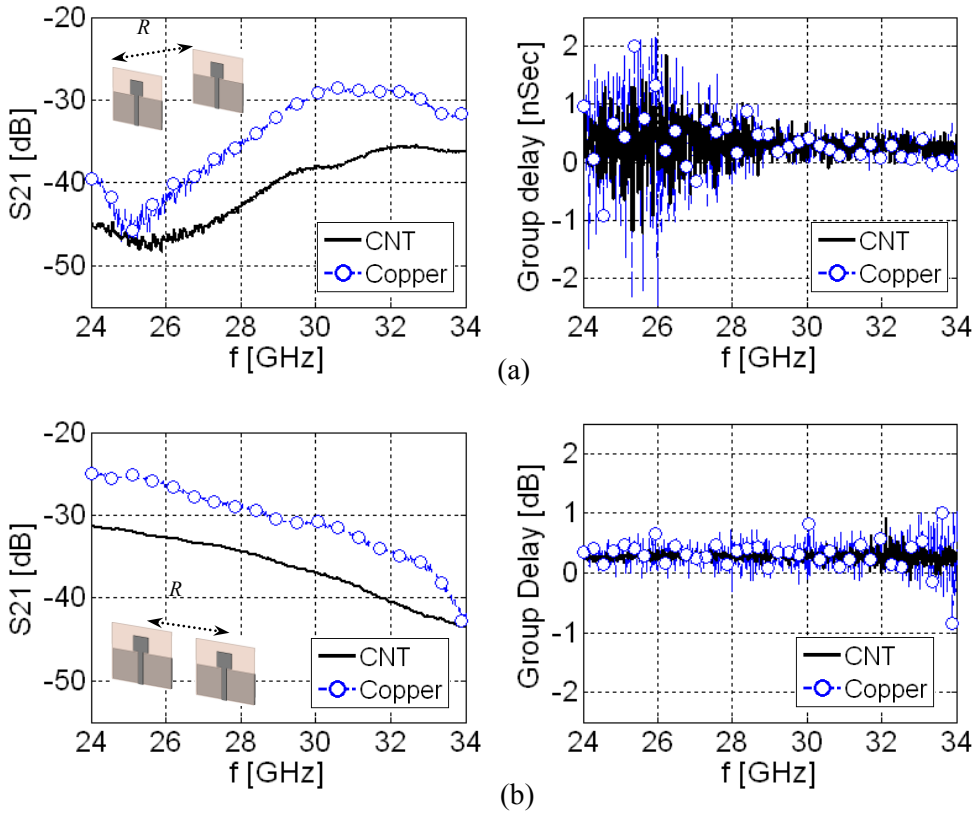

Figure 6.23. Transfer function of monopole antenna in Tx/Rx configuration for R = 30 mm, (a) face-to-face, and (b) side-by-side setups.

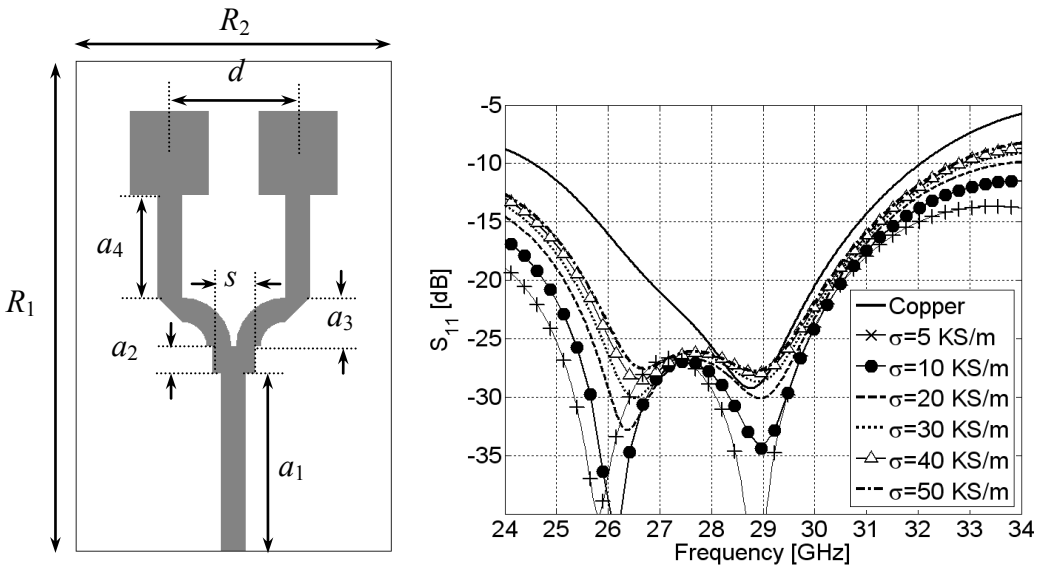

Figure 6.24. (a) The geometry of two-element array antenna. (b) simulated S_{11} versus conductivity.

6.5.2 Two-Element Antenna Array and Measurements

As shown in Figure 6.26(a), the two-element array fed by a matched T-junction is designed to operate from 24 to 34 GHz. The separation distance between elements is d = 5.7mm which is about 0.5λ at 26.5 GHz. The geometrical parameters are $R_1 = 22$, $R_2 = 14$, $a_1 = 8$, $a_2 = 1.2$, $a_3 = 2.2$, $a_4 = 4.6$, and $s = 1.9$ mm. The ground plane height is 15.5 mm.

The simulated reflection coefficient of the array antenna for various conductivities is shown in Figure 6.26(b). Due to the bandwidth limitation of the T-junction feed network, the impedance match is degraded at upper edge of frequency range for the copper antenna, and the maximum frequency of operation is decreased to 32 GHz. An impedance match with $S_{11} < -10$dB is desired.

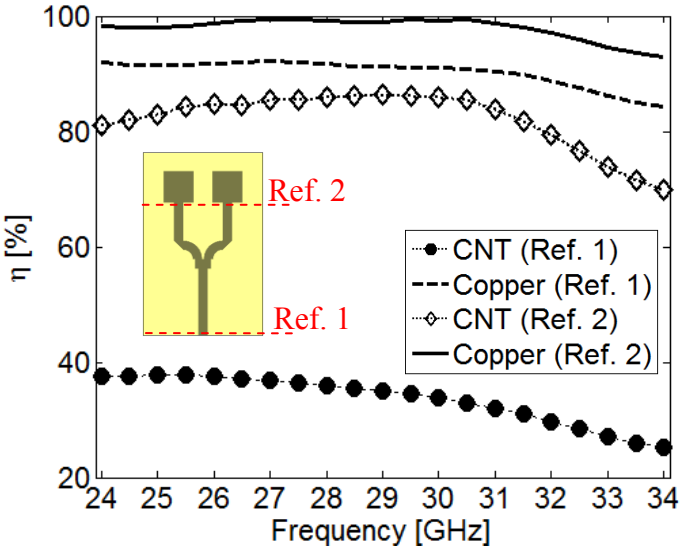

Figure 6.25. Radiation efficiency of the copper and CNT array antennas.

The radiation efficiency of the copper and CNT array antennas is calculated over the 24 to 34 GHz frequency range as displayed in **Figure 6.25**. The curves labeled Ref. 2 give the radiation efficiency of the antenna alone. The curves labeled Ref. 1 give the efficiency of the system made up of the lossy feed structure plus the antenna. The ohmic loss of the matched T-junction and the feed lines reduces the efficiency of the system greatly compared to the efficiency of the antenna alone.

The copper and CNT array antennas were fabricated and the reflection coefficient S_{11} was measured as shown in Figure 6.26(a). Good agreement is observed between measurement and simulation results, specifically when the effect of connectors are considered in EM model of antenna. As expected, unlike the CNT antenna, the upper-edge operating frequency of copper antenna is reduced to 32.2 GHz.

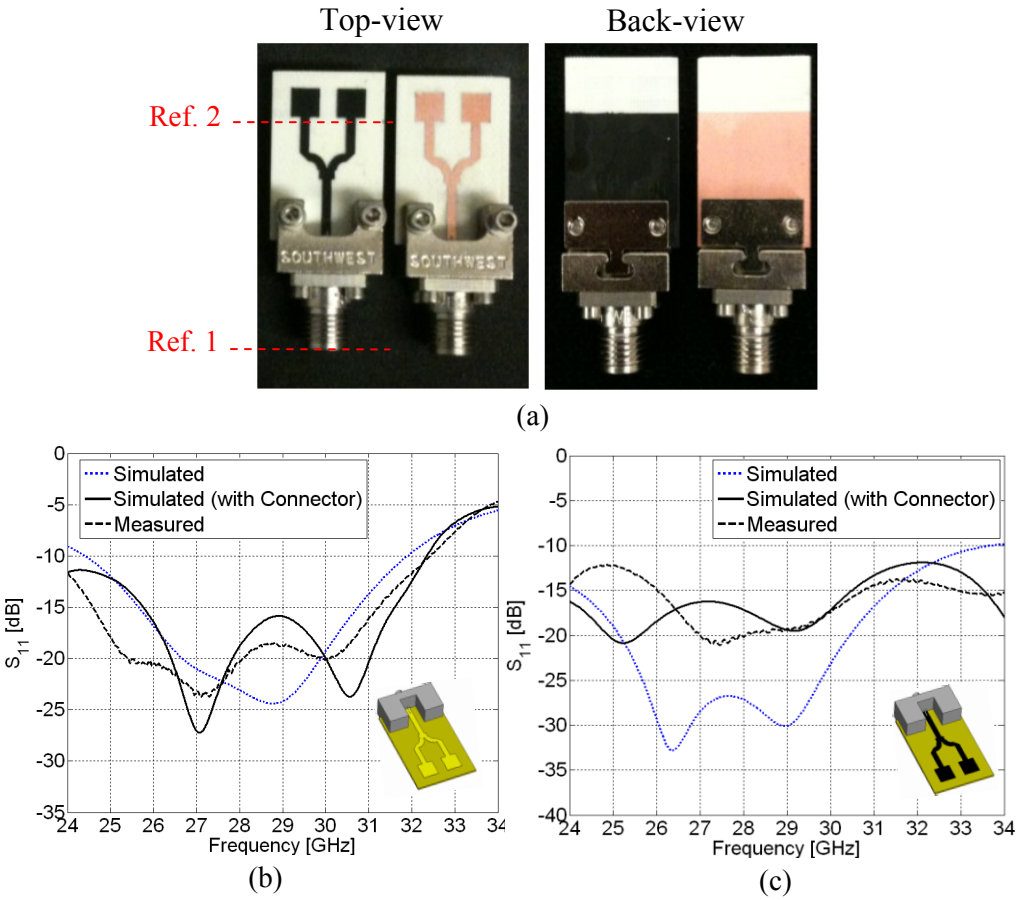

Figure 6.26. (a) Fabricated CNT and copper array antenna, (b) S_{11} of copper antenna, (c) S_{11} of CNT antenna.

The normalized radiation patterns of the copper and the CNT array antennas were measured and compared at two frequencies, 26.5 and 30 GHz, as shown in Figure 6.27. It is observed that CNT antenna shows a stable radiation performance over the frequency range of interest.

The gain at the boresight angle of $\theta = 0^{\circ}$, $\varphi = 90^{\circ}$ at reference plane 1 is shown in Figure 6.28(a). Simulations show that the loss of composite T-junction between the connector and reference plane 2 is about 3.5-4.4 dB from 24 to 34 GHz. Taking out the loss of the connector and feed network, the simulated boresight gain of antenna array at reference plane 2 is shown in Figure 6.28(b).

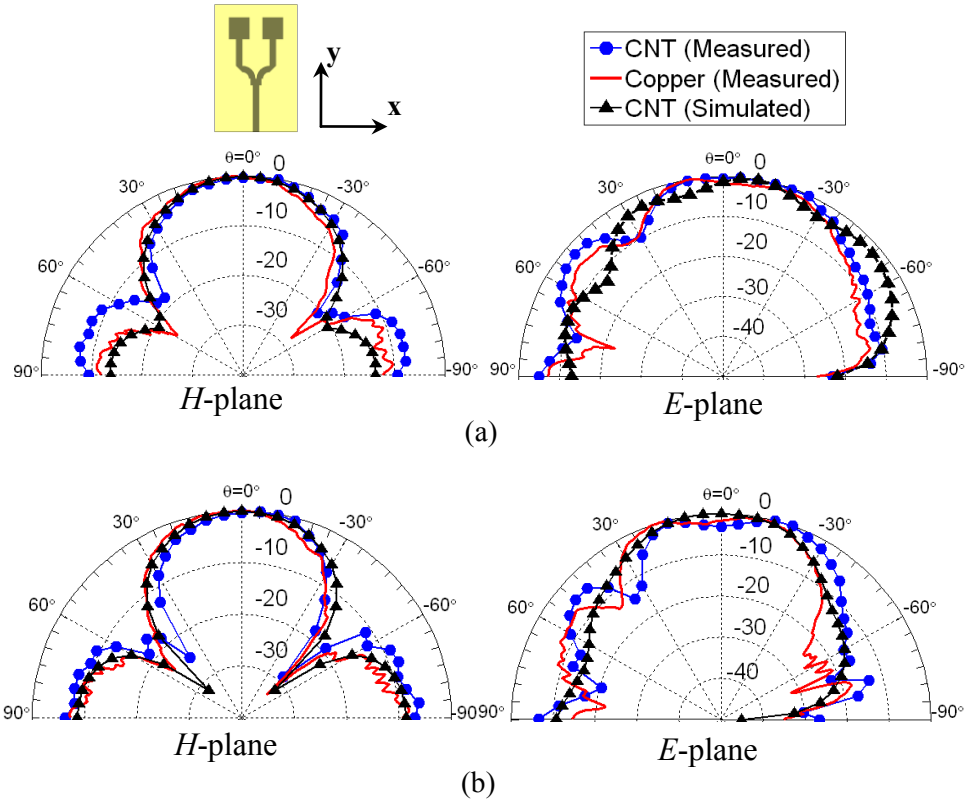

Figure 6.27. Normalized radiation pattern of array antenna at: (a) 26.5 GHz, (b) 30 GHz.

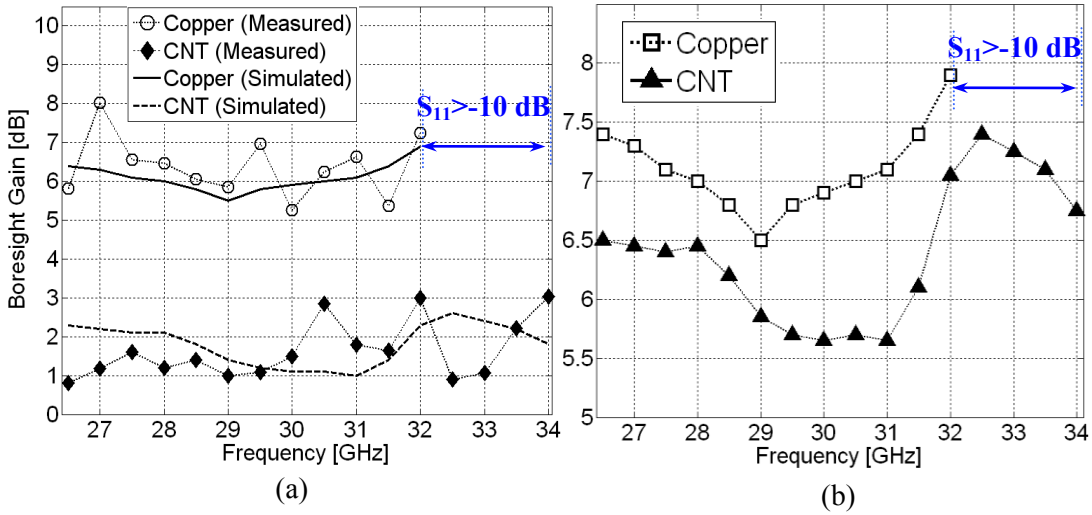

Figure 6.28. Boresight gain of array antenna, (a) measured and simulated gain at Ref. plane 1. (b) simulated gain at Ref. plane 2.

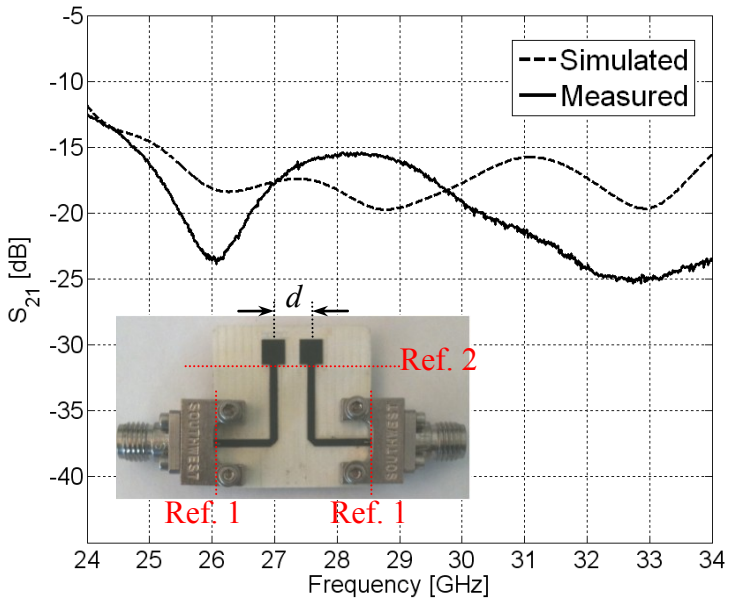

Figure 6.29. Mutual coupling of CNT antenna elements at Ref. plane 2.

6.5.3 Mutual Coupling

The mutual coupling between the adjacent elements of the array is investigated Figure 6.29 from 24 to 34 GHz. The separation distance between the monopole antennas is d = 5.7 mm. By removing the losses in the microstrip line and the connectors, the mutual coupling between two antennas is obtained at reference plane 2. It is observed that the mutual coupling is lower than -15 dB over almost entire frequency range of interest. It should be noted that the level of mutual coupling between ports at reference plane 1 highly depends on the length of microstrip lines connecting reference plane 1 to reference plane 2. By increasing the microstrip line length by ΔL cm, the mutual coupling at reference plane 1 would increase by $2 \times (\Delta L) \times 2.6$ dB. This issue could be useful for dense integrated circuits where it is desirable to space elements as closely as possible, and also desirable to avoid strong EM coupling between ports.

6.5.4 Housing Effect

The performance of an antenna can be considerably affected by nearby objects [162]-[164]. Usually the antenna is integrated in a circuit which includes various components and modules. In mobile and vehicular applications, the antenna could be used in the proximity of a variety of materials, such as metal objects or the human body. Therefore, the housing effect becomes a major issue to be addressed.

When the antenna radiates in the vicinity of an object, the backscattered fields produced by the object induce electric current on the antenna, affecting the antenna performance. The induced current on the antenna, I_s, caused by the backscattered magnetic field from the nearby scatterer, H_{scat}, can be expressed as [48],

$$I_s \propto \left(\frac{\eta_0}{\eta_0 + Z_s} \right) . H_{scat} \tag{6.2}$$

where

$$Z_s = (1+j)\sqrt{\frac{\pi f \mu_0}{\sigma}}. \tag{6.3}$$

Z_s is the surface impedance of the antenna. Due to the lower conductivity, the composite antenna produces weaker radiated fields than copper antenna, leading to lower H_{scat}. Moreover, Z_s is larger for the composite, making the ratio in (6.2) lower. As a result, the CNT antenna is not as much affected by nearby conductive objects as copper antenna.

Since metals produce the maximum backscattered fields because of their high conductivity, we assume a steel sheet as the nearby object to the antenna in our study. The housing effect setup is shown in Figure 6.30(a). A 5 cm × 5 cm steel sheet is placed very close in the front of the antenna with a separation distance of d. The reflection

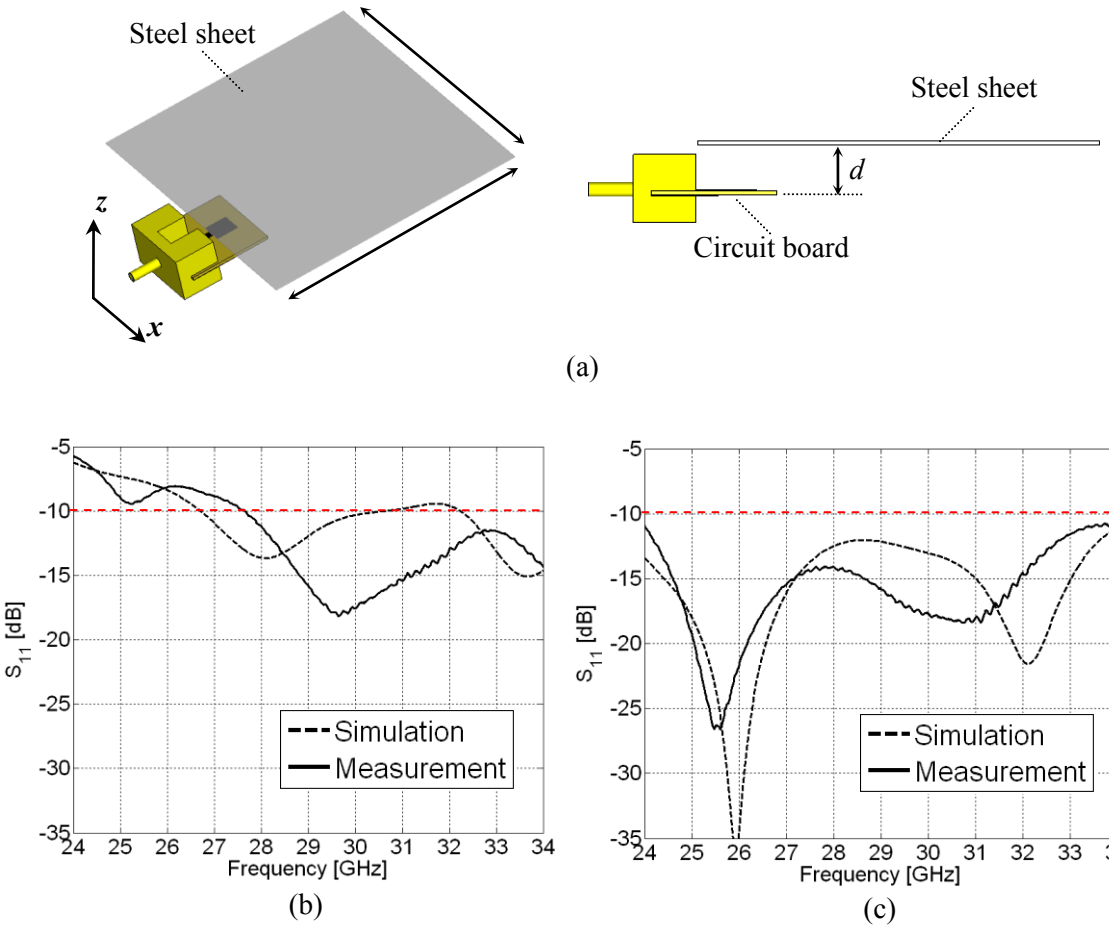

Figure 6.30. (a) Housing effect setup, (b) S_{11} of copper antenna, (c) S_{11} of CNT antenna.

coefficient of the CNT and copper antennas is measured for d = 2mm, as displayed in Figure 6.30(b) and (c). It is observed that the performance of the copper antenna deteriorates significantly, whereas the CNT antenna still operates over the entire frequency range with S_{11}<-10 dB. We have also investigated the housing effect for different values of d, not shown here. It was observed that CNT antenna performance shows much lower sensitivity to the steel sheet than does the copper antenna.

The far-field radiation pattern of the antennas in the vicinity of steel sheet is evaluated as shown in Figure 6.31. Since the metal sheet behaves like a good reflector, the main beam of the radiation pattern moves obviously toward the antenna back and the *H*-plane

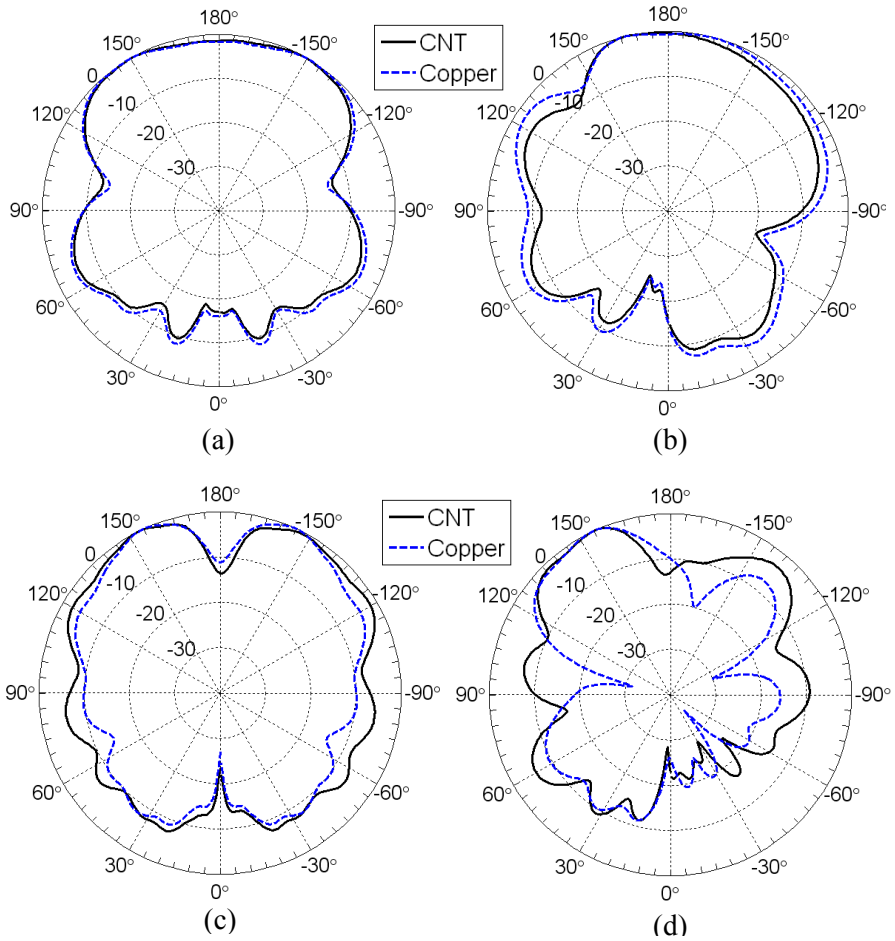

Figure 6.31. Normalized radiation pattern in the vicinity of metal sheet, (a) *H*-plane at 25 GHz, (b) *E*-plane at 25 GHz, (c) *H*-plane at 34 GHz, (d) *E*-plane at 34 GHz.

radiation pattern is not omnidirectional anymore. It is observed that as frequency goes up, the number of minima in the radiation pattern increases which is due to the reflections and diffractions of metal sheet. As a matter of fact, the path difference between the radiated field of the antenna and reflected/diffracted fields caused by the metal sheet would be comparable to the half-wavelength at high frequencies, leading to the cancellation of electric field at the minimum points. However, because of the lower EM coupling with the nearby metal sheet, the CNT antenna shows much weaker minima at

Table 6.8: Radiation efficiency of the composite antenna with/without the presence of metallic sheet

f (GHz)	24	26	28	30	32	34
Antenna	84.4	86.3	85.9	85.3	81.1	76.4
Antenna+Housing	82.1	80.2	79.6	81.2	79	76.8

E-plane than copper antenna as shown in Figure 6.31(d). We found that the CNT antenna shows weaker minima than copper antenna at *E*-plane at frequencies above 30 GHz as well, showing more stable radiation pattern. At lower frequencies, both antennas show almost the same radiation pattern.

The radiation efficiency of the composite antenna at reference plane 2 in the vicinity of metal sheet is calculated as shown in **Table 6.8**. It is observed that the radiation efficiency of the antenna changes slightly in the presence of the metal sheet. Therefore, since the matching of composite antenna is still good, the total efficiency does not change significantly.

6.6 Summary

In this Chapter, the use of CNT composites was investigated numerically and experimentally for building antennas for different antenna applications, namely RFID, WLAN, X-band, and mm-wave antennas. Metal in the antenna structure was replaced with CFC. The gain of the antenna degrades due to the low conductivity of composites compared to metals. The composite antenna performance was evaluated both numerically and experimentally, and good agreement was found between the simulations and the measurements.

The SWCNT composite material was used to build different microstrip antennas for single-band, multiband, and wideband applications. A new fabrication procedure was used to print the SWCNT buckepaper on any desired type of substrate. The T-match bow-tie antenna, meander line antenna, multiband fractal antenna, square ring slot patch, and the microstrip-fed monopole antennas were proposed and fabricated for various antenna applications. The performance of the antennas such as impedance bandwidth, radiation pattern, and gain were studied in detail.

Chapter 7 : Conclusion

7.1 Summary

In this thesis, we studied two most promising carbon-fiber composite (CFC) materials, namely reinforced continuous carbon fiber (RCCF) composite and carbon nanotube (CNT) composite. The shielding effectiveness of CFCs was investigated carefully in Chapters 2 and 3. The exact solution for the Green's function of a dielectric slab backed by a CFC ground plane was calculated in Chapter 4. We explored using CFCs in various antenna applications such as UHF-RFID, Bluetooth, WLAN, UWB, X-band, and mm-wave applications in Chapters 5 and 6.

In Chapters 2 and 3, due to the complex structure of the reinforced composites and also in order to avoid the time-consuming full-wave methods, the equivalent models of the structure of a CFC were used to analyze the shielding characteristics. In contrast with isotropic model, the highly accurate anisotropic equivalent models were used for RCCF modeling. It was shown, both numerically and experimentally, that using different orientation patterns in the multilayer RCCF composites controls the shielding properties of the structure. We evaluated the effect of incident angle and polarization angle of incident plane wave on the shielding of perpendicular ($E\perp$) and parallel ($E_{||}$) modes. It was observed that the SE changes considerably with the polarization angle γ at higher frequencies, and the SE decreases for $E_{||}$ and increases for $E\perp$ as the incidence angle increases. The coaxial cable fixture and standard waveguides were used for shielding effectiveness measurements. The shielding and conductivity characteristics of the

proposed highly conductive MWCNT composites were investigated over a wide frequency range up to 26.5 GHz. It was shown that the SE level can reach to 90 dB over a part of K-band and more than 60 dB over G-, X- and Ku-band frequency ranges by loading the CFC with only 8%*wt* of multi-walled carbon nanotubes (MWCNT). The proposed nanocomposites showed an outstanding improvement in shielding effectiveness compared to the other type of CNT composites introduced in literature so far.

In Chapter 4, using the spectral domain method, the Green's function was obtained for an infinitesimal HED on a dielectric slab over a CFC ground plane. Because CFCs have high conductivity, they were modeled using a surface impedance. The expressions for the electric field components were derived. The integration details such as dealing with surface wave poles and slowly converging integral were addressed carefully. It was shown that the electromagnetic fields at the air-dielectric interface depend on both the conductivity and anisotropic characteristics of the composite ground plane. The Green's function presented is versatile and can be used in the numerical modeling of any kind of microstrip structure with a CFC ground plane.

In Chapters 5 and 6, the use of RCCF and single-walled carbon nanotube (SWCNT) composite was investigated numerically and experimentally for building antennas. The metal in the antenna is replaced with a CFC. In addition to low cost, low weight, ease of fabrication and good corrosion resistance, the composite antennas were shown to have promising electrical characteristics. However, the radiation efficiency degrades due to the low conductivity of composites compared to metals.

We used RCCF composites to build RFID and UWB antennas. It was shown that the anisotropic nature of the conductivity of RCCF composites can be used to control the

direction of current flow. In order to enhance the conductivity of RCCF composite, a small volume fraction of MWCNTs was added to the RCCF material. The light-weight RCCF composite antenna was shown to operate well over UWB frequency range.

As one of the highest conductive materials, SWCNT buckypaper was used to build composite antennas. A new fabrication method was proposed to print arbitrarily-shaped full-composite SWCNT antenna on any type of substrate. Buckypaper was hardened by resin infiltration in order to be processed on the milling machine. Various types of SWCNT antennas were fabricated for different antenna applications. We fabricated T-match bow-tie and meander line antennas for UHF-RFID, modified Sierpinski fractal antenna for UHF-RFID/Bluetooth/WLAN, the square ring slot antenna for X-band, and planar monopole antennas for wideband mm-wave application operating over the 24-34 GHz frequency range. Good agreement was observed between simulation and experimental results for all the aforementioned composite antennas. It was shown that the gain and RFID read-range of composite antennas can be controlled by using different conductivities. This is not possible for materials with fixed conductivity such as copper. Furthermore, the matching between input impedances of the RFID IC chip and the RFID tag can be also controlled by using composite materials with different values of conductivity and thickness. The mm-wave composite antenna showed low dispersion characteristics over the frequency range of interest and so may be used for ultra-wideband radios. The housing effect on the composite antenna performance was investigated and it was shown that the composite antenna is much less affected than the copper antenna.

The performance of a microstrip patch antenna with ground plane made of RCCF composite was investigated. The patch was designed to operate at 5.6 GHz. It was observed that the impedance bandwidth of the antenna highly depends on the direction of the fibers in the ground plane. When the fibers are oriented in the direction of current flow in the copper ground plane, the patch antenna with the RCCF ground shows the same resonant behavior as the antenna with the copper ground plane.

7.2 Future Work

The shielding properties of real structures (aircraft, helicopters, spacecraft and so on) having a fuselage made of composite material can be characterized using accurate electromagnetic models of composites. It should be noted that the plane-wave SE of a composite sample may not guarantee the same level of shielding when used to build a three dimensional structure such as an aircraft fuselage. For example, aircraft have windows in the fuselage which may affect the shielding significantly. All reported works in analysis of aircraft shielding are focused on a metal fuselage. In addition to shielding, interference path loss (IPL) is an important issue in aircraft which could be investigated using a composite fuselage [165]. IPL is associated with transmission paths from a transmitter inside the aircraft cabin to an antenna mounted on the outside the fuselage, such as a GPS antenna. Usually to measure the IPL, the transmitter antenna is located close to a window in the fuselage and the coupling is measured between transmitter and external antenna on the top of the fuselage. It should be noted that by including all the materials present inside the fuselage, such as seats and bulkheads, in EM models of aircraft, the accuracy of results could be improved considerably.

It would be interesting to produce composites with high conductivity or adjustable conductivity for various antenna applications. We may control the gain of a composite antenna by adjusting the conductivity. Recently, we have mixed SWCNTs with MWCNTs to control the material's conductivity. This issue is under investigation. Increasing the composite's conductivity could be another issue to be studied. It was shown that highly-conductive MWCNT samples can be produced efficiently by using the three-roll milling technique. However, there is a room to do further research to evaluate the possibility of fabricating more highly conductive composite materials.

It was shown that the anisotropic conductivity tensor affects the performance of RCCF composite antennas, and this suggests many possibilities for new antenna configurations. By controlling the current distribution over the surface of an RCCF antenna, one may achieve interesting radiation characteristics without changing the antenna geometry.

Composite materials can be used in many other antenna applications beyond those presented in this dissertation. For example, conformal antennas might be of interest [123],[166][167]. As a matter of fact, the main application of conformal antennas is in avionic systems and it is one of the very well-known antennas mounted on aircraft. Typically, a conformal antenna is used in arrays which could be distributed on the curved surface of the aircraft body. Since composites are extensively used in aircraft fuselage to replace metals, it would be interesting to make a composite conformal antenna.

In order to reduce the cost of manufacturing, inkjet printing is one of the most desirable techniques to fabricate antennas, using conductive nanoparticles in solution in the ink. The shape of the antenna is printed directly on the substrate, with no waste as in a conventional etching technique. Recently, CNTs have been printed using the inkjet

printing technique [136][168]. The low conductivity of the ink leads to the need for several overwritings to obtain a sufficiently thick layer. Producing highly conductive SWCNT composites using inkjet printing method could be considered as important research in future work.

References

[1] D. J. De Renzo, *Advanced composite materials products and manufacturers*, William Andrew, 1988.

[2] A. Kelly, "Composites in context," *Compos Sci Technol*, Vol. 23, Issue. 3, pp. 171-199, 1985.

[3] R. F. Gibson, *Principles of Composite Material Mechanics*, McGraw Hill Inc., 1994.

[4] D. Hull and T. W. Clyne, *An Introduction to Composite Materials*, Second edition, Cambridge University Press, 1996.

[5] S. V. Hoa, *Principles of the Manufacturing of Composite Materials*, DEStech Publications Inc., 2009.

[6] L. A. Pilato and M. J. Michno, *Advanced Composite Materials*. Berlin: Springer-Verlag, 1994.

[7] D. Gay, S. V. Hoa, and S. W. Tsai, *Composite materials: design and applications*, Boca Raton, FL: CRC Press, 2003.

[8] A, Baker, S. Dutton, and D. Kelly, *Composite Materials for Aircraft Structures*, American Institute of Aeronautic and Astronautics Inc., 2004.

[9] A. Badanoiu, J. Holmgren, "Cementitious composites reinforced with continuous carbon fibres for strengthening of concrete structures," *Cement & Concrete Composites*, Vol. 25, pp. 387–394, 2003.

[10] T. Yamada, "Modeling of kink-shaped carbon-nanotube Schottky diode with gate bias modulation," *Appl. Phys. Lett*. Vol. 80, pp. 4027-4029, 2002.

[11] X. C. Tong, *Advanced materials and design for electromagnetic interference shielding*, Taylor & Francis Group, LLC, 2009.

[12] J. M. F. de Paiva, A. de Nadai dos Santos, and M. C. Rezende, "Mechanical and morphological characterizations of carbon fiber fabric reinforced epoxy composites used in aeronautical field," *Materials Research*, Vol. 12, No. 3, pp. 367-374, 2009.

[13] E. C. Botelho, R. A. Silva, L. C. Pardini, M. C. Rezende, "A review on the development and properties of continuous fiber/epoxy/aluminum hybrid composites for aircraft structures" *Materials Research*, Vol. 9, No. 3, 247-256, 2006.

[14] D. D. L. Chung, "Review Electrical applications of carbon materials" *Journal of Materials Science*, Vol. 39, pp. 2645-2661, 2004.

[15] S. Yang, K. Lozano, A. Lomeli, H. D. Foltz, and R. Jones, "Electromagnetic interference shielding effectiveness of carbon nanofiber/LCP composites," *Composites*: *Part A* , Vol. 36, pp. 691-697, 2005.

[16] S.-E. Lee, J.-H. Kang, and C.-G. Kim, "Fabrication and design of multi-layered radar absorbing structures of MWNT-filled glass/epoxy plain-weave composites," *Composite Structures*, Vol. 76, pp. 397-405, 2006.

[17] S.-E. Lee, K.-S. Oh, and C.-G. Kim, "Electromagnetic characteristics of frequency selective fabric composites," *Electronic Lett*., Vol. 42, No. 8, pp. 2006.

[18] K.-Y. Park, S.-E. Lee, C.-G. Kim, and J.-H. Han, "Fabrication and electromagnetic characteristics of electromagnetic wave absorbing sandwich structures," *Composites Sci. Technol.*, Vol. 66, pp. 576-584, 2006.

[19] C. M. Chang, J. C. Chiu, Y. F. Lan, J. W. Lin, C. Y. Yeh, W. S. Jou, .J. J. Lin, and W. H. Cheng, "High electromagnetic shielding of a 2.5-Gbps plastic transceiver module using dispersive multiwall carbon nanotubes", *IEEE J. Lightwave Technology*, Vol. 26, pp. 1256-1262, 2008.

[20] W. S. Jou, H. Z. Cheng, and C. F. Hsua, "The electromagnetic shielding effectiveness of carbon nanotubes polymer composites," *J. Alloys Compounds*, Vol. 434-435, pp. 641-645, 2007.

[21] C. S. Zhang, Q. Q. Ni, S.Y. Fu, and K. Kurashiki, "Electromagnetic interference shielding effect of nanocomposites with carbon nanotube and shape memory polymer," *Comp. Sci. Technol*., Vol. 67, pp. 2973–2980, 2007.

[22] I. M. De Rosa, F. Sarasini, M. S. Sarto, and A. Tamburrano, "EMC impact of advanced carbon fiber/carbon nanotube reinforced composites for next-generation aerospace applications," *IEEE Trans. Electromagn. Compat*., Vol. 50, pp. 556-563, 2008.

[23] R. A. Tellakula, V. K. Varadan, T. C. Shamy, and G. N. Mathur, "Carbon fiber and nanotube based composites with polypyrrole fabric as electromagnetic absorbers," *Smart Mater. Struct.*, Vol. 13, pp. 1040–1044, 2004.

[24] N. N. Hoang, J.-L. Miane, and J.-L. Wojkiewicz, "Modeling of electromagnetic shielding effectiveness of multilayer conducting composites in the microwave band," *in Proc. IEEE Communications and Electronics (ICEE'06)*, 2006, pp. 482-485.

[25] C. L. Holloway, M. S. Sarto, and M. Johansson, "Analyzing carbon-fiber composite materials with equivalent-layer models," *IEEE Trans. Electromagn. Compat.*, vol. 47, no. 4, pp. 833-844, 2005.

[26] H. Rmili, J.-L. Miane, H. Zangar, and T. Olinga, "Design of microstrip-fed proximity-coupled conducting polymer patch antenna," *Microw. Opt. Technol. Lett.*, Vol. 48, pp. 655–660, 2006.

[27] Y. Bayram Y. Zhou, J.L. Volakis, B-S. Shim and N.A. Kotov, "Conductive textiles and polymer-ceramic composites for novel load bearing antennas," *Proc. IEEE Antenna and Propagation Symposium* (*APS* 2008), July 2008.

[28] P. V. Nikitin, S. Lam, and K. V. S. Rao, "Low cost silver ink RFID tag antennas," in *Proc. IEEE Antennas Propag. Society Int. Symp.*, 2005, pp. 353-356.

[29] L. Yang, A. Rida, R. Vyas, and M. M. Tentzeris, "RFID tag and RF structures on a paper substrate using inkjet-printing technology," *IEEE Trans. Microw. Theory Tech.*, Vol. 55, pp. 2894–2901, 2007.

[30] S. Ludmerer, "Conductive Inks for RFID Antenna: the low cost high speed route to RFID labels," Parelec. Inc. Available Online: www.parelec.com.

[31] J. Anguera, J.-P. Daniel, C. Borja, J. Mumbru, C. Puente, T. Leduc, N. Laeveren, P. Van Roy, "Metallized foams for fractal-shaped microstrip antennas," *IEEE Antennas and Propagat. Mag.*, Vol. 50, pp. 20-38, 2008.

[32] T. J. Duggan, "Military aircraft electromagnetic compatibility: release to service testing in the United Kingdom, past, present and future," *in Proc. IEEE International Symp. Electromagn. Compat.*, Jul. 2007.

[33] T. X. Nguyen, S. V. Koppen, J. J. Ely, G. N. Szatkowski, J. J. Mielnik and T. P. Salud, "Small aircraft RF interference path loss measurements," *in Proc. IEEE International Symp. Electromagn. Compat.*, Jul. 2007.

[34] T. X. Nguyen, S. V. Koppen, J. J. Ely, R. A. Williams, L. J. Smith, and M. T. Salud, "Portable wireless LAN device and two-way radio threat assessment for aircraft VHF communication radio band," NASA Langley Res. Center, Hampton, VA, NASA/TM-2004-213010, Mar. 2004.

[35] H. Bagci, A. E. Yilmaz, J.-M. Jin, and E. Michielssen, "Fast and rigorous analysis of EMC/EMI phenomena on electrically large and complex cable-loaded structures," *IEEE Trans. Electromagn. Compat.*, Vol. 49, No. 2, pp. 361-381, 2007.

[36] M.-S. Lin and C. H. Chen, "Plane-Wave shielding characteristics of anisotropic laminated composites," *IEEE Trans. Electromagn. Compat*. vol. 35, pp. 21-27, 1993.

[37] M. Parise, and M. S. Sarto, "Efficient formulation of high-order boundary conditions for the high-frequency modeling of multilayer composite slab," *Proc*. *of IEEE International Symposium on Electromagn. Compat.*, 2003, pp. 753-758.

[38] H.-Ke Chiu, H.-C. Chu, and C. H. Chen, "Propagation modeling of periodic laminated composite structures," *IEEE Trans. Antenna Propagat*. Vol. 40, pp. 218-224, 1998.

[39] A. Todoroki, M. Tanaka, and Y. Shimamura, "Measurement of orthotropic electric conductance of CFRP laminates and analysis of the effect on delamination

monitoring with an electric resistance change method," *Comp. Sci. Technol.*, Vol. 62, pp. 619-628, 2002.

[40] J. B. Park, T. K. H. Wang, H. G. Kim, and Y. D. Doh, "Experimental and numerical study of the electrical anisotropy in unidirectional carbon-fiber-reinforced polymer composites," *Smart Mater*. *Struct*. Vol. 16, pp. 57-66, 2007.

[41] H.-C. Chu, S.-K. Jeng, and C. H. Chen, "Reflection and transmission characteristics of lossy periodic composite structures," *IEEE Trans. Antenna Propagat.* Vol. 44, pp. 580-587, 1996.

[42] A. Balzano, I. M. De Rosa, F. Sarasini and M. S. Sarto, "Effective properties of carbon fiber composites: EM modeling versus experimental testing," *Proc. of IEEE Int. Symp. EMC*, Honolulu, HW, Jul. 2007.

[43] M. S. Sarto, "Hybrid MFIE/FDTD analysis of the shielding effectiveness of a composite enclosure excited by a transient plane wave," *IEEE Trans. Magnetics*, Vol. 36, pp. 946-950, 2000.

[44] *CONCORDIA CENTER FOR COMPOSITES* (*CONCOM*), Concordia University, QC, Canada, 1979. Online: http://concom.encs.concordia.ca.

[45] M.-S. Lin, C.-M. Lin, R.-B. Wu, and C. H. Chen, "Transient propagation in anisotropic laminated composites," *IEEE Trans. Electromagn. Compat*. Vol. 35, pp. 357-365, 1993.

[46] C. Buccella, "Quasi-Stationary analysis of the electric field in anisotropic laminated composites," *IEEE Trans. Industry App*., Vol. 35, pp. 1296-1305, 1999.

[47] M. S. Sarto, and C. L. Holloway, "Effective boundary conditions for the time-domain analysis of the EMC performances of fiber composites", *Proc*. *of IEEE International Symposium on Electromagn. Compat.*, 1999, pp. 462-467.

[48] R. E. Collin, Field *Theory of Guided Waves*, New York, McGraw-Hill, 1991.

[49] M. N. O. Sadiku, *Numerical Techniques in Electromagnetics*, CRC Press. 2001.

[50] S. J. Ofranidis, *Electromagnetic Waves and Antennas*, ECE Department, Rutgen University, 2002.

[51] J. Avloni, M. Ouyang, L. Florio, A. R. Henn and A. Sparavigna, "Shielding effectiveness evaluation of metallized and polypyrrole-coated fabrics," *Journal of Thermoplastic Composite Materials*, Vol. 20, pp. 241-254, 2007.

[52] I. S. Seo, W. S. Chin, and D. G. Lee, "Characterization of electromagnetic properties of polymeric composite materials with free space method," *Composite Structures*, Vol. 66, pp. 533–542, 2004.

[53] S. Yang, K. Lozano, A. Lomeli, H. D. Foltz, R. Jones, "Electromagnetic interference shielding effectiveness of carbon nanofiber/LCP composites," *Composites*: *Part A*, Vol. 36, pp. 691-697, 2005.

[54] T. W. Więckowski, and J. M. Janukiewicz, "Methods for evaluating the shielding effectiveness of textiles," *FIBRES & TEXTILES in Eastern Europe*, Vol. 14, pp. 18-22, 2006.

[55] R. K. Challa, D. Kajfez, V. Demir, J. R. Gladden, and A. Z. Elsherbeni, "Characterization of multiwalled carbon nanotube (MWCNT) composites in a waveguide of square cross section," *IEEE Microwave and Wireless Components Lett*., Vol. 18, No. 3, pp. 161-163, 2008.

[56] http://www.microwaves101.com/encyclopedia/waveguidedimensions.cfm

[57] A. Mehdipour, C. W. Trueman, A. R. Sebak, I. D. Rosca and S. V. Hoa, **"**Shielding effectiveness analysis of multilayer carbon-fiber composite materials" *Presented in General Assembly of the International Union of Radio Science* (*URSI* 2008), Chicago, USA, 2008.

[58] Hexion Specially Chemicals Inc., Columbus, OH, 2006.

[59] Freeman Mfg. & Supply Co., Columbus, OH, 2001.

[60] S. Ijima, "Helical microtubules of graphitic carbon," *Nature*, Vol. 354, pp. 56-58, 1991.

[61] E. T. Thostenson, C. Li, and T.-W. Chou, "Nanocomposites in context," *Comp. Sci. Technol*., Vol. 65, pp. 491-516, 2005.

[62] G. Y. Slepyan, S. A. Maksimenko, A. Lakhtakia, O. Yevtushenko, A. V. Gusakov, "Electrodynamics of carbon nanotubes: Dynamic conductivity, impedance boundary conditions, and surface wave propagation," *Physical Review B*, Vol. 60, No. 24, pp. 17136-17149, 1999.

[63] A. M. K. Esawi, and M. M. Farag, "Carbon nanotube reinforced composites: Potential and current challenges," *Materials and Design*, Vol. 28, pp. 2394–2401, 2007.

[64] W. Bauhofer, and J. Z. Kovacs, "A review and analysis of electrical percolation in carbon nanotube polymer composites", *Compos. Sci. Technol*. *Comp*. *Sci*. *Technol*., Vol. 69, pp. 1486-1498, 2009.

[65] F. H. Gojny, M. H. G. Wichmann, B. Fiedler, I. A. Kinloch, W. Bauhofer, A. H. Windle, and K. Schulte, "Evaluation and identification of electrical and thermal conduction mechanisms in carbon nanotube/epoxy composites," *Polymer*, Vol. 47, pp. 2036–2045, 2006.

[66] F. H. Gojny, M. H. G. Wichmann, B. Fiedler, and K. Schulte, "Influence of different carbon nanotubes on the mechanical properties of epoxy matrix composites - A comparative study," *Compos. Sci. Technol*., Vol. 65, pp. 2300–2313, 2005.

[67] E. T. Thostenson, S. Ziaee, and T. W. Chou, "Processing and electrical properties of carbon nanotube /vinyl ester nanocomposites," *Compos. Sci. Technol*., Vol. 69, pp. 801-804, 2009.

[68] E. T. Thostenson, and T. W. Chou, "Processing-structure-multi-functional property relationship in carbon nanotube/epoxy composites", *Carbon*, Vol. 44, pp. 3022–3029, 2006.

[69] J. Li, P. C. Ma, W. S. Chow, C. K. To, B. Z. Tang, and J. K. Kim, "Correlations between percolation threshold, dispersion state, and aspect ratio of carbon nanotubes," *Adv. Funct. Mater*., Vol. 17, pp. 3207–3215, 2007.

[70] J. B. Bai, and A. Allaoui, "Effect of the length and the aggregate size of MWNTs on the improvement efficiency of the mechanical and electrical properties of nanocomposites-experimental investigation," *Composites A*, Vol. 34, pp. 689–694, 2003.

[71] M. J. Jiang, Z. M. Dang, H. P. Xu, and S. H. Yao, "Effect of aspect ratio of multiwall carbon nanotubes on resistance-pressure sensitivity of rubber nanocomposites," *Appl. Phys. Lett*., Vol. 91, pp. (072907) 1-3, 2007.

[72] C. M. Chang, M. C. Lin, J. C. Chiu, W. S. Jou, and W. H. Cheng, "High-Performance electromagnetic susceptibility of plastic transceiver modules using carbon nanotubes," *J. Sel. Topics Quant. Electron*., Vol. 12, No. 6, pp. 1091–1096, 2006.

[73] H. M. Kim, K. Kim, S. J. Lee, J. Joo, H. S. Yoon, S. J. Cho, S. C. Lyu, and C. J. Lee, "Charge transport properties of composites of multiwalled carbon nanotube with metal catalyst and polymer: application to electromagnetic interference shielding," *Current Applied Physics*, Vol. 4, pp. 577–580, 2004.

[74] Z. Liu, G. Bai, Y. Huang, Y. Ma, F. Du, F. Li, T. Guo and Y. Chen, "Reflection and absorption contributions to the electromagnetic interference shielding of single-walled carbon nanotube/polyurethane composites," *Carbon*, Vol. 45, pp. 821–827, 2007.

[75] Y. Li, C. Chen, S. Zhang, Y. Ni and J. Huang, "Electrical conductivity and electromagnetic interference shielding characteristics of multiwalled carbon nanotube filled polyacrylate composite films," *Applied Surface Science*, Vol. 254, pp. 5766–5771, 2008.

[76] Y. Huang, N. Li, Y. Ma, F. Du, F. Li, X. He, X. Lin, H. Gao, and Y. Chen, "The influence of single-walled carbon nanotube structure on the electromagnetic interference shielding efficiency of its epoxy composites," *Carbon*, Vol. 45, pp. 1614–1621, 2007.

[77] P. C. Kim, and D. G. Lee, "Composite sandwich constructions for absorbing the electromagnetic waves," *Composite Structures*, Vol. 87 pp. 161–167, 2009.

[78] K. Umishita, T. Okubo, N. Takuya, and O. Hashimoto, "Absorption and shielding effect of electromagnetic wave at GHz frequency by multi-walled carbon nanotube/polymer composites," *Proc. of the 9th European Conf. on Wireless Tech.*, pp 291-294, 2006.

[79] A. Saib, L. Bednarz, R. Daussin, C. Bailly, X. Lou, J.-M. Thomassin, C. Pagnoulle, C. Detrembleur, R. Jérôme, and I. Huynen, "Carbon nanotube composites for broadband microwave absorbing materials," *IEEE Trans. Microw. Theory Tech.*, Vol. 54, No. 6, pp. 2745-2754, 2006.

[80] A. Mehdipour, I. D. Rosca, C. W. Trueman, A. R. Sebak, and S. V. Hoa, "High frequency shielding properties of multiwall carbon nanotube (MWCNT) composites" *Presented in The 1st Canadian and American Technical Conference on Composites* (*ASC/CACSMA*), DE, US, 2009.

[81] I. D. Rosca, and S. V. Hoa, "Highly conductive multiwall carbon nanotube and epoxy composites produced by three-roll milling," *Carbon*, Vol. 47, pp. 1958-1968, 2009.

[82] L. J. van der Pauw, "A method of measuring the resistivity and Hall coefficient on lamellae of arbitrary shape," *Phil. Tech. Rev*., Vol. 20, pp. 220-2244, 1958.

[83] J. Jang, J. Bae, and S. H. Yoon, "Study on the effect of surface treatment of carbon nanotubes for liquid crystalline epoxide–carbon nanotube composites," *J. Mater. Chem*., Vol. 13, pp. 676–681, 2003.

[84] D. Stauffer and A. Aharony, Introduction to Percolation Theory. Taylor & Francis, 1992.

[85] T. Itoh, *Numerical techniques for microwave and millimeter-wave passive structure*, Chapter 9, John Wiley and Sons, 1989.

[86] M. Koledintseva, P. C. Rawa, R. Dubroff, J. Drewniak, K. Rozanov and B. Archambeault, "Engineering of composite media for shields at microwave frequencies," *Proc. of IEEE Int. Symp. EMC*, Vol. 1, 2005, pp. 169-174.

[87] *CST – Microwave Studio*, Computer Simulation Technology, 2009.

[88] CST of America, "Efficient, accurate, reliable EM simulation tool", *Microwave Journal*, Oct. 2008.

[89] I. Munteanu, and T. Weiland, *RF & microwave simulation with the finite integration technique – from component to system design*, Springer Berlin Heidelberg, 2007.

[90] C. R. Paul, *Introduction to Electromagnetic Compatibility*, Wiley Series in Microwave and Optical Engineering, 1992.

[91] J.-F. Kiang, "Rectangular patch resonator with laminated ground plane," *IEEE Trans. Antenna and Propagat*., Vol. 43, pp. 1361-1368, 1995.

[92] G. N. Tsandoulas, "Excitation of a grounded dielectric slab by a horizontal dipole," *IEEE Trans*. *Antennas Propagat*., Vol. 15, pp. 156-161, 1969.

[93] M. A. Marin, S. Barkeshli, and P. H. Pathak, "Efficient analysis of planar microstrip geometries-using a closed-form asymptotic representation of the grounded dielectric slab green's function," *IEEE Trans. Microwave Theory Tech*., Vol. 37, pp. 669-679, 1989.

[94] M. I. Aksun and R. Mittra, "Derivation of closed-form Green's functions for a general microstrip geometry," *IEEE Trans. Microw. Theory Tech.*, Vol. 40, pp. 2055–2062, 1992.

[95] J. R. Mosig, F.E. Gardiol, "Analytical and numerical techniques in the Green's function treatment of microstrip antennas and scatterers," *IEE Proc*., Vol. 130. pp. 175-182, 1983.

[96] V. S. Reddy and R. Garg, "Efficient analytical evaluation of the asymptotic part of Summerfield type reaction integrals in microstrip/slot structures," *IEE Microw. Antenna. Propag*. Vol. 147, pp. 1-7, 2000.

[97] G.-W. Pan, J. Tan, and J. D. Murphy, "Full-wave analysis of microstrip floating-line discontinuities," *IEEE Trans. Electromagn. Compat*., Vol. 36, pp. 49-58, 1994.

[98] I. E. Rana, and N. Alexopoulos, "Current distribution and input impedance of printed dipoles," *IEEE Trans. Antenna and Propagat*., Vol. 29, pp. 99-105, 1981.

[99] D. Pozar, "Input impedance and mutual coupling of rectangular microstrip antennas," *IEEE Trans*. *Antennas Propagat*., Vol. 30, pp. 1191-1196, 1982.

[100] J. R. Mosig, T. K. Sarkar, "Comparison of quasi-static and exact electromagnetic fields from a horizontal electric dipole above a lossy dielectric backed by an imperfect ground plane" *IEEE Trans. Microwave Theory Tech*., Vol. 34, , pp. 379-388, 1986.

[101] E. H. Newman, and D. Forrai, "Scattering from a microstrip patch" *IEEE Trans. Antennas Propagat.*, Vol. 35, pp. 245-251, 1987.

[102] D. Pozar, "Improved computational efficiency for the moment method solution of printed dipoles and patches," *Electromagnetics*, Vol. 3, pp. 299-309, 1983.

[103] S.-L. Chen, and K.-H. Lin, "A slim RFID tag antenna design for metallic object applications," *IEEE Antennas and Wireless Propagat. Lett.*, Vol. 7, pp. 729-732, 2008.

[104] G. Marrocco, "The art of UHF RFID antenna design: impedance-matching and size-reduction techniques," *IEEE Antennas and Propagat. Magazine,* Vol. 50, pp. 66-79, 2008.

[105] K. Finkenzeller*, RFID Handbook*, 2nd ed. New York: Wiley, 2003.

[106] P. V. Nikitin, K. V. S. Rao, S. F. Lam, V. Pillai, R. Martinez, and H. Heinrich, "Power reflection coefficient analysis for complex impedances in RFID tag design," *IEEE Trans. Microw. Theory Tech.*, Vol. 53, pp. 2721–2715, 2005.

[107] M. Hirvonen, K. Jaakkola, P. Pursula, and J. Säily, "Dual-band platform tolerant antennas for radio-frequency identification," *IEEE Trans. Antenna Propagat.* Vol. 54, pp. 2632-2637, 2006.

[108] K. V. Seshagiri Rao*,* P. V. Nikitin*,* and S. F. Lam, "Antenna design for UHF RFID tags: a review and a practical application," *IEEE Trans. Antenna Propagat.* Vol. 53, pp. 3870-3876, 2005.

[109] G. Marrocco, "Gain-Optimized self-resonant meander line antennas for RFID applications," *IEEE Antennas and Wireless Propagat. Lett.*, Vol. 2, pp. 302-305, 2003.

[110] A. Mehdipour, A.-R. Sebak and C. W. Trueman, and S. V. Hoa "Carbon-Fiber composite T-match folded bow-tie antenna for RFID applications," Presented *in IEEE Antenna and Propagation Symposium* (*APS* 2009), Charleston, SC, June 1-5, 2009.

[111] *UHF Frequency ICs*, Texas Instrument Inc., Dallas, TX., 2006.Available online: http://focus.ti.com/docs/prod/folders/print/ri-uhf-strap-08.html.

[112] FCC, "FCC first report and order on ultra-wideband technology," 2002.

[113] P. Li, J. Liang*,* and X. Chen, "Study of printed elliptical/circular slot antennas for ultrawideband applications," *IEEE Trans. Antennas Propag.*, Vol. 54, pp. 1670–1675, 2006.

[114] T.-G. Ma, and C.-H.Tseng, "An ultrawideband coplanar waveguide-fed tapered ring slot antenna," *IEEE Trans. Antennas Propag.*, Vol. 45, pp. 1105–1110, 2006.

[115] N. Telzhensky and Y. Leviatan, "Planar differential elliptical UWB antenna optimization," *IEEE Trans. Antennas and Propag.*, vol. 54, no. 11, pp. 3400-3406, 2006.

[116] A. Mehdipour, K. Mohammadpour-Aghdam, R. Faraji-Dana, and M. R. Kashani-Khatib, "A novel coplanar waveguide-fed slot antenna for ultrawideband applications", *IEEE Trans. Antenna and Propagation.*, Vol. 56, pp. 3857-3862, 2008.

[117] A. Mehdipour, A. Parsa, A.-R. Sebak and C. W. Trueman, "Miniaturized CPW-fed antenna and band-notched design for UWB applications", *IET Microw. Antennas and Propag*, Vol. 3, pp. 974-986, 2009.

[118] Z. N. Chen, T. S. P. See, and X. Qing, "Small printed ultrawideband antenna with reduced ground plane effect", *IEEE Trans. Antennas Propag.*, Vol. 55, pp.383 –388, 2007.

[119] A. Mehdipour, A.-R. Sebak, C. W. Trueman, I. D. Rosca, and S. V. Hoa, "Reinforced continuous carbon-fiber composites using multi-wall carbon nanotubes for wideband antenna applications," *IEEE Trans. Antenna and Propagat*., Vol. 58, pp. 2451-2456, 2010.

[120] G. R. Aiello, and G. D. Rogerson, "Ultra-wideband wireless systems," *IEEE Microwave*, Vol. 4, pp. 36–47, 2003.

[121] Montoya T. P. and Smith G. S., "A study of pulse radiation from several broad-band loaded monopole," *IEEE Trans. Antennas Propag.*, Vol. 44, pp. 1172–1182, 1996.

[122] Z. N. Chen, X. H. Wu, H. F. Li, N. Yang, and M. Y. W. Chia, "Considerations for source pulses and antennas in UWB radio systems," *IEEE Trans. Antennas Propag.*, Vol. 52, pp. 1739–1748, 2004.

[123] L. Josefsson, and P. Persson, *Conformal array antenna theory and design*, Wiley–IEEE Press, 2006.

[124] A. Mehdipour, A.-R. Sebak, C. W. Trueman, I. D. Rosca, and S. V. Hoa, "Performance of microstrip patch Antenna on a reinforced carbon fiber composite ground plane," *Microwave Optic Lett.*, Vol. 53, No. 6, pp. 1328-1331, 2011.

[125] N. Srivastava, H. Li, F. Kreupl, and K. Banerjee, "On the applicability of single-walled carbon nanotubes as VLSI interconnects," *IEEE Trans. Nanotechnol.*, Vol. 8, pp. 542-559, 2009.

[126] P. Avouris, "Carbon nanotube electronics," *Chemical Physics*, Vol. 281, pp. 429–445, 2002.

[127] P. J. Burke, S. D. Li, and Z. Yu, "Quantitative theory of nanowire and nanotube antenna performance. *IEEE Trans. Nanotechnol.*, Vol. 5, pp. 314-334, 2006.

[128] G. W. Hanson, "Fundamental transmitting properties of carbon nanotube antennas," *IEEE Trans. Antenna and Propagat*., Vol. 53, pp. 3426-3435, 2005.

[129] G. W. Hanson, "Current on an infinitely-long carbon nanotube antenna excited by a gap generator," *IEEE Trans. Antenna and Propagat*., Vol. 54, pp. 76-81, 2006.

[130] W. C. Chen, W.-Y. Yin, L. Jia, and Q. H. Liu, "Electrothermal characterization of single-walled carbon nanotube (SWCNT) interconnect arrays," *IEEE Trans. Nanotechnol.*, Vol. 8, pp. 718-728, 2009.

[131] W. Hoenlein, F. Kreupel, G. S. Duesberg, A. P. Graham, M. Liebau, R. V. Seidel, and E.Unger, "Carbon nanotube applications in microelectronics," *IEEE Trans. Compon. Packag. Techn.*, vol. 27, no. 4, pp. 629–634, 2004.

[132] J. J. Plombon, K. P. O'Brien, F. Gstrein, V. M. Dubin, and Y. Jiao, "High-frequency electrical properties of individual and bundled carbon nanotubes," *Appl. Phys. Lett.*, Vol. 90, 2007.

[133] M. S. Sarto, A. Tamburrano, and M. D'Amore, "New electron-waveguide-based modeling for carbon nanotube interconnects," *IEEE Trans. Nanotechnol.*, Vol. 8, pp. 214-225, 2009.

[134] H. Li, W.-Y. Yin, K. Banerjee, and J.-F. Mao, "Circuit Modeling and Performance Analysis of Multi-Walled Carbon Nanotube Interconnects," *IEEE Trans. Electron Device*, Vol. 55, pp. 1328-1337, 2008.

[135] C. Rutherglen, and P. Burke, "Nanoelectromagnetics: circuit and electromagnetic properties of carbon nanotubes," *Small*, Vol. 5, pp. 884-906, 2009.

[136] J. Song, J. Kim, Y. Yoon, B. Choi, and C. Han, "Inkjet printing of singe-walled carbon nanotubes and electrical characterization of the line pattern," *Nanotechnol.*, Vol. 19, pp. 095702, 2008.

[137] P. J. Burke, and C. Rutherglen, "Carbon nanotube based variable frequency patch antenna", US patent 2009/0231205 A1, September 17, 2009.

[138] A. Mehdipour, I. D. Rosca, A.-R. Sebak, C. W. Trueman, and S. V. Hoa, "Advanced carbon-fiber composite materials for RFID tag antenna applications", *Applied Computational Electromagnetic Society* (*ACES*) *Journal*, Vol. 25, pp. 218-229, 2010.

[139] Y. Zhou, Y. Bayram, J. L. Volakis, and L. Dai, "Conformal Load-Bearing Polymer-Carbon Nanotube Antennas and RF Front-Ends," *IEEE Antenna and Propagation Symposium* (*APS* 2009), Charleston, SC, June 1-5, 2009.

[140] A. Mehdipour, I. D. Rosca, A.-R. Sebak, C. W. Trueman, and S. V. Hoa, "Full-composite fractal antenna using carbon nanotubes for multiband wireless applications," *IEEE Antenna and Wireless Propagation Lett.*, Vol. 9, pp. 891-894, 2010.

[141] T. J. Warnagiris, and T. J. Minardo, "Performance of a meandered line as an electrically small transmitting antenna," *IEEE Trans. Antennas and Propagat.* , Vol. 46, pp. 1797-1801, 1998.

[142] K.-L. Wong, L.-C. Chou, and C.-M. Su, "Dual-band flat-plate antenna with a shorted parasitic element for laptop applications," *IEEE Trans. Antennas Propag.*, Vol. 53, pp. 539-544, 2005.

[143] J.-Y. Jan, and L.-C. Tseng, "Small planar monopole antenna with a shorted parasitic inverted-L wire for wireless communications in the 2.4-, 5.2-, and 5.8-GHz bands," *IEEE Trans. Antennas Propag.*, vol. 52, pp. 1903-1905, 2004.

[144] R. Li, B. Pan, J. Laskar, and M. M. Tentzeris, "A novel low-profile broadband Dual-frequency planar antenna for wireless handsets," *IEEE Trans. Antennas Propag.*, vol. 56, pp. 1155-1162, 2008.

[145] A. Mehdipour, A.-R. Sebak and C. W. Trueman, "Compact microstrip-fed antenna for 2.4/5.2/5.8 GHz wireless communication systems," *Presented at IEEE Antenna and Propagation Symposium* (*APS* 2009), Charleston, SC, June 1-5, 2009.

[146] D. H. Werner, and S. Gangul, "An overview of fractal antenna engineering research," *IEEE Antennas and Propagation Magazine*, Vol. 45, pp. 38-57, 2003.

[147] D.-C. Chang, B.-H. Zeng, and J.-C. Liu, "CPW-Fed circular fractal slot antenna design for dual-band applications," *IEEE Trans. Antennas Propag.*, Vol. 56, pp. 3630-3636, 2008.

[148] W.J. Krzysztofik, "Modified Sierpinski fractal monopole for ISM-bands handset applications," *IEEE Trans. Antennas and Propag.*, Vol. 57, pp. 606-615, 2009.

[149] W.-L. Chen, G.-M. Wang, and C.-X. Zhang, "Bandwidth enhancement of a microstrip-line-fed printed wide-slot antenna with a fractal-shaped slot," *IEEE Trans. Antennas Propag.*, Vol. 57, pp. 2176-2179, 2009.

[150] N. Kaneda, W. R. Deal, Y. Qian, R. Waterhouse, and T. Itoh, "A broad-band planar quasi-Yagi antenna." *IEEE Trans. Antennas Propag.*, Vol. 50, pp. 1158-1160, 2002.

[151] A. A. Eldek, A. Z. Elsherbeni, and C. E. Smith, "Wide-band modified printed bow-tie antenna with single and dual polarization for C– and X-band applications," *IEEE Trans. Antennas Propag.*, Vol. 53, pp. 3067-3072, 2005.

[152] M. E. Bialkowski, A. W. Robinson, and H. J. Song, "Design, development, and testing of *X*-band amplifying reflectarrays," *IEEE Trans. Antennas Propag.*, Vol. 50, pp. 1065-1076, 2002.

[153] X. Qu, S.-S. Zhong, and Y.-M. Zhang, "Dual-band dual-polarised microstrip antenna array for SAR applications," *Electronic Lett*. Vol. 42, 2006.

[154] A. Mehdipour, A. R. Sebak, C. W. Trueman, I. D. Rosca, and S. V. Hoa, "Carbon-Fiber Nanotubes for X-band Conformal Antenna Applications" *Presented in IEEE Antenna and Propagation Symposium* (*APS* 2010), Toronto, ON, July 11-17, 2010.

[155] W.-S. Chen, C.-K. Wu, and K.-L. Wong, "Square-ring microstrip antenna with a cross strip for compact circular polarization operation," *IEEE Trans. Antennas Propag.*, Vol. 47, pp. 1566-1568, 1999.

[156] E. Arnieri, L. Boccia, and G. Amendola, "A Ka-band dual-frequency radiator for array applications," *IEEE Antennas and Propagat. Lett*., Vol. 8, pp. 894-897, 2009.

[157] M. Sun, Y. P. Zhang, G. X. Zheng, and W-.Y. Yin, "Performance of intra-chip wireless interconnect using on-chip antennas and UWB radios," *IEEE Trans. Antenna Propag*., Vol. 57, pp. 2756-2762, 2009.

[158] R. A. Alhalabi, and G. M. Rebeiz, "High-Efficiency angled-dipole antennas for millimeter-wave phased array applications," *IEEE Trans. Antenna and Propag*., Vol. 57, pp. 2756-2762, 2009.

[159] T. Zwick, D. Liu, and B. P. Gaucher, "Broadband planar superstrate antenna for integrated millimeter wave transceivers," *IEEE Trans. Antenna and Propag*., Vol. 54, pp. 2790-2796, 2006.

[160] A. Mehdipour, I. D. Rosca, A.-R. Sebak, C. W. Trueman, and S. V. Hoa, "Carbon nanotube composites for wideband millimeter-wave antenna applications," *IEEE Trans. Antenna and Propagat*., Vol. 59, No. 10, pp. 3572-3578, 2011.

[161] Southwest Microwave, Inc., Tempe, AZ, US.

[162] J. Guterman, A. A. Moreira, C. Peixeiro, and Y. Rahmat-Samii, "User interaction with inverted-F antennas integrated into laptop PCMCIA cards," *RADIOENGINEERING*, Vol. 18, pp. 13-18, 2008.

[163] C.-C. Lin, S.-W. Kuo, and H.-R. Chuang, "A 2.4-GHz printed meander-line antenna for USB WLAN with notebook-PC housing," *IEEE Microwave Wireless Components Lett*., Vol. 15, pp. 546-548, 2005.

[164] K. Bahadori, and Y. Rahmat-Samii, "A miniaturized elliptic-card UWB antenna with WLAN band rejection for wireless communications," *IEEE Trans. Antennas Propag.*, Vol. 55, pp.3326–3332, 2007.

[165] T. X. Nguyen, S. V. Koppen, J. J. Ely, G. N. Szatkowski, J. J. Mielnik and T. P. Salud, "Small aircraft RF interference path loss measurements," *Proc. IEEE International Symp. Electromagn. Compat.*, Jul. 2007.

[166] G. Gerini, and L. Zappelli, "Multilayer array antennas with integrated frequency selective surfaces conformal to a circular cylindrical surface," *IEEE Trans. Antennas Propag.*, Vol. 53, pp.2020–2030, 2005.

[167] H. J. Visser, "Second European workshop on conformal antennas,"*IEEE Antenna's and Propagation Magazine,* Vol. 44, pp. 87-90, 2002.

[168] K. Kordas, T. Mustonen, T. Toth, H. Jantunen, M. Lajunen, C. Soldano, S. Talapatra, S. Kar, R. Vajtai, and P. M. Ajayan, “Inkjet printing of electrically conductive patterns of carbon nanotubes, *Small*, Vol. 2, No. 8-9, pp. 1021-1025, 2006.

Publications from the Research Work

Journal Papers:

1) A. Mehdipour, A.-R. Sebak, and C. W. Trueman, "Green's function of a dielectric slab grounded by carbon fiber composite materials," *IEEE Trans. Electromagn. Compat*., vol. 54, no. 1, pp. 118-125, 2012.

2) A. Mehdipour, I. D. Rosca, C. W. Trueman, A.-R. Sebak, and S. V. Hoa, "Multiwall carbon nanotube-epoxy composites with high shielding effectiveness for aeronautic applications," *IEEE Trans. Electromagn. Compat*., Vol. 54, No. 1, pp. 28-36, 2012.

3) A. Mehdipour, I. D. Rosca, A.-R. Sebak, C. W. Trueman, and S. V. Hoa, "Carbon nanotube composites for wideband millimeter-wave antenna applications," *IEEE Trans. Antenna and Propagat*., Vol. 59, No. 10, pp. 3572-3578, 2011.

4) A. Mehdipour, A.-R. Sebak, C. W. Trueman, I. D. Rosca, and S. V. Hoa, "Performance of microstrip patch Antenna on a reinforced carbon fiber composite ground plane," *Microwave Optic Lett.*, Vol. 53, No. 6, pp. 1328-1331, 2011.

5) A. Mehdipour, A.-R. Sebak, C. W. Trueman, I. D. Rosca, and S. V. Hoa, "Reinforced continuous carbon-fiber composites using multi-wall carbon nanotubes for wideband antenna applications," *IEEE Trans. Antenna and Propagat*., Vol. 58, No. 7, pp. 2451-2456, 2010.

6) A. Mehdipour, I. D. Rosca, A.-R. Sebak, C. W. Trueman, and S. V. Hoa, "Full-composite fractal antenna using carbon nanotubes for multiband wireless applications," *IEEE Antenna and Wireless Propagat. Lett.*, Vol. 9, pp. 891-894, 2010.

7) A. Mehdipour, I. D. Rosca, A.-R. Sebak, C. W. Trueman, and S. V. Hoa, "Advanced carbon-fiber composite materials for RFID tag antenna applications", *Applied Computational Electromagnetic Society* (*ACES*) Journal - Vol. 25, No. 3, pp. 218-229, 2010.

8) A. Mehdipour, A. Parsa, A.-R. Sebak and C. W. Trueman, "Miniaturized CPW-fed antenna and band-notched design for UWB applications", *IET Microw. Antennas and Propag*, Vol. 3, Iss. 6, pp. 974-986, 2009.

Conference Papers

1) A. Mehdipour, I. D. Rosca, A. R. Sebak, C. W. Trueman, and S. V. Hoa, "Reinforced continuous carbon fiber (RCCF) composite materials for microwave applications," *ASC/CACSMA Conference on Composites*, Montreal, QC, Canada, Sep. 2011.

2) A. Mehdipour, I. D. Rosca, A. R. Sebak, C. W. Trueman, and S. V. Hoa, "Advanced carbon fiber composite (CFC) materials for antenna applications," *ASC/CACSMA Conference on Composites*, Montreal, QC, Canada, Sep. 2011.

3) A. Mehdipour, A. R. Sebak, C. W. Trueman, I. D. Rosca, and S. V. Hoa, "Carbon-Fiber Nanotubes for X-band Conformal Antenna Applications" *IEEE Antenna and Propagation Symposium* (*APS* 2010), Toronto, ON, July 11-17, 2010.

4) A. Mehdipour, I. D. Rosca, C. W. Trueman, A. R. Sebak, and S. V. Hoa, "High frequency shielding properties of multiwall carbon nanotube (MWCNT) composites" *The 1st Canadian and American Technical Conference on Composites* (*ASC/CACSMA*), DE, US, 2009.

5) A. Mehdipour, I. D. Rosca, C. W. Trueman, A. R. Sebak, and S. V. Hoa, "Shielding effectiveness analysis of reinforced continuous carbon fiber (RCCF) composites: numerical and experimental study," *The 1st Canadian and American Technical Conference on Composites* (*ASC/CACSMA*), DE, US, 2009.

6) A. Mehdipour, A.-R. Sebak and C. W. Trueman, "Compact microstrip-fed antenna for 2.4/5.2/5.8 GHz wireless communication systems," *IEEE Antenna and Propagation Symposium* (*APS* 2009), Charleston, SC, June 1-5, 2009.

7) A. Mehdipour, A.-R. Sebak and C. W. Trueman, and S. V. Hoa "Carbon-Fiber composite T-match folded bow-tie antenna for RFID applications," *IEEE Antenna and Propagation Symposium* (*APS* 2009), Charleston, SC, June 1-5, 2009.

8) A. Mehdipour, C. W. Trueman, A. R. Sebak, I. D. Rosca and S. V. Hoa, "Shielding effectiveness analysis of multilayer carbon-fiber composite materials" *General Assembly of the International Union of Radio Science* (*URSI* 2008), Chicago, USA, 2008.

9) A. Mehdipour, A. Parsa, A.-R. Sebak and C. W. Trueman, "Planar bell-shape antenna fed by a CPW for UWB applications," *IEEE Antenna and Propagation Symposium* (*APS* 2008), San Diego, CA, US, 2008.

10) A. Mehdipour, A.-R. Sebak and C. W. Trueman, "A novel ultrawideband slot-antenna with dual band-notched characteristics," *IEEE Antenna and Propagation Symposium* (*APS* 2008), San Diego, CA, US, 2008.